Cavity-Enhanced Ultrafast Spectroscopy

A Dissertation presented

by

Yuning Chen

to

The Graduate School

in Partial Fulfillment of the

Requirements

for the Degree of

Doctor of Philosophy

in

Chemistry

(Physical Chemistry)

Stony Brook University

August 2018

Stony Brook University

The Graduate School

Yuning Chen

We, the dissertation committee for the above candidate for the

Doctor of Philosophy degree, hereby recommend

acceptance of this dissertation

Thomas K. Allison - Dissertation Advisor
Assistant Professor, Department of Physics and Chemistry

Trevor Sears - Chairperson of Defense
Professor, Department of Chemistry

Michael G. White - Third Internal Member
Professor, Department of Chemistry

Matthew Y. Sfeir - External Outside Member
Staff Scientist, Brookhaven National Laboratory

This dissertation is accepted by the Graduate School

Dean of the Graduate School

Abstract of the Dissertation

Cavity-Enhanced Ultrafast Spectroscopy

by

Yuning Chen

Doctor of Philosophy

in

Chemistry

(Physical Chemistry)

Stony Brook University

2018

Ultrafast optical spectroscopy methods, such as transient absorption spectroscopy and 2D spectroscopy, are typically restricted to optically thick samples, such as solids and liquid solutions. We have developed an all-optical technique, Cavity-Enhanced Ultrafast Spectroscopy, to study dynamics in molecular beams with femtosecond temporal resolution. By coupling frequency comb lasers into optical cavities, we have demonstrated ultrafast transient absorption measurements with a detection limit of $\Delta\text{OD} = 2 \times 10^{-10} (1 \times 10^{-9} \sqrt{\text{Hz}})$, where ΔOD is the change of optical density. Such a high sensitivity enables one to take all-optical ultrafast spectroscopy measurements in samples with column densities less than 10^{10} molecules/cm^2. I will present the signal enhancement principle, the technical details and the performance of this spectroscopy method and the proof-of-concept experiment in molecular iodine and iodine-argon clusters in a supersonic expansion.

To apply cavity-enhanced ultrafast spectroscopy to various molecules of interest, we have extended the operating spectral range of this method to be widely tunable. In this thesis, I will present the spectrometer with ultraviolet pump and tunable visible probe. I will discuss key technical achievements including the high power tunable visible frequency comb laser generation and stabilization, the sample delivery in a molecular beam, technical details of the tunable visible spectrometer and its application to the dynamics of excited state intramolecular proton transfer (ESIPT) in jet-cooled molecules and clusters.

Contents

List of Figures

Acknowledgements

When I was writing this thesis and reviewing my six years in graduate school, I came across with an inspiring story of growing bamboo trees from seeds. Starting with the seeds, one needs to water the soil where the seeds are planted every day. It takes a few months or even years for the seeds to break the ground. Meanwhile, the best one can do is to try to maintain the environment and be patient since the ground seems empty in an outsider's eyes. However, after a few years with all the time and effort, the bamboo trees start to grow and they can grow more than a foot every day. So is the bamboo forest formed within a few weeks or a few years?

This story inspired me to thank the people who taught me how to grow my bamboo forest and helped me make it through. When I started in the Allison lab, I did not have any experience working with lasers and sophisticated instruments. Fortunately, I have always been teamed up with brilliant minds. Professor Tom Allison took me as the first student and spent countless hours advising me and answering my questions. Tom has been always inspiring not only as an enthusiastic and responsible scientist but also as a dedicated advisor who values my education. I would like to thank Dr. Melanie Reber who worked with me for three years at the beginning of my Ph.D.. Melanie taught me how to work smart and think independently. It is a wonderful time setting up the lab, building the spectrometer and getting it to work with Melanie. I would like to thank Myles Silfies, who has always been an awesome partner to work with and fun person to talk to about hobbies. I also thank other excellent coworkers in Allison lab, including Dr. Chris Corder, Peng Zhao, Xinlong Li, Dr. Elena Pavlenko, Jin Bakalis, Jose Bautista for helping me out in the lab and for the science-stimulating group lunch conversations. There are definitely more people supposed to be included in the list and excuse me for not listing all names here.

I would like to thank all my thesis committee members Prof. Trevor Sears, Prof. Michael White, Dr. Matthew Sfeir and Prof. Jin Wang for the time and effort helping me with my thesis work. I also would like to thank the physical chemistry community and AMO physics community at Stony Brook for the inspiring discussions with Prof. Chris Johnson, Dr. Sarah Waller, Prof. Tom Weinacht, Prof. Hal Metcalf, Prof. Eden Figueroa and for generous equipment donations from Prof. Phillips Johnson, Prof. Trevor Sears, Prof Michael White. I'd like to thank the awesome AMO graduate student group, including Spencer, Yusong, Ludwig, Brian, Bertus, Mike, Peter and many more not included in this very short list, for helping me holding up and having fun at Stony Brook.

Last but not least, I would like to thank my family, particularly my parents Zhenhua Chen and Guixia Chen for loving me unconditionally and always supporting me to be a better me. I want to thank my husband Dr. Pengyu Yuan, who has been always loving and supportive, through the good times and the bad times. Without him, this work would have not been possible.

Chapter 1

Introduction

Ultrafast spectroscopies are used to study dynamics on nanoseconds to tens of attoseconds timescales in chemistry, physics, biological and material science. The basic concept is the pump-probe method. The pump pulses excite the sample molecules and generate short-lived species. The probe pulses monitor the molecules at excited states at different time delays after the absorption of pump pulses. The ultrafast dynamics of the excited molecules are encoded in the time delay dependent signals. Depending on the specific detection techniques, there are many different methods based on this pump-probe concept. The detection could be done in photons [1, 2, 3], photoelectrons [4], and ions [5]. With multiple pump pulses instead of one in each pump-probe pulse pair, ultrafast spectroscopies could be extended to multidimensional spectroscopies, such as 2D spectroscopies [6, 7].

Among the various ultrafast time-resolved spectroscopy techniques, transient absorption is one of the most widely used method in many research disciplines. The principle of transient absorption spectroscopy (TAS) is shown in Figure 1.1. The temporal evolution of molecules in excited states are recorded by changes in the transmitted probe light intensity or spectrum as a function of the pump-probe delays.

Study of ultrafast dynamics in dilute samples or samples that must be excited weakly to probe the desired physics [8, 9, 10, 11, 12] requires sensitive ultrafast spectroscopy methods. While a wealth of information has been gained from measuring the static spectra of these systems using a variety of methods [13, 14, 15, 16], studies recording dynamics are much more limited. Transient absorption spectroscopy is mostly limited to solution and solid samples due to the sensitivity. A typical sample concentration in TAS is 1

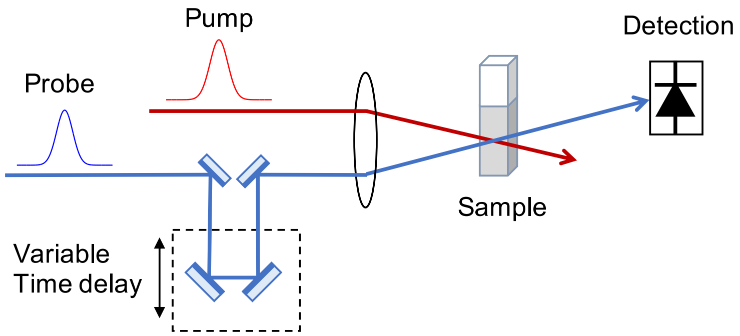

Figure 1.1: Basic components of transient absorption spectroscopy. The pump pulses excite the sample molecules. The probe pulses detect the change of absorption induced by the pump pulses at variable time delays. Transmission of the probe is recorded.

mmol/L, or a number density of 10^{18} molecules/cm^3. In molecular beams, the number density of molecules is less than 10^{14} molecules/cm^3, or 1.5×10^{-4} mmol/L [17]. Due to the orders of magnitude lower densities compared to solutions, application of transient absorption spectroscopy to isolated molecules in molecular beams is only feasible in some special cases before the work in this thesis.

To overcome the sensitivity problem, some ultrafast methods record the dynamics by detecting the photoelectrons and ions in molecules ionized by UV pulses and strong fields [4, 18]. These methods could be extremely sensitive due to the capabilities of single particle detection and background free signals. However, ionization projects the molecular state of interest onto a very different manifold of final states than optical measurements, and this can make the comparison of experimental data from gas phase and condensed phase highly non-trivial [19, 20]. Furthermore, while dynamics of electronically excited states can be probed by ionization, there exist no ionization-based methods for probing purely vibrational dynamics analogous to the powerful tools of ultrafast infrared spectroscopy [7].

1.1 Molecular beams

Work in this thesis in motivated by studying ultrafast dynamics in gas phase, specifically, in samples generated from molecular beams. A brief description of molecular beams is included here. The mean free path of gas molecules is the average travel distance taken by a moving particle before the molecule collides with another particle.

$$\lambda = \frac{1}{\sqrt{2}\pi d^2 n} \tag{1.1}$$

λ is the mean free path, d is the particle diameter and n is the number density of particle. For Helium, at 300 K, the mean free path in terms of the pressure is given by

$$\lambda_{\mathrm{He}}\ [\mathrm{cm}] = \frac{0.0147}{\mathrm{P\ [Torr]}} = \frac{1.1 \times 10^{-4}}{\mathrm{P\ [Pa]}} \tag{1.2}$$

P is the gas pressure in unit of torr or pascal. At a pressure of 1000 torr, the mean free path of He is 1.5×10^{-5} cm, and at 0.1 torr, λ is 0.15 cm. When molecules expand from 1000 torr to 100 mTorr through an orifice with an opening size of 100 μm, the molecules experience frequent collisions during the expansion process. The kinetic energy of the molecules exchange with the internal energy. As a result, the atoms and molecules travel at higher speeds with a narrower velocity distribution and cool down. During supersonic expansion, the total number of binary collisions experienced by a molecule is about 10^2 - 10^3. For diatomics, vibrational states remain unchanged during expansion since 10^4 collisions are required for vibrational relaxation. However, the vibrational relaxation of larger molecules and the rotational relaxation of diatomics requires only 10 - 100 collisions. These are the modes participating in the internal energy relaxation during expansion [21]. The speed of molecule traveling could surpass speed of sound, namely forming supersonic expansion, or free jet expansion since the molecules are traveling in a “free” way in the vacuum environment before the shock wave occurs. The distance of the shock wave from the orifice is dictated by the pressure ratio of the backing pressure and the vacuum pressure. If a skimmer is placed in the free expansion zone, a molecular beam could be guided by the skimmer and isolated from the shock wave.

Supersonic expansion is a rather simple way to generate isolated cold molecules at a temperature of a few to tens of Kelvins [21]. For example, for expansion of Ar from 300 K, the temperature of Ar could reach about 2 K with a Mach number of 22. Of course one could study the ultrafast dynamics of gas phase samples in hot vapor, we would argue that for studying the dynamics of electronically excited molecules, the starting vibrational states may not alter the dynamics significantly, however, for vibrationally excited molecules, the initial vibrational states of the sample molecules are critical. This is one of the reasons that we choose to study ultrafast dynamics of gas phase samples in molecular beams instead of studying vapors in sample cells.

Another reason that physical chemists use supersonic expansions is that some jet-cooled molecules form clusters in the expansion. The size of clusters N ranges from dimer to 10^4 [22]. Study of clusters bridges the gap between the gas phase and liquid phase studies. One example is to understand the role of solvent molecules in ultrafast dynamics such as excited state proton transfer (ESPT). ESPT is an ultrafast photo-induced process, and the dynamics have a strong dependence on the environment, namely, the temperature, the solvent, etc. We could take measurements in isolated molecules first, then study the molecule-solvent clusters of different sizes. This allows us to compare the clean measurements from the molecules free from disturbance of the chemical environment and the molecules surrounded by solvent molecules generated in a controlled way. A description of ultrafast dynamics of excited state intramolecular proton transfer as an example system, and the subsequent processes is included in Chapter 7 in details.

1.2 Cavity-enhancement for ultrasensitive spectroscopies

To enhance the optical signals from gas-phase samples and performing ultrasensitive measurements [23], enhancement cavities are used in linear spectroscopies [24] and nonlinear spectroscopy, such as Saturated-Absorption Cavity Ring-Down Spectroscopy [25]. The intracavity light passes through the sample many times and the signal is increased by a factor proportional to the cavity finesse.

The most common cavity configuration for small signal enhancement in spectroscopies is a two mirror cavity. We employ a bow-tie configuration for both pump and probe cavities for a few reasons. Besides the practical consideration of physically fitting the ~ 3 meters long cavities in the vacuum chamber, this configuration also allows independent control of the cavity length and the beam size at focus. The bow-tie cavity geometry also makes it convenient to separate probe and reference beams for cavity noise subtraction as shown in Figure 3.2 in Chapter 3.

1.2.1 Energy relations in optical ring cavities

All the signal enhancement cavities included in this thesis have bow-tie configurations. Here we briefly introduce the fields and intensities calculation in ring cavity. The incident light field is E_0 and the total reflected field is E_r. The field transmission and reflection coefficients at the input coupler are t_1 and r_1. Using the convention in [26], r_m is related to the round trip power loss, excluding the input coupling t_1 via

$$r_m = \sqrt{1 - L} \tag{1.3}$$

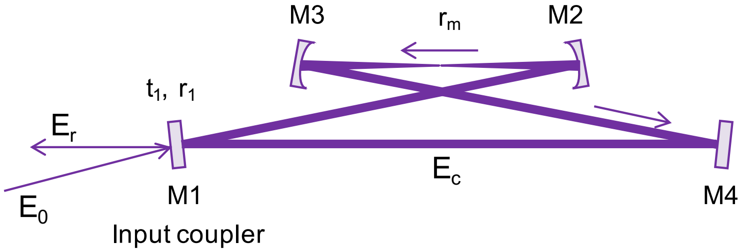

Figure 1.2: A schematic of ring-cavity to show the fields and intensities.

The total phase shift of one round trip is ψ. The total reflected field E_r is a sum of the reflected field and the transmitted field through the input coupler from different round-trips.

$$\begin{aligned} E_r &= -E_0 r_1 + E_0 r_m t_1^2 e^{-i\psi} + E_0 r_1 r_m^2 t_1^2 e^{-2i\psi} + \ldots \\ &= E_0 \frac{r_m e^{-i\psi} - r_1}{1 - r_1 r_m e^{-i\psi}} \end{aligned} \tag{1.4}$$

The field circulating the cavity is

$$\begin{aligned} E_c &= E_0 t_1 + E_0 r_1 r_m t_1 e^{-i\psi} + E_0 r_1^2 r_m^2 t_1 e^{-2i\psi} + \ldots \\ &= E_0 \frac{t_1}{1 - r_1 r_m e^{-i\psi}} \end{aligned} \tag{1.5}$$

Using $cos\psi = 1 - 2\sin^2\frac{\psi}{2}$, we get the intensities of the reflected and circulating light.

$$\begin{aligned} I_r &= I_0 \frac{(r_1 - r_m)^2 + 4 r_1 r_m \sin^2\psi/2}{(1 - r_1 r_m)^2 + 4 r_1 r_m \sin^2\psi/2} \\ I_c &= I_0 \frac{t_1^2}{(1 - r_1 r_m)^2 + 4 r_1 r_m \sin^2\psi/2} \end{aligned} \tag{1.6}$$

The circulating intensity is maximum when the round-trip phase shift ψ is an integer multiple of π. The optical resonance frequencies are related to the phase ψ via

$$\psi = \frac{\omega}{} \tag{1.7}$$

The cavity finesse is defined as the ratio of free spectral range and cavity linewidth $\Delta\nu_{1/2}$.

$$\mathcal{F} \equiv \frac{\text{free spectral range}}{\Delta\nu_{1/2}} = \frac{\pi\sqrt{r_1 r_m}}{1 - r_1 r_m} \tag{1.8}$$

Using equation 1.6, the highest achievable power buildup is when the round-trip phase shift ψ is an integer multiple of π.

$$\frac{I_c}{I_0} = \frac{t_1^2}{(1 - r_1 r_m)^2} = \frac{1 - r_1^2}{(1 - r_1 r_m)^2} \tag{1.9}$$

When $r_1 = r_m$, the cavity is impedance matched. For a ring cavity operating at impedance matched condition, and also with $r_1^2 + t_1^2 = 1$, the power enhancement factor is

$$\frac{I_c}{I_0} = \frac{t_1^2}{(1 - r_1 r_m)^2} = \frac{1}{t_1^2} = \frac{\mathcal{F}}{\pi} \tag{1.10}$$

When the loss of the round-trip is dominated by the input coupler mirror, which is an over-coupled cavity, the highest power buildup one could get is $\frac{2\mathcal{F}}{\pi}$ instead of $\mathcal{F}/\pi$.

1.2.2 Absorption sensitivity enhancement in ring cavities

To calculate the enhancement factor for absorption sensitivity in an optical cavity, we start with a system without a cavity. According to Beer's law, the transmitted light intensity I_{trans} after passing through an absorbing medium with incident light intensity I_0 can be described by

$$I_{trans} = I_0 e^{-\alpha l} \tag{1.11}$$

α is the absorption intensity coefficient and l is the interaction length. The sensitivity of light intensity to the small absorption can be expressed as

$$\frac{dI_{trans}}{d(\alpha l)} = -I_0 l e^{-\alpha l} = -I_{trans} \tag{1.12}$$

The change in transmitted light intensity is experimentally measured and can be expressed as

$$\frac{dI_{trans}}{d(\alpha l)} = -d(\alpha l) \tag{1.13}$$

When the absorption is in a ring-cavity, and αl is much smaller than the loss in the cavity mirrors, we can rewrite the intensity of light circulating in the cavity as

$$\begin{aligned} I_c &= I_0 \frac{t_1^2}{(1-g)^2} \\ g &\equiv r_1 r_m e^{-\frac{\alpha}{2}\cdot l} \end{aligned} \tag{1.14}$$

For a two-mirror standing-wave cavity, $g = r_1 r_m e^{-\frac{\alpha}{2}\cdot 2l}$. The sensitivity in the ring-cavity can be derived as

$$\begin{aligned} \frac{dI_c}{d(\alpha l)} &= \frac{\partial I_c}{\partial g} \cdot \frac{\partial g}{\partial(\alpha l)} \\ &= I_0 t_1^2 \cdot \frac{(-2)}{(1-g)^3} \cdot \frac{\partial g}{\partial(\alpha l)} \\ &= I_0 t_1^2 \cdot \frac{(-2)}{(1-g)^3} \cdot (-\frac{1}{2} r_1 r_m e^{-\frac{\alpha l}{2}}) \\ &= I_c \cdot \frac{(-2)}{(1-g)} \cdot (-\frac{1}{2} g) \\ &= I_c \cdot \frac{g}{1-g} \end{aligned} \tag{1.15}$$

Since the absorption is small, $g \approx r_1 r_m$. Also both r_1 and r_m are close to 1, $g \approx \sqrt{g}$.

$$\begin{aligned} \frac{\mathcal{F}}{\pi} &= \frac{\sqrt{r_1 r_m}}{1 - r_1 r_m} \\ &\approx \frac{\sqrt{g}}{1-g} \\ &\approx \frac{g}{1-g} \end{aligned} \tag{1.16}$$

The change in the intracavity light intensity due to the absorption is

$$\frac{dI_c}{I_c} = \frac{\mathcal{F}}{\pi} \cdot d(\alpha l) \tag{1.17}$$

Compared to the case without an optical cavity, the sensitivity to small absorption is enhanced by a factor of $\mathcal{F}/\pi$ in a ring-cavity. It's straightforward to see that this enhancement factor in a two-mirror cavity is $2\mathcal{F}/\pi$ mathematically since $\frac{\partial g}{\partial \alpha}$ is twice. This is also consistent with the intuitive picture that the light passes through the sample two times in one round-trip in a two mirror cavity while one time in a ring-cavity configuration.

1.3 Frequency comb cavity coupling

Frequency comb lasers have achieved tremendous success in many disciplines in the past few decades. Frequency combs can be understood in both time and frequency domain. In the frequency domain picture, the comb consists of evenly spaced comb teeth across the whole spectral range. In time domain, a frequency comb consists of a train of short pulses separated by the round-trip time in the laser cavity. A schematic of frequency combs is shown in Figure 1.3

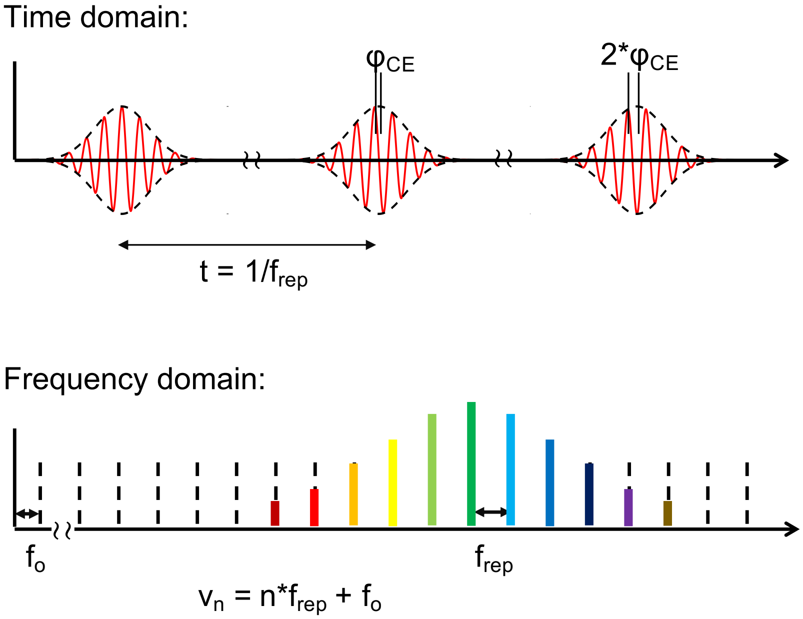

Figure 1.3: A simplified illustration of frequency combs in both time and frequency domain.

Some applications, such as frequency metrology and optical clocks, benefit from the high frequency precision that combs could provide [27, 28]. Some are utilizing frequency combs as many stable continuous lasers over a broad frequency span [29, 30]. This feature is used for fast data acquisition in linear spectroscopies, such as dual-comb spectroscopy [31].

Using an optical frequency comb as "a million stable lasers at once", several groups have employed the cavity-enhancement of frequency combs for performing linear spectroscopy that is simultaneously sensitive, broad-band, and high-resolution [32, 33, 34]. These techniques, called "Cavity-Enhanced Direct Frequency Comb Spectroscopy" (CE-DFCS), have now been applied to rapid trace gas detection [35, 36], breath analysis [35, 37], and microsecond time-resolved kinetics [38]. However, when frequency combs are coupled to cavities, the intracavity light can be short pulses that could be used for the sensitive detection of ultrafast time-resolved signals [39, 40].

The coupling between a frequency comb and a cavity could be understood in both frequency domain and temporal domain. In the frequency domain, a frequency comb has many comb teeth that are evenly separated by the comb's repetition rate. A cavity has transverse modes separated by the cavity's free spectral range, which can be adjusted to match the laser repetition rate or vise versa. The cavity also has a carrier-envelope offset frequency f_o as well as the frequency comb and f_o of the cavity and comb need to be matched. In the time domain, a frequency comb is a train of short pulses with an interval of $1/f_{rep}$. At the input coupler mirror, which is a partial reflecting mirror, the pulses transmit and circulate in the cavity. If we adjust timing and phase evolution of the pulses from the laser to match those of the cavity, the transmitted incident pulses constructively interfere with the laser pulses. This coherently enhances the femtosecond pulses in the cavity.

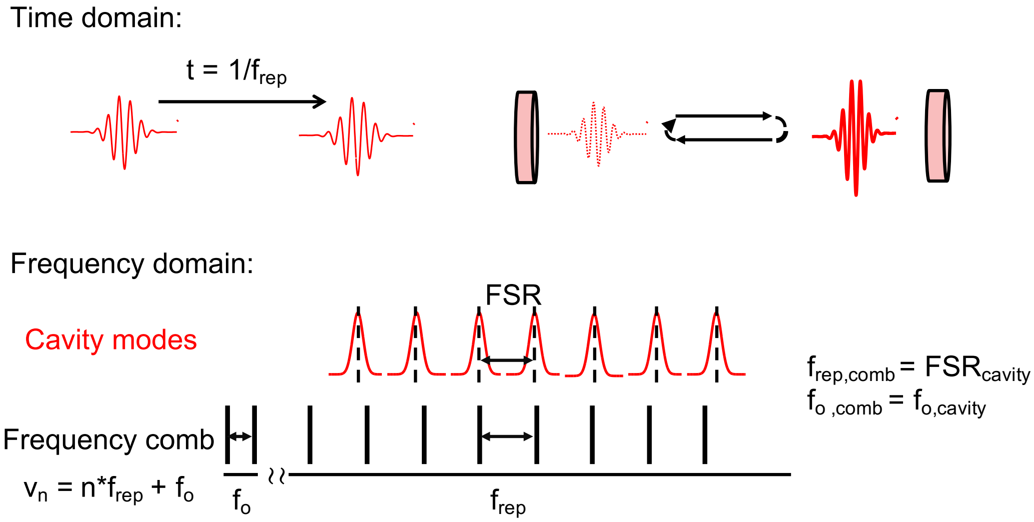

Figure 1.4: The figure shows the coupling of frequency combs to optical cavities.

1.4 Cavity-Enhanced Ultrafast Spectroscopy

By coupling optical frequency combs to pump and probe cavities, we have developed Cavity-Enhanced Ultrafast Spectroscopy to study ultrafast dynamics in samples from supersonic expansion. An extremely simplified schematic of Cavity-Enhanced Transient Absorption Spectroscopy (CE-TAS) layout is shown in Figure 1.5.

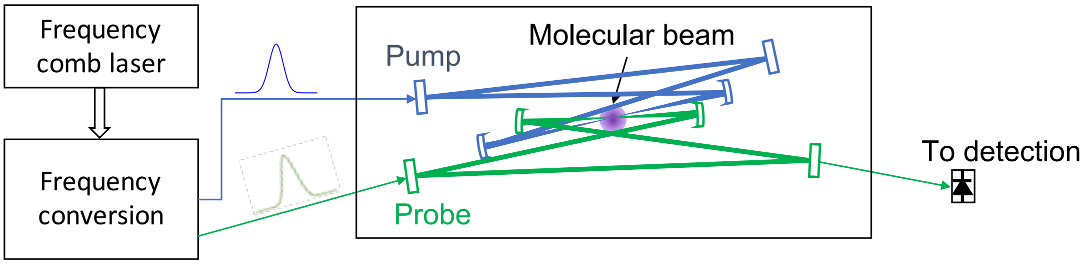

Figure 1.5: The schematic of Cavity-Enhanced Ultrafast Spectroscopy. Generated with one fiber frequency comb laser, the pump and probe comb lasers are converted to the desired spectral range and coupled into corresponding cavities. The pump and probe cavities overlap at the focal plane, where the sample molecules are introduced to by a molecular beam generated from a nozzle. The intensity of probe cavity transmission is recorded as a function of pump-probe delay.

1.5 Principle of Ultrafast Signal Enhancement

The fundamental mechanism for ultrafast signal enhancement is the same as in CE-DFCS and other cavity-enhanced spectroscopies. In CE-DFCS, an intracavity pulse traverses a sample of molecules, identical each round trip in the limit of weak excitation, many times. The signal is enhanced by $\mathcal{F}_{probe}/\pi$ for the case of an impedance matched ring cavity, where $\mathcal{F}_{probe}$ is the cavity finesse. In cavity-enhanced transient absorption spectroscopy (CE-TAS), the probe pulse also traverses a sample of molecules many times, but now we prepare this sample in an excited state using a pump pulse. This excitation, done at a repetition rate equal to the cavity's free spectral range, is identical every round trip, so from the point of view of the probe pulse absorption, there is no difference between CE-DFCS and CE-TAS, and the resulting signal enhancement is the same. Time resolution comes from the time dependence of the excited state of the molecules, as in a normal pump-probe experiment, and the time-resolved signal is recorded by simply varying the pump-probe delay with an external translation stage.

Viewed in the frequency domain, CE-TAS uses both the intracavity comb's spectral amplitude and spectral phase, which encodes the pulse shape and delay, whereas CE-DFCS uses only the amplitude. The recorded transient absorption signal can be viewed as a third-order wavemixing process between the pump and the probe pulses and thus depends on the spectral phase [7]. The fractional change in the probe light intensity ($\Delta I/I$), scales as the product of the pump power and the probe cavity finesse. Resonant enhancement of the pump pulses, with a separate cavity of finesse $\mathcal{F}_{pump}$, can provide passive amplification of the pump power so in principle the signal scales as $\mathcal{F}_{pump}\mathcal{F}_{probe}$. However, in practice the pump power cannot be arbitrarily increased because it is desirable to perform the experiment in the perturbative limit to avoid multi-photon excitation of the sample by the pump pulse alone. A good rule of thumb for transient absorption spectroscopy is approximately 1% excitation [41].

The pump cavities we use in the thesis are all in an over-coupled configuration to have the highest ratio of intensity enhancement (power buildup) to finesse. The round-trip loss in pump cavities are dominated by the input coupler mirror transmission. For the probe cavity, we use a configuration close to impedance-matched, and the probe cavity enhancement is $\mathcal{F}/\pi$ as we derived earlier.

1.6 Technical challenges in cavity-enhanced ultrafast spectroscopy

While using enhancement cavities benefit the signal size, they also introduce technical challenges. A few major ones are discussed here. One is the generation and stabilization of high power and narrow linewidth frequency comb lasers. We use a near zero dispersion Yb:fiber oscillator and chirped pulse amplification, which produces a high power and narrow linewidth frequency comb laser. This work is described in detail in Chapter 2. The widely tunable visible frequency comb laser generation is included in Chapter 6. Another technical difficulty is the enhancement cavity mirror design, particularly the cavity for coupling a tunable visible frequency comb laser. A brief discussion of how dispersion affects the pulse duration is included in the following subsection. The mirror design for tunable visible frequency comb is included in Chapter 5.

1.6.1 Generation and stabilization of high power, widely tunable and narrow linewidth frequency comb lasers

For cavity-enhanced ultrafast spectroscopy, the frequency comb laser needs to satisfy the several following conditions and the reasons for each are listed here. The repetition rate of the frequency comb lasers in this thesis are between 87 MHz and 100 MHz. This corresponds to a cavity length of about 3 meters and the time interval between pulses is about 10 ns. A lower rep rate means a longer cavity, which will be harder to physically fit in the vacuum chamber. Another problem of a much lower rep rate is the narrower cavity linewidth. Since the linewidth of an optical cavity is the free spectral range (FSR) divided by the cavity finesse, $\mathcal{F}$.

$$\nu_{1/2} = \frac{\mathrm{FSR}}{\mathcal{F}} = \frac{c}{l}\frac{1}{\mathcal{F}} \tag{1.18}$$

For cavities with the same finesse, the smaller rep rate ($\mathrm{f_{rep}} = \mathrm{FSR}$) cavity has a much smaller linewidth. This increases the difficulty in coupling the comb efficiently and achieving low noise. But a much higher rep rate limits the dynamics we could study. If the excited state dynamics persist for longer than $1/\mathrm{f_{rep}}$, the next pair of pump probe pulses will sample the excited molecules left from the previous experiment. A higher repetition rate also means the pulse energy is lower, which makes the nonlinear optics and pump-probe more difficult.

Compared to Ti:Sapphire lasers with a rep rate of 1 kHz, this high repetition rate means the pulse energy of our comb laser is 5 orders of magnitude smaller than a Ti:Sapphire laser assuming they have the same average power and this means the frequency conversion is more challenging. To generate a widely tunable frequency comb, a high average power laser is preferred. The probe signal enhancement cavities in this thesis are designed to have a finesse of a few hundred or 1000, which corresponds to a cavity linewidth of about 90 kHz. To efficiently couple the laser to the cavity with low noise, the frequency comb laser linewidth should be much narrower. Frequency comb generation and stabilizations are described in detail in Chapter 2 and Chapter 6.

1.6.2 Group delay dispersion control

When a pulse is circulating in the cavity, the round-trip spectral phase in the cavity can be expressed as

$$\begin{aligned}\psi(\omega) &= \psi(\omega_0) + \frac{\partial\psi}{\partial\omega}(\omega-\omega_0) + \frac{1}{2}\frac{\partial^2\psi}{\partial\omega^2}(\omega-\omega_0)^2 + \frac{1}{6}\frac{\partial^3\psi}{\partial\omega^3}(\omega-\omega_0)^3 + \cdots \\ &= \psi_0 + \psi_1(\omega-\omega_0) + \frac{1}{2}\psi_2(\omega-\omega_0)^2 + \frac{1}{6}\psi_3(\omega-\omega_0)^3 + \cdots\end{aligned} \tag{1.19}$$

The $\psi_2 = \frac{\partial^2\psi}{\partial\omega^2}$ is the group delay dispersion (GDD). Due to the GDD in the cavity, the free spectral range of the cavity is not evenly spaced over the whole spectral range while the frequency comb teeth are evenly spaced [42, 43] as illustrated in Figure 1.6.

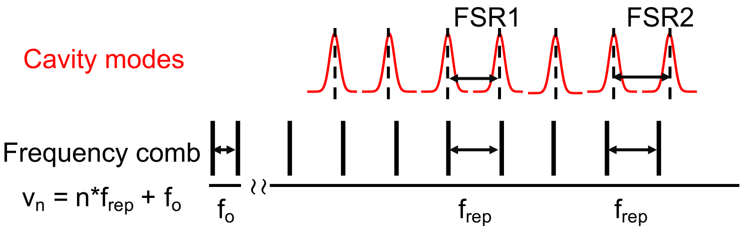

Figure 1.6: The cavity modes are not evenly spaced due to dispersion while the frequency comb teeth are evenly spaced. The mismatch between the cavity modes and the comb teeth limits the bandwidth can be coupled into the cavity.

As a result, how many comb teeth can be coupled into the cavity transverse modes strongly depends on the round-trip GDD and cavity finesse. In other words, the GDD and finesse could set an upper limit on the bandwidth one could couple into the cavity. If we rewrite intracavity light intensity in equation 1.6 with finesse

$$\begin{aligned}I_c &= I_0\frac{t_1^2}{(1-r_1r_m)^2 + 4r_1r_m\sin^2\delta/2} \\ &= I_0\frac{t_1^2}{(1-r_1r_m)^2}\cdot\frac{1}{1+4(\mathcal{F}/\pi)^2(\delta/2)^2}\end{aligned} \tag{1.20}$$

Using the two degrees of freedom $\mathrm{f_{rep}}$ and $\mathrm{f_o}$ of a frequency comb, the comb can be locked to a cavity at the center frequency ω_0 with both the zeroth and first order of δ to be zero. There is a resulting minimum phase error of δ, which is the second order component of δ

$$\begin{aligned}\delta &= \frac{1}{2}\psi_2(\omega-\omega_0)^2 \\ &= 2\pi^2\psi_2(\Delta\nu)^2\end{aligned} \tag{1.21}$$

The intracavity light can be rewritten as

$$I_c = I_0\frac{t_1^2}{(1-r_1r_m)^2}\cdot\frac{1}{1+4\pi^2\mathcal{F}^2\psi_2^2\Delta\nu^4} \tag{1.22}$$

$\Delta\nu$ is the bandwidth of pulse. The cavity acts as a spectral filter according to eqn. 1.22.

In the time domain, as a result of the narrower bandwidth the intracavity pulses possess, the pulses are longer. Therefore, we need to control the GDD in the cavity very well to maintain the femtosecond pulse durations for the ultrafast experiments. For the cavities used in this thesis, since the mirrors are housed in a vacuum environment, the GDD from gas is negligible. The GDD from mirror coatings is the dominant source of dispersion.

In our work, the pulses generated in the Yb:fiber laser are about 100 fs long and this has been the target time resolution for cavity-enhanced ultrafast spectroscopy. The finesses of the enhancement probe cavities are designed to be about 1000. When coupling femtosecond pulses to high-finesse optical cavities, the pulse broadening is determined by the cavity finesse and the GDD in cavity mirrors. With 100 fs input pulses, the intracavity pulse durations calculated with a few example cavities of different finesse and round-trip GDDs are included in Figure 1.7. In a cavity with a finesse of 1000 and round-trip group delay dispersion of 100 fs^2, the intracavity pulse duration is calculated to be 220 fs with 100 fs input pulses. For comparison, in conventional ultrafast spectroscopy experiments, 100 fs^2 of dispersion would only broaden a 100 fs pulse to 100.04 fs. Therefore, the cavity mirror coatings require very careful designs to keep the GDD low. As the cavity finesse gets higher, the control of cavity mirror GDD becomes more demanding. Details of cavity mirror coatings for each experiment are included in later chapters.

Ring-cavity finesse	Round-trip group delay dispersion [fs^2]	Intracavity pulse duration [fs]
1000	100	220
	300	340
10000	10	226
	300	797

Figure 1.7: Calculated intracavity pulse durations in cavities of different finesse and round-trip GDDs.

Chapter 2

High-power low-noise Yb:fiber frequency comb laser

In this chapter, we present a homebuilt high-power low noise Yb:fiber frequency comb laser. A detailed description of the oscillator, the amplifier and the laser system characterization are included.

2.1 Yb:fiber oscillator

Mode-locked fiber lasers can be broadly classified by their net cavity GDD and the saturable loss mechanism by which they are mode locked [44, 45]. With large anomalous GDD, soliton-like pulse shaping produces nearly chirp-free pulses, but with limited power [46, 44]. Lasers working with large normal GDD, even with all normal dispersion elements,[45] can support wave-breaking free pulses of very large energy. For example, Baumgartl *et al.*[47] have even demonstrated 66 W of average power and μJ pulses directly from an oscillator without subsequent amplification. However, for the quietest operation, with both the lowest phase and amplitude noise most suitable for comb applications, it is desirable to operate the laser near net zero cavity GDD [48, 49, 50, 51, 52]. Unlike Er-doped fiber lasers operating at 1.5 μm, where it is easy to make fibers with normal or anomalous dispersion, silica fibers predominantly have normal dispersion in the 1.0-1.1 μm range amplified by Yb, so that dispersion compensation is usually done with a free-space dispersive delay line [48, 53, 54] or fiber Bragg gratings [52, 51]. Fiber Bragg gratings can allow for all-fiber designs, but require very careful design before assembly, as the dispersion is not adjustable. Oscillators with a free-space dispersive delay line allow tuning to find zero dispersion. As we show in section 2.1.4, with transmission gratings, fine-tuning of the grating separation in such a delay line using piezo-electric actuators can also be used to control the comb's carrier-envelope offset frequency.

As an intense pulse propagates in the non polarization-maintaining fiber, the intensity of the pulse induces Kerr effect, e.g. an intensity-dependent nonlinear change in the refractive of index. The polarization of pulse rotates and experiences self-phase modulation, cross-phase modulation and birefringence of the fiber. For mode locking, nonlinear polarization evolution (NPE) in fiber [55, 56, 57] provides a fast artificial saturable absorber [58] that does not require any special components, but is sensitive to temperature or humidity changes. On the other hand, lasers based on real saturable absorbers, such as semiconductor saturable absorber mirrors (SESAM), can be made very environmentally stable, but typically have larger phase and amplitude noise [59, 60].[1] In our laser, we use NPE mode locking, and have observed free-running comb-tooth linewidth less than 30 kHz and residual intensity noise less than -130 dBc/Hz for frequencies above 10 kHz. We have also observed reasonable long-term stability in a laboratory setting (more details below).

2.1.1 Oscillator Construction

The basic layout for our Yb:fiber oscillator is shown in Figure 2.1. The fiber section provides gain and nonlinearity while the components in the free space section compensate the dispersion of the fiber, manipulate the polarization, and actuate on the pulse's round-trip group delay and carrier-envelope offset phase. An example mode-locked spectrum of the oscillator is shown in Figure 2.2.

---

[1] The quiet Yb-oscillators described in references [52] and [61] actually use a combination of both NPE and the SESAM

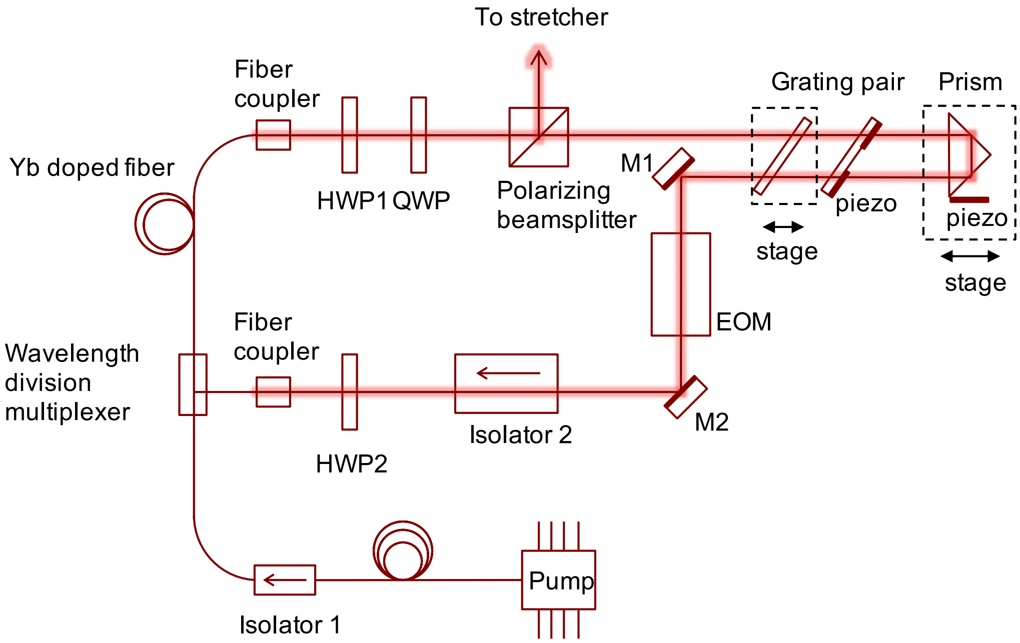

Figure 2.1: The block diagram shows the optical layout of the Yb:fiber oscillator. EOM: electro-optic modulator, G: grating, M: mirror, HWP: half waveplate, QWP: quarter waveplate. The beam displacement from the prism is vertical.

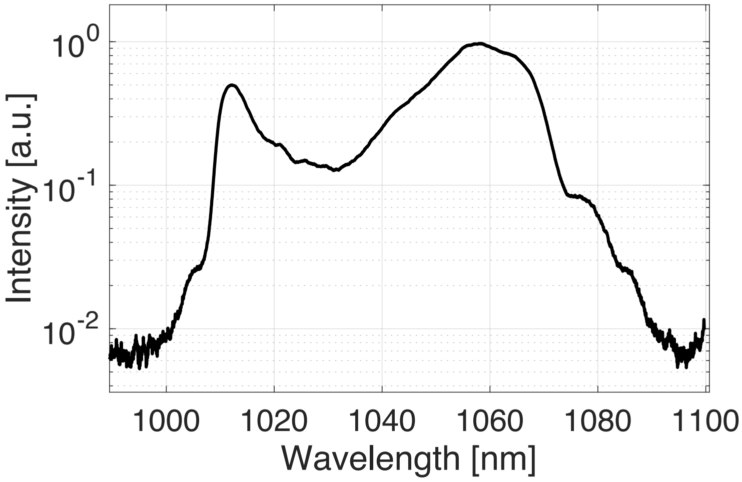

Figure 2.2: Mode-locked Yb:fiber oscillator spectrum.

The pump laser is a fiber Bragg grating stabilized diode laser operating at 976 nm (Oclaro LC96L76P-20R). Basic current and temperature controllers from Thorlabs (LDC210C and TED200C) are used to drive the pump laser. The noise specifications of this diode current controller are sufficient to obtain low-noise operation because the effect of high-frequency pump power fluctuations is suppressed by the low-frequency roll-off of the pump-modulation transfer function observed for this Yb:fiber oscillator, shown in Figure 2.5. Although the pump laser's fiber is polarization maintaining (PM), we simply splice this onto non-PM fiber for injection into the oscillator cavity with a fused wavelength division multiplexer (WDM). In addition to the WDM, a polarization insensitive isolator (Isolator 1) is used to isolate the pump laser from the oscillator light.

The fiber assembly is terminated on each end with anti-reflection (AR) coated angled FC/APC connectors which are then plugged into a fiber coupler lens assembly (Thorlabs PAF-X-5-C). These AR coated fiber tips are obtained simply by splicing the ends of AR coated patch cables (Thorlabs P4-980AR-2) to the ends of the gain fiber and WDM fiber pigtail. The use of connectorized fiber tips enables replacing the fiber assembly with minimal realignment and also allows for the rough alignment of the cavity using another fiber coupled laser, if desired. For the gain fiber, we have used either YB1200-4/125 or YB1200-6/125DC from Thorlabs with similar results. The fiber assembly is spliced together with a basic optical fiber fusion splicer. In our lab, we use a refurbished Ericsson FSU 995FA.

The specifics of the fiber lengths are important for a few reasons, and can be found in the appendix material. The first is that mode locking depends upon the amount of nonlinearity in the fiber [62] and the more fiber there is, particularly following the gain fiber, the easier it is to mode lock. Second, if the AR coated fiber tips become damaged, this is usually due to the gain fiber being too long, and is not remedied simply by reducing the pump power. However, the overall length of the assembly and the relative lengths of the different sections do not have to be controlled with high precision. By changing the fiber assembly, we have operated oscillators with repetition rates from 70 MHz to 97 MHz with the same free-space section and obtained similar performance.

In the free-space section, zeroth-order waveplates are used for polarization control and tuning of the laser, a Faraday isolator ensures uni-directional operation, an EOM enables fast actuation on the effective cavity length, and a pair of transmission gratings is used for dispersion compensation. A polarization beam splitter cube (PBS) is used as an output coupler, reflecting vertically polarized light out of the cavity. The first diffraction grating is mounted on a manual translation stage for finding zero dispersion, and a piezo-electric transducer (PZT) for fine-tuning the comb's carrier-envelope offset frequency. A right angle prism with an AR coated hypotenuse (Thorlabs PS908H-C) serves as the retroreflector in the dispersive delay line, changing the beam height by 5 mm and allowing the beam which initially crossed above to be reflected by D-shaped mirror (M1, which has a straight edge). In section 2.1.3, we describe the PZT and EOM actuators more carefully using fixed-point analysis [59, 63].

For suppression of acoustic noise and mechanical vibration, both oscillators are enclosed in aluminum sheet metal boxes sided with "egg-crate" style sound damping foam and built on honeycomb optical breadboards that are supported on the optical table with a 5/8" thick piece of sorbothane rubber. Light is coupled from the oscillator to the amplifier chain via the single-mode fiber pigtail of the stretcher fiber module.

2.1.2 Alignment, mode locking, and long-term stability

Since the stress-induced birefringence of the coiled fiber assembly is unknown, finding the correct positions of the waveplates for NPE mode locking is a somewhat random process. If one simply randomly rotates the three waveplates, this amounts to searching a three-dimensional space. We have instead developed a reliable procedure for finding mode locking that simplifies the search considerably. First, the oscillator is aligned with the goal of minimizing the pump power necessary for lasing, minimizing the CW lasing threshold, which includes optimizing beam alignment and iterative rotation of polarizers. The pump power is then increased to around 200 mW, well above the minimum pump power that can maintain mode locking, which is about 100 mW. The quarter-wave plate just before the input fiber coupler (QWP2) is rapidly rotated a few degrees back and forth. If mode locking is not achieved, the half-wave plate (HWP) should be stepped a few degrees and then the QWP2 rotation repeated. This process should be repeated until mode locking is achieved, usually within a few iterations. Once the first quarter-wave plate (QWP1) is set for lowest CW lasing threshold, it is generally not necessary to rotate it to find mode locking.

A major problem with NPE Yb:fiber oscillators is that they are prone to multi-pulsing,[64] or the production of more than one pulse circulating in the cavity. The separation between pulses can occur on many different time scales, and thus one needs a range of instruments to detect it. Unlike a Ti:sapphire oscillator, we have frequently observed multi-pulsing to occur with the particularly troublesome separation of 1-500 ps: too short to measure with a typical oscilloscope, but too long to observe easily as interference fringes in the optical spectrum. To be able to detect multi-pulsing at all separations, we employ a combination of three instruments: (1) a low resolution USB optical spectrometer for small pulse separations <3 ps, (2) a simple scanning autocorrelator using a GaAsP two-photon photodiode [65] for the 1-50 ps range, and (3) a fast photodiode (Electro Optics Technology Inc. ET-3010) and sampling oscilloscope (Tektronix 11801C with an SD-26 sampling head, 20 GHz equivalent bandwidth) for longer timescales. A collinear, interferometric autocorrelator is preferred so that one can align it well enough to have confidence in the alignment for longer stage travels, and a two-photon photodiode simplifies the nonlinear signal detection.

Once stable mode locking is found, one can search for the lowest noise. The grating spacing for net zero GDD can in principle be calculated using the material parameters for the fibers and other optical elements in the cavity, and this is a good place to start, but it is generally necessary to fine tune this spacing once mode locked. The GDD can be measured using the technique of Knox,[66] changing the center wavelength either by inserting a knife edge into the dispersed beam or rotating QWP2 slightly (or both). Figure 2.3 shows the different oscillator spectra with a knife edge partially blocking the beam between the grating and the prism.

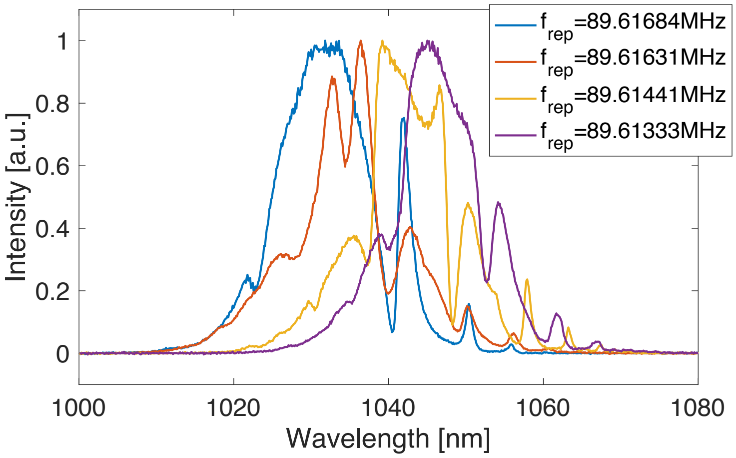

Figure 2.3: Yb:fiber oscillator spectra with a knife edge in the dispersive beam. The spectrum centroid shifted from 1033 nm to 1046 nm while the corresponding repetition rate is 89.61684 MHz and 89.61333 MHz for these two spectra. The total oscillator GDD is anomalous. The frequency comb's repetition rate is measured with a counter.

The net-group GDD is calculated by differentiating the group delay $T = 1/f_{rep}$, versus the center frequency of the optical spectra calculated with the optical spectrum centroid. For the measurements as shown in Figure 2.3, the oscillator's net GDD is obtained from the slope of the linear fit as shown in Figure 2.4 as -0.026 ps^2.

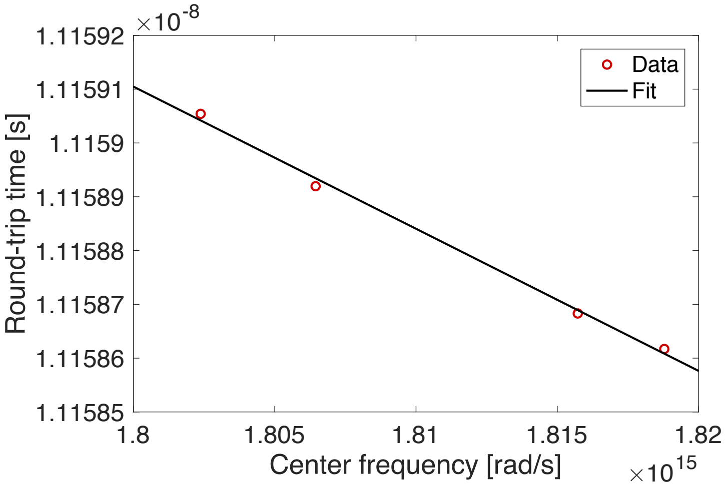

Figure 2.4: Yb:fiber oscillator round-trip GDD measurement. The red dots are the round-trip time with different spectra. The black line is a linear fit obtained with the least squares fitting. The slope gives a total round-trip GDD of -0.026 ps^2.

While tuning the grating separation, we monitor oscillator performance using two metrics that can be evaluated quickly: (1) The oscillator relative intensity noise (RIN), measured on a low noise, high bandwidth photodiode, and (2) the free-running heterodyne beat between the oscillator and a narrow linewidth (<1 kHz) CW Nd:YAG laser (Innolight Mephisto). Cingöz *et al.* [67] showed that the phase noise and the RIN are correlated, and as reported by Nugent-Glandorf *et al.* [48] the laser comb-tooth linewidth depends strongly on the net cavity GDD. Indeed, we have observed optical linewidths ranging between 2 MHz and less than 30 kHz this way, depending on the grating separation.

Once satisfactory mode-locked performance is found, we leave the oscillator on indefinitely, and have enjoyed stable hands-free operation for many months at a time in a laboratory setting with reasonable temperature and humidity control (±1 °C, 20-60% relative humidity). The parts of the laser that in principle have finite lifetimes, the pump diode and the gain fiber, are inexpensive. We have not observed significant degradation of the pump diode performance over five years of nearly continuous operation. However, we have observed that the gain fibers can fail after about one year of continuous operation. The main symptom of this is that the laser just won't mode lock. Lasing thresholds and output powers are similar, but stable mode-locked operation is not re-attained until the gain fiber is replaced, or a new fiber assembly with a fresh gain fiber is installed in the oscillator.

2.1.3 Comb Stabilization

The key element defining an optical frequency comb is that its comb teeth are evenly spaced to an extraordinary precision [42, 43]. This occurs naturally in mode-locked lasers and can also occur in other comb-generating systems such as microresonators [68] and broad-band electro-optically modulated light fields [69]. Once even spacing is established, the comb has two degrees of freedom that determine the frequencies of the comb teeth. Usually this is expressed in terms of the electronically countable repetition rate f_{rep} and carrier-envelope offset frequency f_0 via the familiar comb formula

$$\nu_n = n f_{rep} + f_0 \tag{2.1}$$

where n is an integer and the ν_n are the optical frequencies. Indeed, for self-referenced combs this may be the most sensible parameterization, as it is f_{rep} and f_0 that are actively controlled. However, for optically referenced combs, combs coupled to cavities, or when discussing the effects of actuators or noise sources, the discussion is often simplified by using a fixed point analysis, [70, 63, 59] writing the comb's optical frequencies as

$$\nu_n = (n - n^*) f_{rep} + \nu_{n^*} \tag{2.2}$$

where n^* is an integer representing a fixed point of the frequency comb that does not change due to a particular perturbation such as noise or intentional actuation on the laser. In the fixed point picture, one considers the comb teeth simply expanding and contracting around the fixed point via changes in f_{rep}. The larger the frequency difference is between the fixed point and a particular comb tooth, the more the frequency of that comb tooth changes due to the perturbation.

Since the frequency comb has two degrees of freedom, one needs two feedback loops and two actuators to stabilize the comb. Ideally, these two feedback loops would have zero cross-talk. For example, if one directly stabilizes f_{rep} and f_0, ideally one actuator would actuate only on f_{rep} and the other only on f_0. In practice, this goal is almost never reached exactly, which is acceptable as long as one feedback loop can be significantly slower than the other, such that the faster loop can adiabatically track and correct for the cross-talk from the competing loop.

For coupling a frequency comb to an optical cavity, or locking the frequency comb to another optical reference, it is desirable to have one fast actuator with its fixed point far from the optical frequency and another actuator with fixed point near the optical frequency. This allows the fast actuator to have large travel at optical frequencies that are being stabilized, and the second actuator to simply cause the comb to breathe around this locked point.

2.1.4 Transducer transfer functions

A commonly used combination of actuators to accomplish this is a fast intracavity EOM [71, 72, 73, 74, 75, 76, 77] for cavity length changes, with fixed point near DC ($n^* \sim 0$), and the pump laser power for changing the intracavity pulse's round trip phase shift, with fixed point near the optical carrier frequency [59, 63, 78]. While fast bandwidth can be obtained via actuating on the pump current in some laser designs [67], the bandwidth attainable with this actuator depends on the details of the laser and population inversion dynamics [79]. In the current ring cavity design with lower loss and smaller gain than the laser in reference [67], and thus lower relaxation oscillation frequency, we have observed the bandwidth of pump power modulation to be quite limited, as shown in Figure 2.5. To record this data, we modulate the pump diode current sinusoidally and record the amplitude modulation on the comb light with a photodiode and a spectrum analyzer. The pump current to pump power transfer function (not shown) was independently verified to be flat out past 1 MHz modulation frequencies with this setup, confirming that the roll-off is due to the transfer function of the Yb laser.

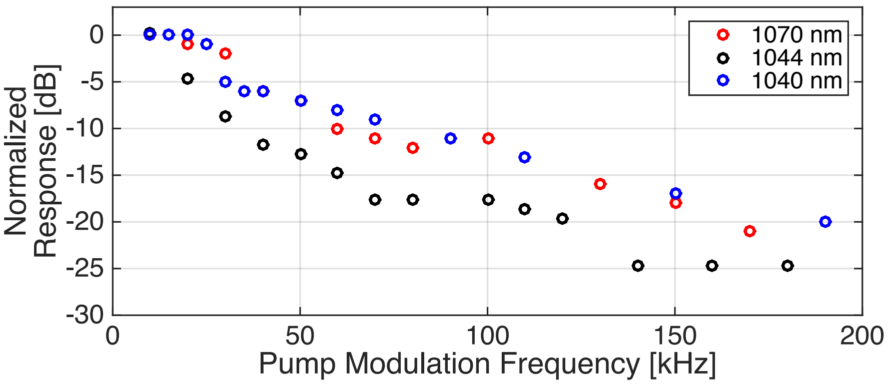

Figure 2.5: Pump amplitude to laser amplitude modulation transfer function. The different data are taken with mode-locked spectra centered at different wavelength. The spectrum tuning is achieved by moving a knife edge in the dispersive beam.

We use a bulk EOM for fast (multi-MHz bandwidth) actuation with a fixed point near DC, and instead of the pump power we use μm-scale piezoelectric adjustments of the grating spacing, which we show below has a fixed point near the optical frequency. Previous authors [76] have used short (few mm) EOM crystals due to concern over higher order dispersion. However, short crystals require multi-kV voltages to produce substantial phase shifts, and this is challenging to provide with high bandwidth. We have found that the remarkable tolerance of Yb:fiber oscillators to uncompensated higher-order dispersion [80] enables the use of longer crystals with correspondingly lower voltage requirements. The EOM is a commercial phase modulator (Thorlabs EO-PM-NR-C2) with a 40 mm MgO doped Lithium Niobate crystal and a V_π of 250 V. As shown in Figure 2.6), the EOM allows phase modulation with multi-MHz bandwidth without piezo-elastic resonances that have limited previous efforts [76]. To record this data, we drive the EOM with a sinusoidal voltage and record the amplitude of phase-modulation side bands on the heterodyne beat with the CW Nd:YAG laser, taking care of the fact that the intracavity EOM modulates the laser's *frequency* but the sidebands on the beat report on the *phase* modulation depth.

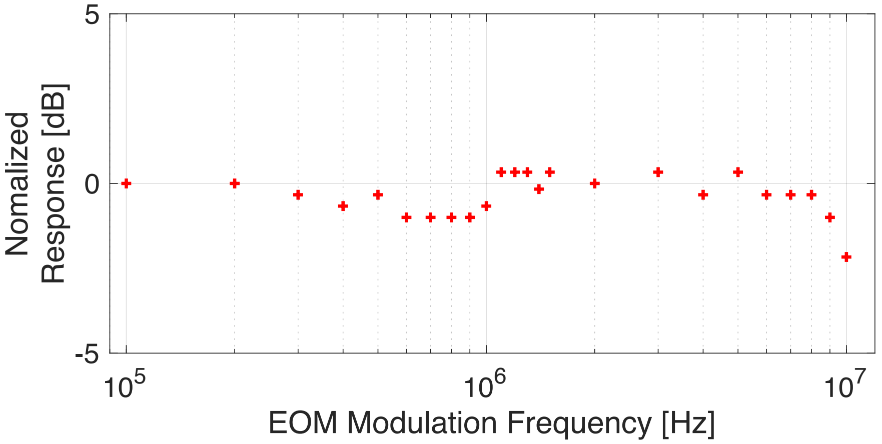

Figure 2.6: Voltage to phase modulation transfer function for the intracavity EOM.

We supply a 2 MHz sinusoidal voltage to the EOM to put frequency modulation (FM) sidebands on the comb that enable Pound-Drever-Hall (PDH) locking of the comb to passive optical cavities [81, 82, 83]. We measured the residual amplitude modulation (RAM) on the output light of the oscillator to be less than -90 dBc when driving the EOM with a 20 V (peak to peak) sine wave (more than what is typically required for PDH locking). The EOM alignment can be fine-tuned *in situ* by minimizing this RAM.

For actuation on the grating spacing, the first grating is glued to a ring PZT (Noliac NAC2125) using Loctite Hysol 1C-LV epoxy (also sold under the trade name Torr-seal), and this allows > 10 kHz of bandwidth before encountering mechanical resonances. Shifting the carrier-envelope offset phase of a pulse by actuation on the grating separation of a pulse compressor has been employed for carrier-envelope offset phase stabilization in amplified Ti:sapphire lasers (after the amplifier chain), [84] but to our knowledge this is first report of doing this inside a laser cavity. Here we derive the resulting frequency shifts for a transmission grating geometry and show that for transmission gratings operated in Littrow condition, the fixed point is at the optical carrier frequency $\nu_{optical}$, such that the change in f_0 is approximately $\nu_{optical}/f_{rep}$ larger than the change in f_{rep}.

For the parallel grating pulse compressor illustrated in figure 2.7, the total phase shift for one pass through the grating pair is given by:[85]

$$\phi_g(\omega) = \frac{\omega}{c} p(\omega) - \frac{2\pi}{d} G \tan(\beta) \tag{2.3}$$

where $\omega = 2\pi\nu$ is the angular frequency, $\phi_g(\omega)$ is the spectral phase, $p(\omega)$ is the frequency dependent optical path length through the compressor, β is the angle of diffraction determined from the grating equation, $\sin(\alpha) + \sin(\beta) = \lambda/d$, with α the angle of incidence measured from normal, d is the grating pitch, λ is the wavelength, and G is the distance between the gratings measured perpendicular to the grating surfaces. The second term in equation (2.3) accounts for the 2π phase shift encountered by the light for each grating groove traversed and must be included to obtain correct results [85]. Careful inspection of the angle-dependent path length shows that

$$\frac{d\phi_g}{dG} = \frac{\omega}{c} \left(\frac{1}{\cos(\beta)} - \frac{\cos(\alpha + \beta)}{\cos(\beta)} \right) - \frac{2\pi}{d} \tan(\beta) \tag{2.4}$$

Now one is tempted to locate the fixed point, ω^*, by setting equation (2.4) equal to zero and solving for ω, but this is not generally correct because mode locking demands that the comb teeth remain evenly spaced, and thus the differential phase shift between comb tooth $n+1$ and n must be the same as the differential phase shift between comb tooth $n+2$ and comb tooth $n+1$. Enforcing this fact that the comb has only two degrees of freedom amounts to linearizing the spectral phase using the phase shifts obtained near the optical carrier frequency, viz.

$$\frac{d\phi_{comb}}{dG} = \left.\frac{d\phi_g}{dG}\right|_{\omega_0} + \left.\frac{d\tau}{dG}\right|_{\omega_0} (\omega - \omega_0) \tag{2.5}$$

where $\tau = d\phi_g/d\omega$ is the frequency dependent group delay, which is evaluated at the optical carrier frequency ω_0 in equation (2.5). The fixed point is then given by

$$\omega^* = \omega_0 - \left(\left.\frac{d\phi_g}{dG}\right|_{\omega_0} \right) \left(\left.\frac{d\tau}{dG}\right|_{\omega_0} \right)^{-1} \tag{2.6}$$

At the Littrow condition, $\alpha = \beta(\omega_0) = \sin^{-1}(\pi c/\omega_0 d)$, one can show that the phase shift due to changing the grating separation, $d\phi_g/dG$, is identically zero and the fixed point is thus at the optical carrier frequency. For the more realistic scenario that the gratings end up slightly off-Littrow, one can use equations (2.2), (2.4), and (2.6) along with the relation $df_{rep}/dG = -f_{rep}^2\, d\tau/dG|_{\omega_0}$ in order to determine the changes in comb tooth frequencies. One can also derive relations for the changes in f_{rep} and f_0. For two passes through the grating pair, under Littrow conditions, the result is:

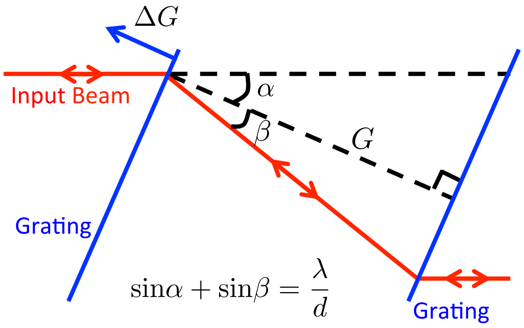

Figure 2.7: Illustration of the notation for the intracavity grating compressor. The grating spacing is adjusted slightly (ΔG) using a PZT to control the comb's carrier-envelope offset frequency. The arrow indicates the direction of positive ΔG.

$$\frac{df_{rep}}{dG} = -\frac{4\pi f_{rep}^2}{\omega_o d}\tan(\alpha). \tag{2.7}$$

$$\frac{df_0}{dG} = -n^* \frac{df_{rep}}{dG} = \frac{2 f_{rep}}{d}\tan(\alpha). \tag{2.8}$$

We have experimentally verified this analysis by recording changes in the comb repetition frequency and an optical comb tooth near 1064 nm when a voltage is applied to the grating PZT. The data are shown in Figure 2.8. The repetition rate changes are measured using a photodiode and a frequency counter. The changes in the optical frequency are measured by recording the beat frequency of an unstabilized heterodyne beat between the comb and the CW Nd:YAG laser. Linear fits to the data give slopes of $\frac{d\nu_{rep}}{dV} = 0.14$ MHz/V and $\frac{df_{rep}}{dV} = 0.39$ Hz/V. The number of comb teeth between 1064 nm and the fixed point can then be simply calculated from the ratio $\Delta\nu_{beat}/\Delta f_{rep} = 3.3 \times 10^5$. So the fixed point lies only approximately 30 THz away from the optical carrier frequency of 283 THz. This is consistent with the above equations and α deviating from the Littrow angle by approximately 4 degrees, which is realistic given our ability to initially set the grating angle in the laser and the α dependence of the grating's diffraction efficiency.

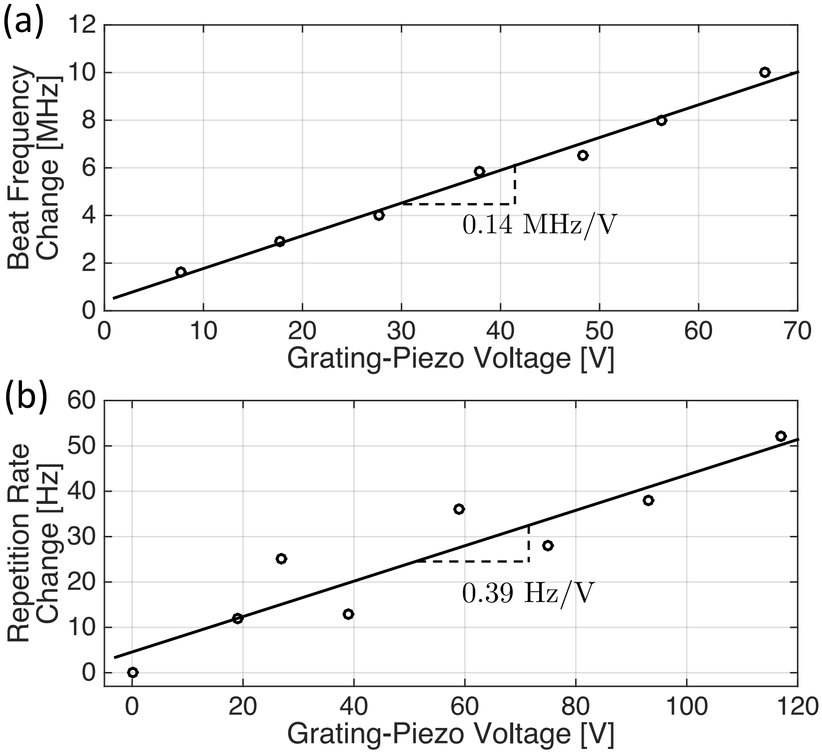

Figure 2.8: Grating actuations. a) 1064 nm beat frequency change with grating separation. b) Repetition rate change with grating separation. The data indicate that the fixed point is near the optical frequency.

The grating can also be used to make a shift purely in f_0, if the grating is moved parallel to its surface, similar to the motion of a sound wave in an acousto-optic frequency shifter. Here the phase shift is simply 2π per grating pitch moved,[86] and the fixed point is at $\nu = \infty$. Using both parallel and perpendicular motions, in principle one could completely control the comb with only μm-scale motions of the grating alone, as the two motions have different fixed points.

2.2 Dispersive wave shifted Er:fiber frequency comb laser

One desired operating spectral range of cavity-enhanced ultrafast spectroscopy is in the mid-infrared, particularly in the 3 - 5 μm for studying hydrogen bonding networks. For the convenience of generating mid-infrared frequency combs, we replaced the homebuilt Yb:fiber oscillator with a commercial Er:fiber frequency comb laser. Generation of widely tunable pulses have been reviewed by Brida *et al.* [87] An overview of mid-infrared generation setup with Er:fiber frequency comb laser is shown in Figure 2.9.

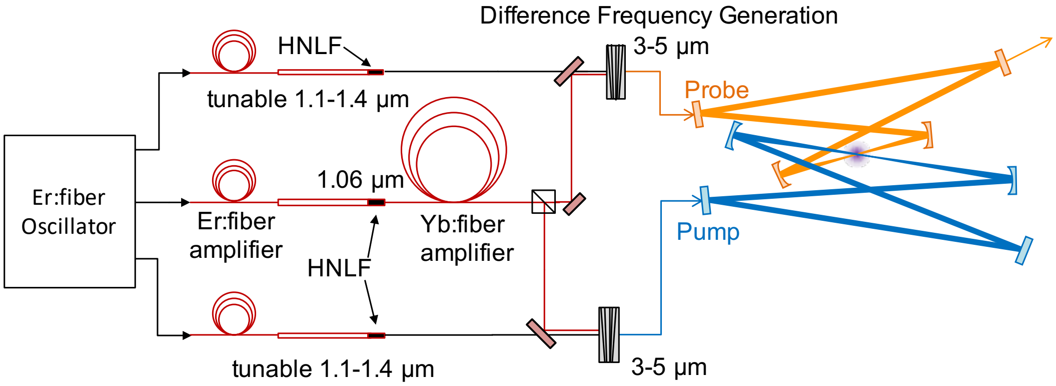

Figure 2.9: Overview of generating mid-IR frequency combs with Er:fiber oscillator. HNLF: highly nonlinear fiber.

The mode-locked Er:fiber frequency comb laser has three outputs with similar optical powers and spectra centered around 1550 nm. All three branches are amplified in homebuilt Er:fiber amplifiers to a few hundreds of miliWatts and the power could be tuned by tuning the pump power of the amplifier. In fused silica, the dispersion is anomalous at 1550 nm. As a result, the pulses are compressed to 30 - 50 fs in an undoped patch cable fiber before going into the highly nonlinear fiber (HNLF). The pulse duration could be optimized via changing the patch cable fiber length. In a 2 - 5 cm long highly dispersive fiber with a small core size, the femtosecond pulses form soliton at longer wavelengths. At the same time, the pulses generate phase-matched dispersive waves at shorter frequencies. By adjusting the pulse energy and pulse duration in the HNLF, the spectrum of dispersive wave is tunable between 1.1 - 1.4 μm.

The proposed pathway of generating the mid-IR frequency combs is via difference frequency generation in optical parametric amplifiers (OPAs). One branch of Er:fiber frequency comb laser is dispersive wave shifted to 1060 nm to seed the large mode area Yb:fiber amplifier described in the following section. The amplified 1060 nm light are split to pump two OPAs. The tunable pulses at 1.1 - 1.4 μm generated with the other two branches are used as the seed for the OPAs. The difference frequency is generated at 3 - 5 μm and these mid-IR pulses are coupled to pump and probe cavities for the spectroscopy experiment.

At the time of writing, the Yb:fiber amplifier seeding branch is in operation and the two tunable branches are proposed setups. The mid-IR frequency comb generation using dispersive wave shifted Er:fiber comb lasers have been demonstrated [88, 89].

To seed the chirped pulse amplifier, the 1060 nm pulses generated from HNLF is amplified in a homebuilt Yb:fiber amplifier before the fiber stretcher as is shown in Figure 2.10.

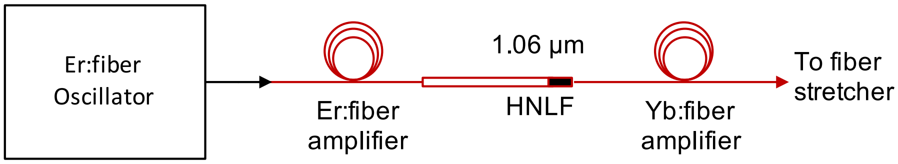

Figure 2.10: Dispersive wave shifted Er:fiber frequency comb laser. HNLF: highly nonlinear fiber.

To briefly summarize the chirped pulse amplification seeding laser sources, there are two different oscillators used for work included in this thesis. The homebuilt Yb:fiber oscillator is depicted in Chapter 2. The light from the amplifier seeded with Yb laser is used for the experiments in I_2 and I_2 Ar clusters in Chapter 3 and Chapter 4 and the supercontinuum generation in Chapter 6. The amplifier seeded with the Er laser is used in the tunable spectrometer development included in Chapter 5 and Chapter 6.

2.3 Chirped pulse amplification in Yb:doped photonic crystal fiber amplifier

Amplification of continuous wave lasers to high average power in Yb:fiber is straightforward, but amplification of femtosecond pulses presents additional complications. The long length of fiber presents a large amount of dispersion even for large mode area (LMA) fibers, and it is much more difficult to avoid accumulated nonlinear phase shifts than in bulk solid-state lasers. Designers of ultrafast fiber lasers usually take one of two approaches: embrace nonlinearity [90, 91, 92, 93, 94] or use stretchers and compressors with very large GDD to avoid it [61, 95, 96, 97, 98]. For comb applications, linear amplification, in which the B-integral, or accumulated nonlinear phase shift throughout the amplifier chain, is less than one, is generally preferred because then the amplified comb's coherence properties are determined mainly by the oscillator. In nonlinear amplification, amplitude noise from the high-power pump diodes in the amplifier chain could write phase noise on the amplified comb [99, 44], although we are aware of some recent efforts using high-power nonlinear fiber amplification for comb applications.[100, 101]

We have used linear chirped pulse amplification, but have strived to maintain modest stretcher/compressor dispersion by (1) seeding the amplifiers with very broad spectra, (2) maximizing the mode area of the seed light throughout the amplifier chain, even if this means seeding amplifiers below saturation, and (3) running the Yb amplifier to the red of the gain maximum at 1030 nm, to reduce gain narrowing, as shown by [51]. For simplicity and low-cost, we make use of a fiber stretcher based on anomalous third-order dispersion depressed cladding fibers (OFS) and grating compressor based on inexpensive polymer transmission gratings (Wasatch Photonics). While we do not quite reach transform limited pulses, the benefits of the simplicity of this scheme have outweighed the slightly reduced performance.

2.3.1 Photonic crystal fiber amplifier optical layout

A schematic of the chirped pulse amplifier scheme is shown in Figure 2.11. The oscillator light is coupled into a stretcher fiber module custom made by OFS Specialty Photonics Division with FC/APC connectorized SMF-980 fiber pigtails. Between the stretcher and the following Faraday isolator (I1), about half the seed power is lost. After the dichroic mirror (D1), which is used to isolate the pump light and seed (or signal) light, 15-20 mW is launched into the 5 m amplifier fiber. The amplifier fiber is a doped, LMA (760 μm^2) PCF terminated with sealed ends and copper SMA 905 connectors, purchased from NKT Photonics (aerogain Flex 5.0). This fiber is end pumped with a 30 W, 915 nm pump diode (nLight Element). After the second dichroic mirror (D2), the beam is expanded to 4.2 mm ($1/e^2$ diameter), sent through another Faraday isolator, and compressed using a pair of polymer transmission gratings (Wasatch Photonics) and a roof reflector (RM, or retroreflector, two mirrors with a 90 degree angle, to change the beam hight by two reflections). Below, we discuss these features in more detail and the design decision processes behind them.

The coiled amplifier fiber is supported on a circular aluminum plate. The pump end, where the optical power is the highest, is mounted in a water-cooled copper clamshell assembly. Detailed drawings of the copper clamshell can be found in the appendix. The seed end of the amplifier fiber is screwed into an SMA connector (Thorlabs HFB001) mounted on a flexure stage (Thorlabs MicroBlock MBT616D). The heavy copper mode-stripper assembly of the fiber is further supported by shims placed on the flexure stage. The output of the stretcher fiber and pump diode fiber are mounted on flexure stages in similar fashion. For delivering the pump light, the pump diode fiber pigtail is spliced onto the end of an AR coated multimode patch cable (Thorlabs M105L02S-B). The pump light is launched counter-propagating to the amplified seed light to reduce the accumulated nonlinear phase shift (B-integral) in the amplifier fiber. Despite not being "all-fiber", we have observed consistent performance from this mechanical setup without alignment for more than three years of operation.

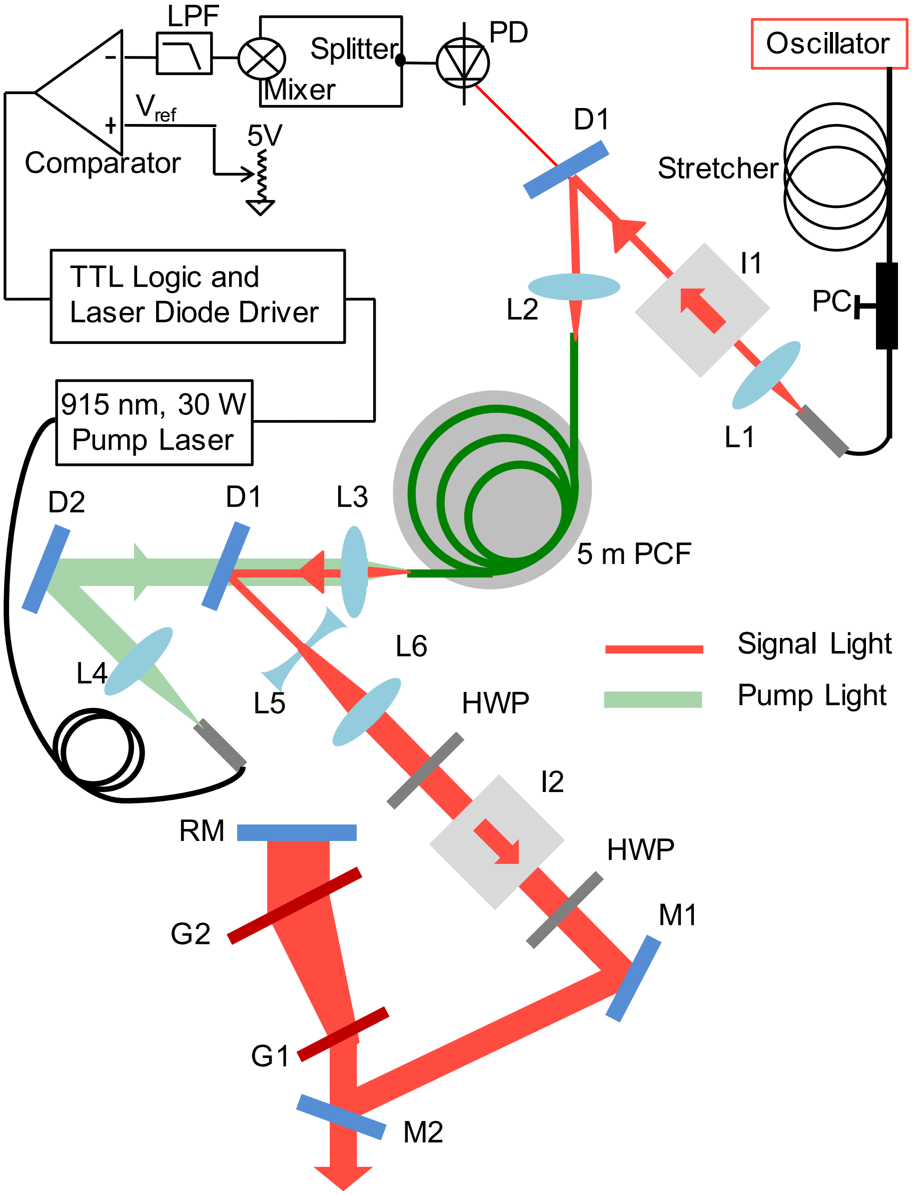

Figure 2.11: Photonic crystal fiber amplifier layout. Pulses from the oscillator are stretched and amplified in a 5 m flexible PCF amplifier up to 11.3 W average power without pre-amplification. Component lists can be found in the appendix material. PC: polarization controller. D: dichroic mirror. L: lens. PD: photodiode. RM: roof reflecting mirror. LPF: low pass filter. V_{ref} = reference voltage. G: grating. M: mirror. I: Faraday isolator. HWP: half-wave plate

2.3.2 Chirped pulse amplification results

The saturation power for the LMA PCF amplifier is more than 200 mW, and many previously reported amplifier systems using these PCF amplifiers have employed a fiber pre-amplifier with smaller mode area between the oscillator and the PCF amplifier [61, 98, 96, 100, 101] in order to seed the power amplifier at saturation. Since we are seeding the amplifier well below the saturation power, a threshold-like behavior is observed in the amplified power vs. pump power curves shown in Figure 2.12a), reducing the efficiency of the amplifier. While this one-stage amplification scheme is less efficient, it is much simpler because (1) there are no pre-amplifier components and (2) the pulses do not have to be stretched as much to avoid nonlinearity, since all the high power propagation is done in LMA fiber. A smaller stretching/compression ratio allows for looser tolerances on matching the higher-order dispersion of the stretcher and compressor. The 5 Watts of pump power wasted before the amplifier reaches saturation are not really of consequence, due to the low cost of high-power pump diodes.

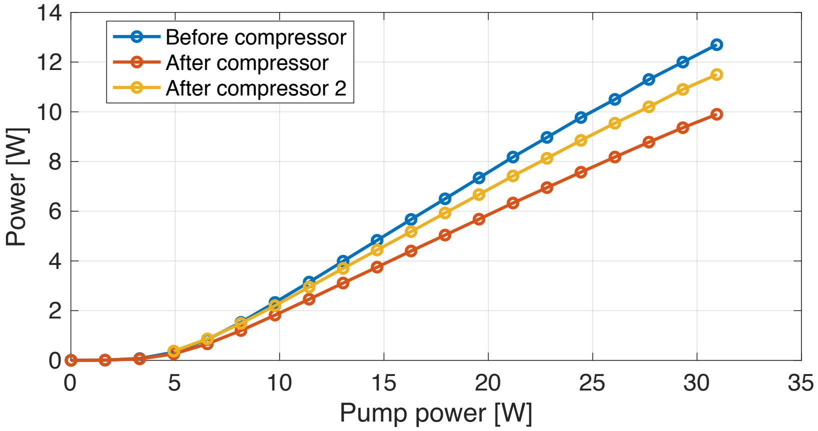

Figure 2.12: The chirped pulse amplification efficiency. The blue curve corresponds to the power measured before the grating compressor. The red and yellow curve are powers measured with two different seed spectra and powers.

Two concerns with underseeding the amplifier are (1) noise due to amplified spontaneous emission (ASE), [55] and (2) catastrophic damage to the amplifier fiber due to self-lasing and Q-switching. Regarding (1), despite the expectation of increased ASE, the measured RIN spectrum of the amplified light indicates that the main source of noise on the amplified light is due to the pump diode RIN, not ASE. Regarding (2), while we do not know what the lowest necessary seed power is to avoid catastrophic damage, we can say that we have run this PCF amplifiers at 1060 nm for many hours with seed powers as low as 10 mW without observing damage. We continuously monitor the seed light with a fast (100 MHz bandwidth) photodiode (PD) and a simple interlock circuit, shown in Figure 2.11, which immediately shuts off the pump diode in the event that the RF power from the photodiode drops below a set threshold, indicating reduced power or loss of mode locking. Pump diode drivers from VueMetrix Inc. shut off in less than 50 microseconds upon receiving an electronic signal, much shorter than the energy storage time in Yb of approximately 1 ms [102].

Another feature of this amplifier system to note is the operating wavelengths. The amplified light is at 1060 nm and the pump light is at 915 nm, whereas most ultrafast Yb amplifiers are pumped at 975 nm and amplify light at 1030-1040 nm, where the absorption and emission cross sections are largest [102]. We use 915 nm for the pump wavelength because the absorption feature at 975 nm is narrow, requiring tight control over the pump diode wavelength for efficient pumping. While the absorption cross section at 915 nm is three times lower, the absorption maximum there is also much broader, which loosens the requirements for controlling the pump diode wavelength, and thus temperature, considerably. With the long 5 m PCF, more than 90% of the pump light is still absorbed. For the amplified wavelength, we operate this laser at 1060 nm, far to the red of the Yb emission maximum, because one can amplify with considerably less gain narrowing, and this has also been employed in a few other linear CPA designs [61, 52]. Figure 2.13 shows the output spectrum of the amplified laser with more than 30 nm of bandwidth.

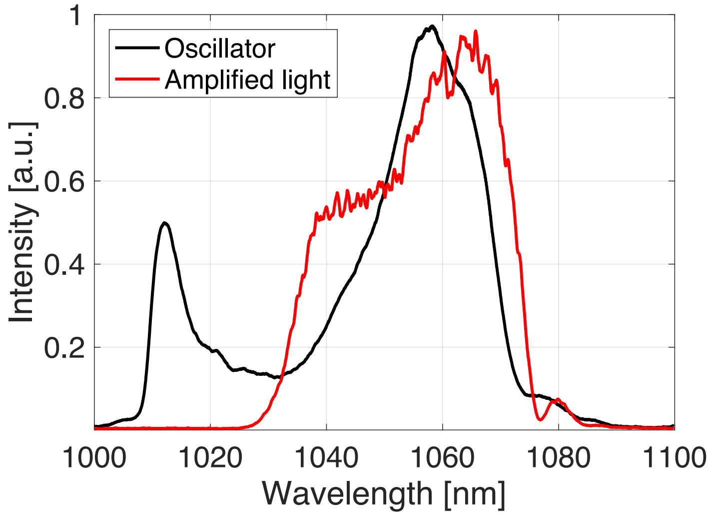

Figure 2.13: Comparison between the Yb: fiber oscillator spectrum and the amplified light spectrum after the compressor.

A dispersion budget for the CPA system following the oscillator is shown in table 2.1. The oscillator pulses are stretched to approximately 100 ps duration in the fiber stretcher module and compressed to <100 fs after amplification using a Treacy-style compressor with 1250 groove/mm transmission gratings (Wasatch Photonics). We measure an overall compressor efficiency of 77%, corresponding to a diffraction efficiency of $(77\%)^{1/4} = 94\%$.

Component	GDD (ps^2)	TOD (fs^3)	notes
Stretcher	1.65	-7.9×10^6	
Amplifier	0.095	2.06×10^5	FS, L_{tot}=5 m
Isolators	0.011	6.6×10^3	TGG, L_{tot}=8 cm
Compressor	-1.76	7.63×10^7	

Table 2.1: Dispersion budget for the 1060 nm laser. FS = fused silica. TGG = Terbium Gallium Garnet.

Figure 2.14 shows a second harmonic generation (SHG) frequency resolved optical gating (FROG) trace taken with the laser at full power using a commercial FROG system (Mesa Photonics FROGscan Ultra). While a free-space Offner-type stretcher [103] would allow for more tunability than the fiber stretcher module, and perhaps better compensation of higher order dispersion, [104] it would also add substantial mechanical complexity and cost. The fiber stretcher module is alignment-free, and we have observed nearly transform-limited performance.

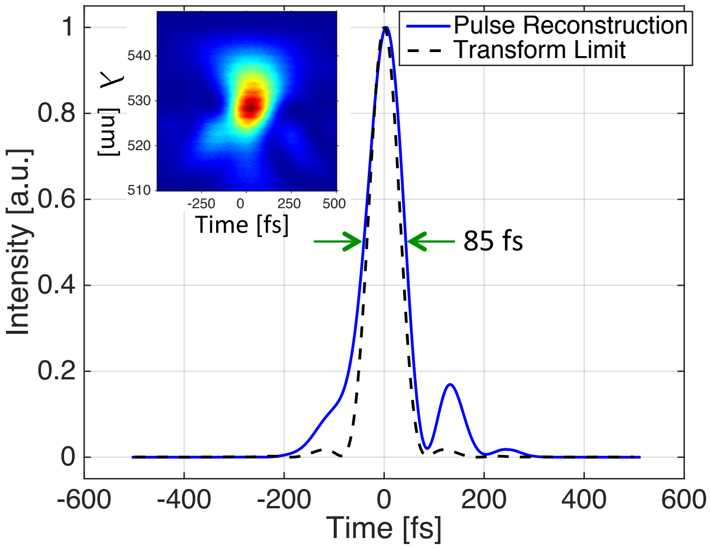

Figure 2.14: The raw FROG trace and the retrieved pulse shape of the compressed pulses compared to the transform limit calculated from the spectrum in 2.13.

2.4 Phase coherence of Yb:fiber laser

An important judge of the laser performance is the intensity noise and, for frequency combs, comb tooth linewidth. The linewidth of the heterodyned beat is analyzed with an RF spectrum analyzer and found to be between 10 and 30 kHz as shown in 2.15. This is just a rough estimate of the comb tooth linewidth from the beat of free-running Yb:fiber frequency comb laser and a continuous Nd:YAG laser with 1 kHz linewidth. The beat intensity decreases by about 3 dB when the RF spectrum analyzer resolution bandwidth is decreased from 30 kHz to 10 kHz.

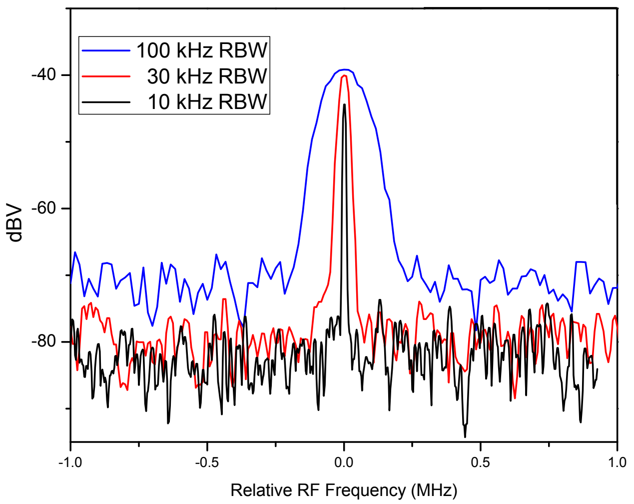

Figure 2.15: The beat signal between the free-running Yb:fiber frequency comb laser and a narrow linewidth cw Nd:YAG laser. The signal is measured with different resolution bandwidth of RF spectrum analyzer.

The relative intensity noise spectrum of the amplified light and the oscillator light are included in Figure 2.16.

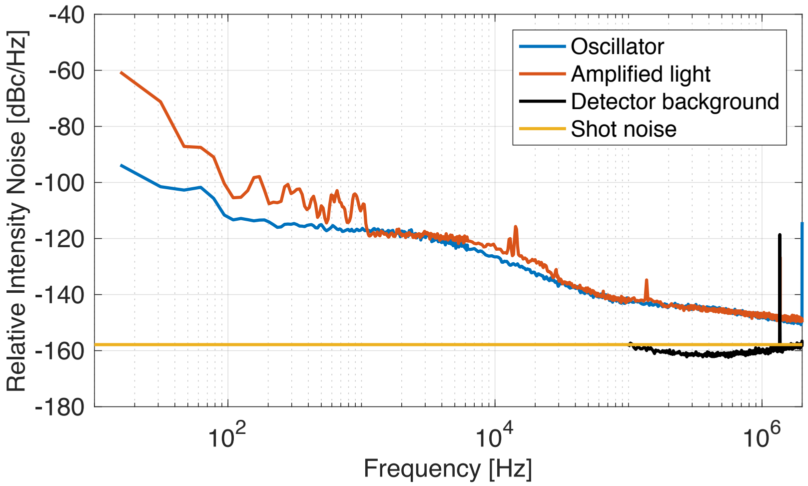

Figure 2.16: The RIN of the oscillator and amplified light. The shot noise is calculated using the photocurrent on the detector.

Chapter 3

Cavity-enhanced ultrafast spectroscopy

The principle of pump-probe signal enhancement is described in chapter 1. This chapter is dedicated to the technical details of cavity-enhanced ultrafast spectroscopy.

3.1 Overview of CE-TAS experimental setup

A diagram of the CE-TAS setup is shown in Fig. 3.1. The foci of two femtosecond enhancement cavities (fsEC's) cross at an angle of ~ 20 mrad above a nozzle where sample molecules are introduced in a supersonic expansion. Pump and probe pulses traverse the sample in the same direction to avoid broadening of the temporal resolution due to the transit time through the sample. High frequency modulation/demodulation techniques can still be employed for signal recovery without penalty as long as the modulation frequency is substantially lower than the cavity linewidths, but two complications arise in detecting the signal on the intracavity probe light. The first is that while the probe cavity enhances the signal, it also increases the amplitude noise on the transmitted light since the probe cavity turns the laser's frequency noise into amplitude noise [105]. This is commonly encountered in cavity-enhanced spectroscopy [23]. The second is that the supersonic expansion flow speed is not fast enough to replenish the sample within one cavity round trip, so that the sample is reused for approximately 3-10 pump-probe sequences, and the probe pulse measures not only femtosecond signals from the excited population immediately preceding it, but also nanosecond signals from several preceding pump pulses. This problem is unique to CE-TAS. Coherent molecular motion can be suppressed on nanosecond time scales by collisions with carrier gas [106] or the natural decay of the excited state (the likely case for most molecules of interest to ultrafast spectroscopy), but still a large ground-state bleach signal is expected to persist.

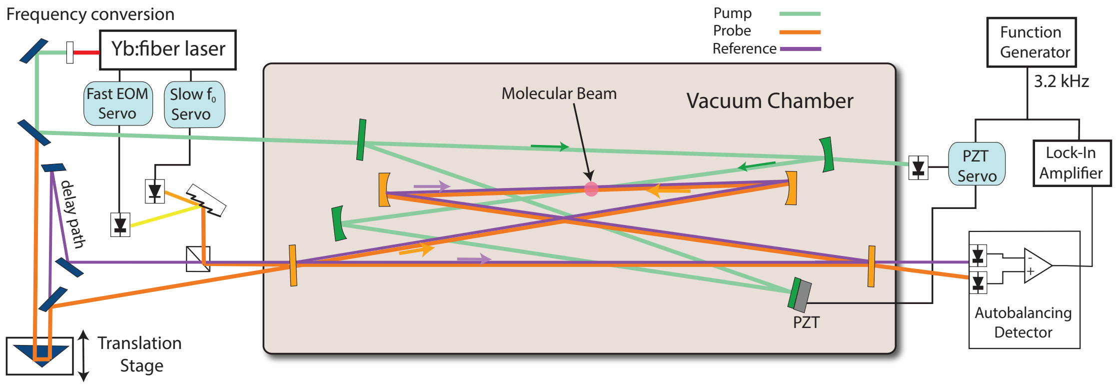

Figure 3.1: Schematic of the CE-TAS system. Ultrafast transient absorption experiments are performed in a molecular beam at the common focus of two optical resonators, one for the pump pulses and another for the probe pulses. Delayed counter-propagating reference pulses are used for common mode noise subtraction. The beams are color coded for clarity. More details are described in the main text.

We solve both of these problems by coupling a counter-propagating reference pulse train to the probe cavity and recording the difference between probe and reference pulses using an autobalance detector (Nirvana 2007, Newport, Inc.). The pulse sequence at the molecular sample is illustrated in Fig. 3.2a. The probe and reference pulses share common mode noise, but different signals. The probe pulse arrives shortly after the pump and records the femtosecond signal of interest, while the reference pulse arrives 6 ns later and samples the persistent bleach signal. Counter-propagation allows the reference beam to be easily separated from the probe beam in the ring cavity geometry and also reduces the concern for any parasitic coherent excitation it might produce, since this is effectively smeared out in time. Noise reduction is shown in Fig. 3.2b, where subtraction of the reference pulse reduces the relative intensity noise (RIN) on the intracavity light by more than 40 dB at the modulation frequency, allowing small signals to be recovered.

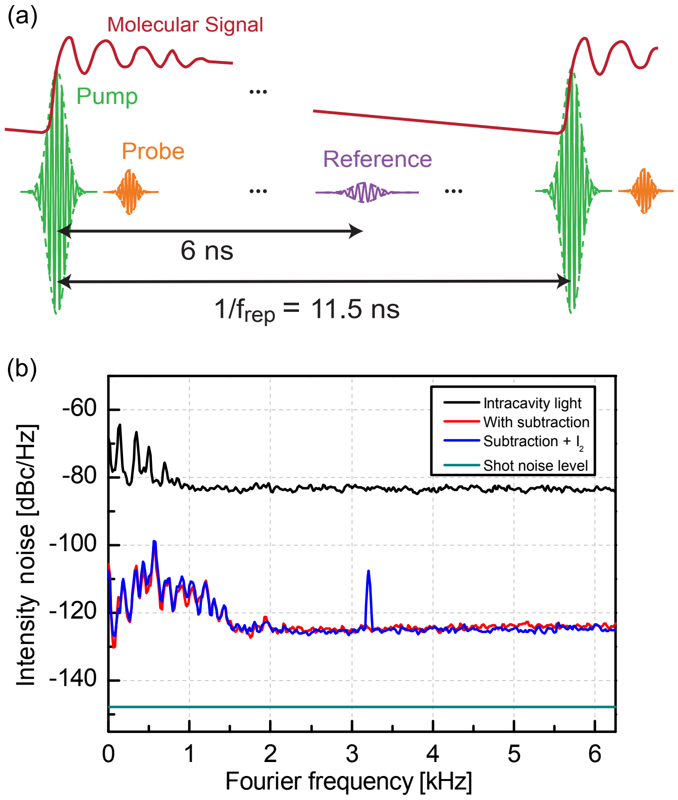

Figure 3.2: Noise subtraction. (a), Pulse sequence at the molecular sample. The probe and reference share common mode noise but sample different molecular signals. (b), Intracavity relative intensity noise (RIN) spectrum with and without subtraction of the reference pulse train. More than 40 dB of RIN can be suppressed. With the introduction of sample molecules, the signal at the pump modulation frequency of 3.2 kHz is observed.

3.2 Two cavity operation

3.2.1 Coupling one frequency comb to two cavities

In cavity-enhanced ultrafast spectroscopy experiments, we have one cavity for the pump and another cavity for the probe. It is highly unlikely that the carrier-envelope offset frequencies of the two cavities are the same since the f_0 is determined by the dispersion of the cavity mirrors. Moreover, in the ultraviolet pump and tunable visible probe experiments described in Chapter 5 - 7, the probe cavity dispersion is not constant across the whole tuning range. However, the pump and probe combs originate from the same frequency comb laser, which has only one f_o. We could tune the f_o of laser by tuning the laser oscillator intracavity dispersion to match either the pump or the probe cavity. To match the frequency comb laser's f_o to both cavities, we use different strategies in different experiments. The f_{rep} of all cavities can be done by matching the cavity lengths.

In the cavity-enhanced transient absorption experiment in iodine, both the pump and probe cavity are resonant for 529 nm. The cavity mirrors are simple quarter-wave stacks for this wavelength, which has low GDD at the design wavelength but a small available tuning range. The f_0 matching problem is solved by insertion of a $\sim 150\ \mu$m fused silica microscope cover slip at Brewster's angle in the pump cavity. Different cover slips were tried until one with the correct thickness was found. The f_o problem in the uv/tunable visible experiment is solved by using an optical parametric oscillator and the details are included in Chapter 5.

Both pump and probe cavities are mounted on an optical platform housed in a 2 ft. by 4 ft. rectangular vacuum chamber. The geometrical parameters of the pump and probe cavities (e.g., focal lengths, spot sizes) were chosen considering ease of alignment, interaction length in the sample, and the constraint that the cavities fit in this chamber. Overlap of pump and probe beams at the sample is obtained by aligning both cavity modes through a 100 μm diameter pinhole placed near the plane of the nozzle. This alignment cannot be optimized in-situ with the current mechanical design, but this could be accomplished by motorizing the pump cavity mirrors. Once the alignment of the two cavities are set, the pump-probe signal size is reproducible. However, the absolute signal size has a strong dependence on the pump-probe overlap, so realigning the pump and probe cavities usually results in a different absolute signal size.

3.3 Locking the pump and probe cavities

To keep pump and probe cavities on resonance for the experiment, we lock both cavities to the frequency comb laser. They are stabilized in different ways and schematically shown here.

3.3.1 "f_{rep} lock" of probe cavity

We use a two-point Pound-Drever-Hall (PDH) technique [107, 108] to lock the comb to the probe cavity. A schematic is shown in 3.3. The laser light is phase modulated at 2 MHz with an Electric-Optical Modulator (EOM) in the oscillator cavity at a modulation depth of 0.0074π. The modulation depth is calculated using the ratio of the modulation signal voltage sent to the EOM to the half-wave voltage of this EOM. The oscillator light is amplified and frequency converted to the desired wavelength, then sent to the probe cavity. The reflection from the cavity is the interference between the reflection from cavity input coupler and the transmission of intracavity light. The beam is dispersed by a grating onto two photodiodes, one for the "f_{rep} lock" and the other for "f_o lock". The photodiode (PD1) signal is mixed with 2 MHz sine wave in mixer 2, and this is the same frequency and waveform as the phase modulation signal sent to the EOM in the oscillator cavity. After passing two 1.9 MHz low pass filters (low pass filter 4), the 90 MHz laser repetition rate and the 4 MHz image frequency are eliminated, and this signal is used as the error signal for PDH lock. An example PDH error signal is shown in Figure 3.4. The error signal is sent to a PI^2D style loop filter (D2-125 Vescent Photonics), which has adjustable corner frequencies for the integrators and differential circuit. The servo output signal (Servo Out) is amplified in a high voltage amplifier and then combined with the 2 MHz modulation sine wave in a bias tee circuit. The combined signal is sent to the EOM in the oscillator cavity. The other output of the loop filter is the auxiliary output, which is an integrated servo output signal. This signal voltage is amplified in a homebuilt Piezoelectric transducer (PZT) driver circuit then sent to a PZT mounted in the manual stage for a plane probe cavity mirror. The feedback to EOM is fast but has limited travel, so the PZT is used to correct the slow drift of the probe cavity length.

This lock could also be done by locking the probe cavity to the frequency comb. One of the probe cavity mirrors was glued to a bullet style copper mount adapter as in [109]. A 2 mm thick PZT is glued to the back of one cavity mirror and the servo output signal is sent to the 2 mm thick PZT instead of the EOM. More servo bandwidth could be obtained using the EOM, allowing a higher gain at lower frequency. Using the PZT in the probe cavity locks the cavity but the intracavity noise is higher than locking the comb to the cavity.

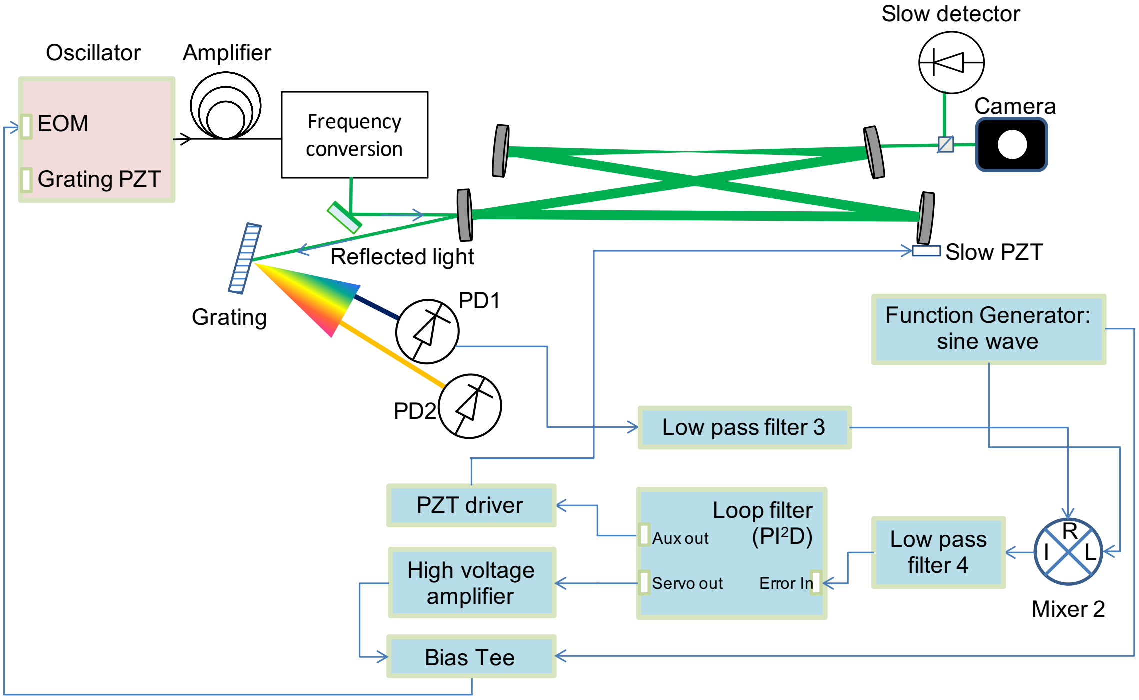

Figure 3.3: The schematic of "f_{rep} lock" of probe cavity. EOM: electrical optical modulator. PD: photodiode. PID: proportional-integral-derivative. Aux out: auxiliary servo output.

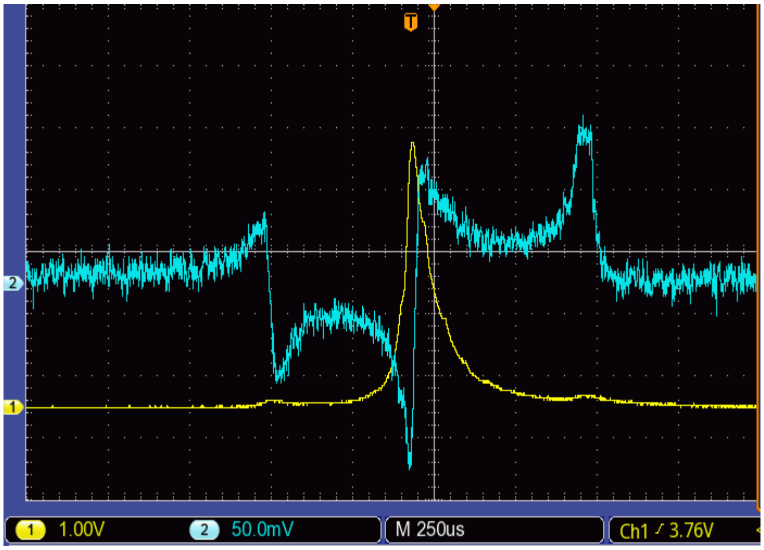

Figure 3.4: An example PDH error signal (blue trace) and cavity transmission signal (yellow trace) recorded by an oscilloscope.

3.3.2 “f_o lock” of probe cavity

The f_o is locked in a different way from f_{rep}. As we mentioned earlier, the dispersed probe cavity reflection beam are split by a D-shaped mirror. We record the reflected beam off the D-shaped mirror with another silicon photodiode PD2 and filter with a 1.9 MHz low pass filter to remove the repetition rate of the laser and the image frequency at 4 MHz. The filtered detector signal is mixed with the EOM modulation sine wave in mixer 1. This error signal has a similar waveform as the “f_{rep} lock” error signal. The error signal is integrated with a homebuilt integrator and amplified by a homebuilt piezo electric actuator driver to drive a ring shaped piezo transducer glued to the back of a transmission grating in the oscillator. The fixed points of the grating actuation is near the optical frequency whereas the fixed point for a pure f_o shift is at infinity. Changing the grating separation effectively changes the f_o while it has a much smaller influence on the repetition rate as discussed in section 2.1.4. This transducer characterization for tuning f_o and f_{rep} is shown in Chapter 2.

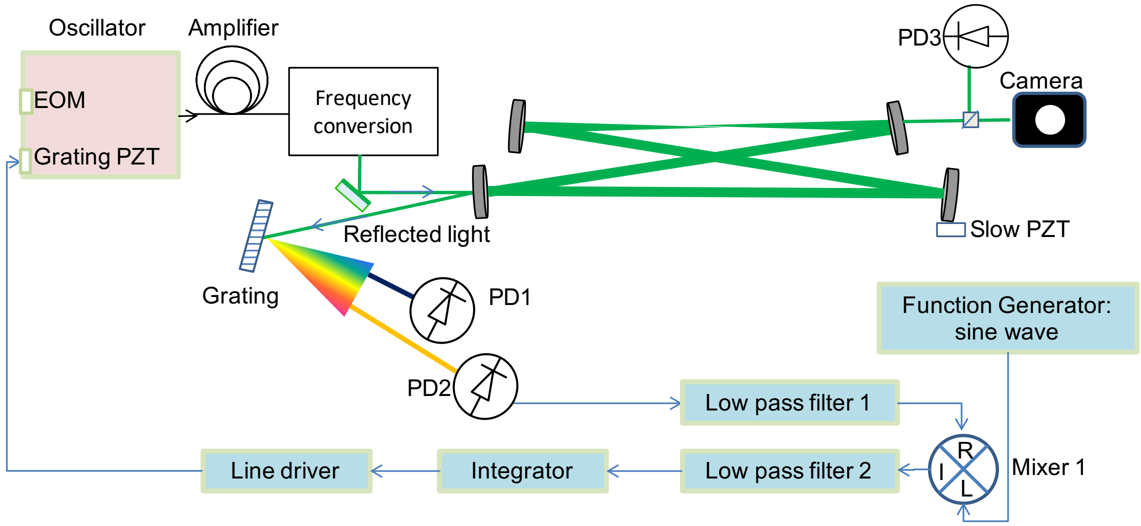

Figure 3.5: The schematic of "f_o lock" of probe cavity.

3.3.3 "Side-of-line" lock for pump cavity

In the spectroscopy experiment, we modulate the pump cavity at a few kHz for lock-in detection of the pump-probe signal. One way to do this could be to modulate the light incident on the pump cavity, for example with a mechanical chopper. However, this would make locking the pump cavity to the pump comb difficult since the intensity of the incident light is changing (or even vanishing in the case of a chopper). Instead, we intentionally detune the comb/cavity coupling for the pump cavity and use this detuning to modulate the intracavity pump power. This is done with a "side-of-line" lock method illustrated in Figure 3.6. Here the pump cavity transmitted light is used as the error signal and the servo feeds back on the cavity length to maintain an intracavity power set by a DC offset in the servo loop. By modulating this DC offset the intracavity power is modulated.

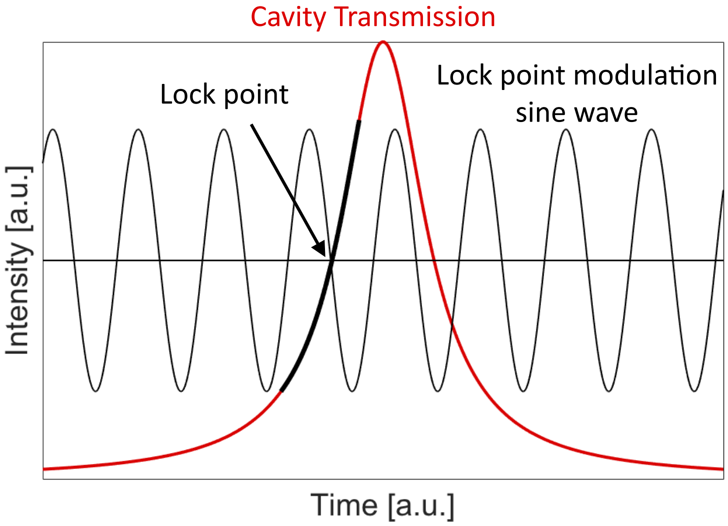

Figure 3.6: "Side-of-line" lock for pump cavity. The red trace represents the cavity transmission signal on a photodiode. The "lock point" is modulated with a 3.2 kHz sine wave.

Figure 3.7 includes a more detailed setup for this modulated pump cavity lock. The pump cavity transmission light is recorded with a silicon photodiode. This detector signal is used as the error signal, which is sent to a laser servo loop filter that's identical to the one employed in the probe lock. By sending a 3.2 kHz sine wave signal into the DC offset port, we modulate the cavity lock point with a sine wave, as discussed above. To minimize the effort required of the servo-loop, a "feed forward" sine wave of the same frequency is also sent from the function generator and added to the servo output in the line driver amplifier circuit. The relative phase of the two sine waves is set to minimize the amplitude of the 3.2 kHz signal at servo out. The servo-out signal is further integrated and sent to a slow PZT to keep the fast PZT in range in the same fashion as the probe cavity.

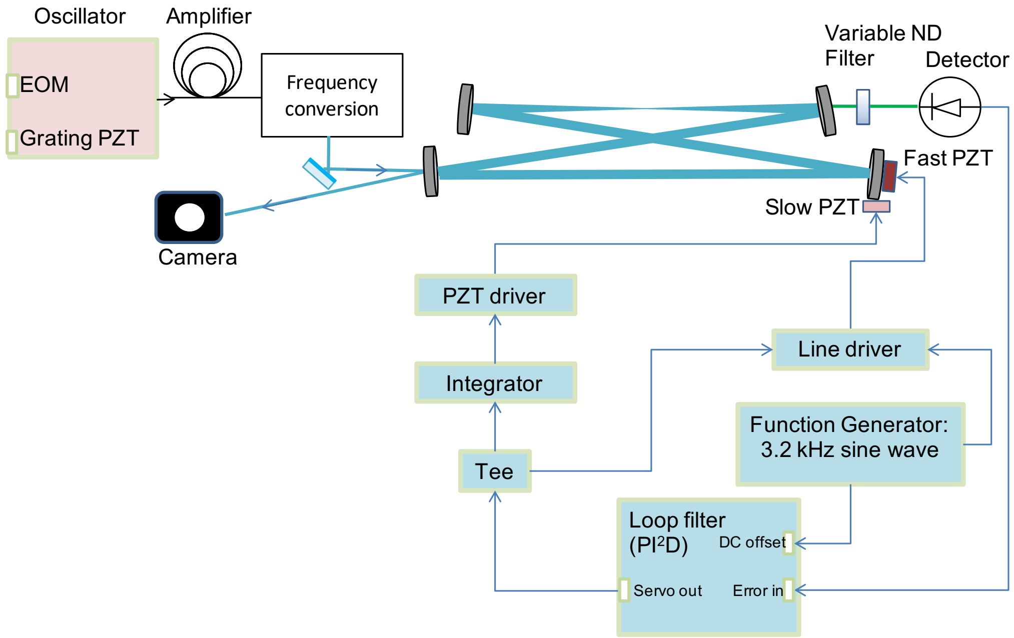

Figure 3.7: Pump cavity lock schematic.

3.4 Sample delivery pumping system

3.4.1 An overview of the molecular beam setup

The pump and probe cavities overlap at the focus and the angle in between is minimized to $\sim 1.5°$ to maximize the overlap interaction length at focus. The molecule-of-interest is delivered to the overlap of pump and probe cavities in a molecular beam. The supersonic expansion is formed by flowing about 300 to 1000 Torr of carrier gas to the vacuum chamber through a nozzle. Different nozzles and pumping setups are used in different experiments. For the experiment in I_2 described in the following chapter 4, a schematic of the vacuum setup is shown in Figure 3.8. The sample molecules in the reservoir cell is picked-up by the carrier gas and delivered to the overlap of pump and probe cavities through a small nozzle. The roots pump EH1200 and the roughing pump E2M80 (Edwards, Inc), generously provided by Professor Trevor Sears, handles the gas throughput from the molecular beam jet. The pressure in the chamber is maintained at a few mTorr by the turbo pump (OSAKA, TG900) attached to the chamber. A home-designed dry ice cold trap is used to effectively pump the I_2 in the chamber to mitigate the contamination of cavity mirrors without pumping the carrier gas.

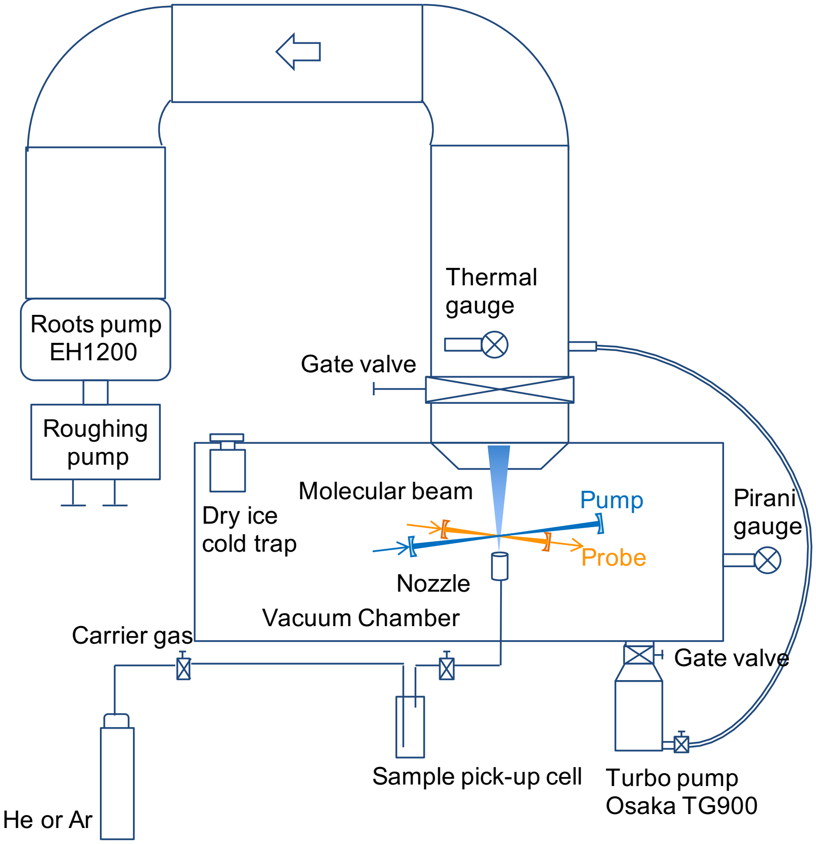

Figure 3.8: Sample delivery setup. Pump: pump cavity. Probe: probe cavity.

To apply cavity-enhanced ultrafast spectroscopy to neutral clusters formed in molecular beams, we need to have higher throughput than the setup used in the I_2 experiment. Multiple changes are implemented to the vacuum setup and a brief sketch of current vacuum setup is shown in Figure 3.9. The turbo pump that was attached to the vacuum chamber is removed from this setup. In the carrier gas line, a mass flow controller is installed to keep the flow rate constant so the supersonic expansion is reproducible. The supersonic expansion is pumped out by the roots pump EH4200 (Edwards, Inc). The smaller roots pump EH1200 and the roughing pump E2M80 (Edwards, Inc) are used as the backing pump for EH4200. For running a UV cavity in the chamber, we also continuously flow oxygen to the mirrors and backfill the chamber with argon to eliminate contamination problem of the cavity mirrors. A more detailed vacuum setup for the UV cavity is included in Chapter 5. A residual gas analyzer is installed to analyze the molecules in the supersonic expansion. The details about the gas detection using the RGA is included in a later subsection.

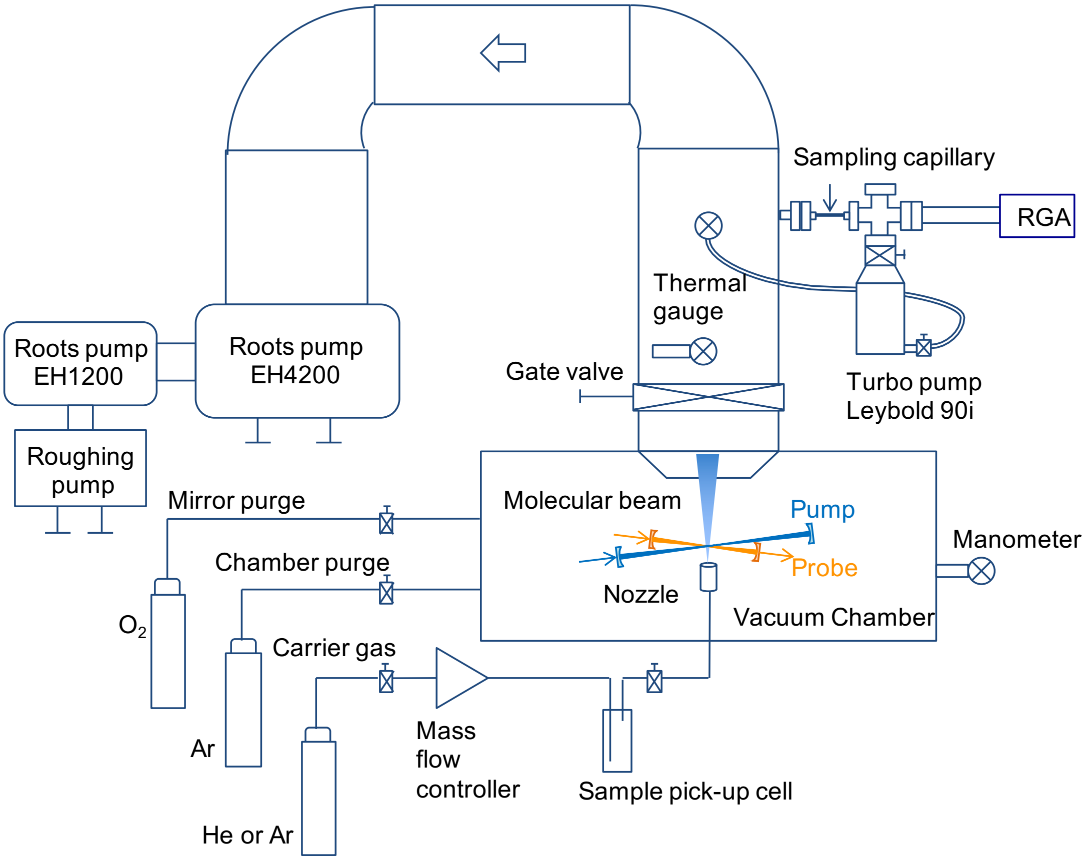

Figure 3.9: Sample delivery setup. Pump: pump cavity. Probe: probe cavity. RGA: residual gas analyzer.

3.4.2 Vacuum pumping calculation

Roots pumps are used for this vacuum setup to maintain operation of a continuous nozzle. Since the pump-probe experiment is done at the repetition rate of the frequency comb laser, which is between 87 MHz to 100 MHz in this thesis, we use a continuous nozzle since this is a too high frequency for a mechanically pulsed nozzle. Using pulse nozzles could reduce the gas load but also reduces the duty cycle of the experiment. All nozzles in this thesis are continuous. Therefore, the vacuum pumps are designed to handle a high throughput but we do not need high vacuum levels. The molecules experience supersonic expansion from carrier gas backing pressure $\mathrm{P_0}$ to the vacuum chamber $\mathrm{P_b}$. The chamber pressure $\mathrm{P_b}$ will limit how cold the molecules could get and how far from the nozzle we reach the shock wave boundary condition. The mach disk location can be calculated with Eqn. 7.6, where x_m is the mach disk location and d is the diameter of a round nozzle or the width for a slit nozzle [110]. In the work described in this thesis, we have nozzles of different sizes and shapes for different experiments. The smallest round nozzle used for the experiments has a diameter of 500 μm and the narrowest slit nozzle has a width of 200 μm. With a backing pressure at 760 Torr, to get a mach disk at 5 mm away from the slit nozzle, the highest chamber pressure is calculated to be 546 mTorr.

$$\frac{x_m}{d} = 0.67 \cdot (\frac{P_0}{P_b})^{1/2} \tag{3.1}$$

The lowest chamber pressure we could achieve depends on the throughput from the continuous nozzle and the pumping speed. To calculate the ultimate chamber pressure we could get with these pumps, we need the throughput from the nozzle and the effective pumping speed. The throughput in a free jet source is expressed as Eqn. 3.2. [111]

$$Q = C(\frac{T_c}{T_0})\sqrt{\frac{300}{T_0}}(P_0 d)d \tag{3.2}$$

$\mathrm{T_c}$ is the vacuum chamber temperature in K, $\mathrm{T_0}$ is the nozzle temperature in K, $\mathrm{P_0}$ is the backing pressure in torr, d is the nozzle diameter for round nozzles in cm. Numerical values of C depend on the gas species. $\mathrm{C_{He}}$ is 45 $\mathrm{L/cm^2/s}$ and $\mathrm{C_{Ar}}$ is 14 $\mathrm{L/cm^2/s}$. The $\mathrm{d^2}$ is equal to $4\mathrm{A}^2/\pi$ and A is the nozzle area. For the 200 μm wide and 5 mm long slit nozzle, A is 0.01 $\mathrm{cm^2}$. Assuming the chamber temperature is 300 K, backing pressure $\mathrm{P_0}$ is 760 Torr, we could get the throughput $\mathrm{Q_{He}}$ is 435 Torr·L/s and $\mathrm{Q_{Ar}}$ is 135 Torr·L/s.

The pumping speed of EH4200 is 2935 cubic foot per minute (cfm), or 1386 Liters/s. EH1200 pumping speed is 845 cfm, or 399 L/s. E2M80 pumping speed is 56.5 cfm = 27 L/s. The effective pumping speed of EH4200 with a backing pump of E2M275 (pumping speed: 206 cfm) is 1825 cfm. We use the EH1200 and E2M80 together as the backing pump, which has a backing speed of 495 cfm. Thus, it is reasonable to assume the effective pumping speed of EH4200 to be 2120 cfm (1000 L/s). Without including the conductance of the pipe connecting the vacuum chamber to the pumps, we get the pipe pressure as

$$P_b = \frac{Q}{S_{pump}} \tag{3.3}$$

The pipe pressure is 435 mTorr for He and 135 mTorr for Ar. However, we need to verify the pipe conductance does not have a significant effect on this pressure.

Before we calculate the pipe conductance, we need to determine the flow regime in the pipe. The carrier gas we use is He or Ar. The mean free path can be calculated by Eqn. 3.4.

$$\lambda = \frac{1}{\sqrt{2}\pi d_0^2 n} = \frac{kT}{\sqrt{2}\pi d_0^2 P} \tag{3.4}$$

d_0 is the diameter of the molecule, n is number density, k is Boltzmann constant, T is temperature and P is pressure. Diameter of He is 0.218 nm and of Ar is 0.364 nm. [112] The mean free path could be simplified to the following equations.

$$\begin{aligned} \lambda_{He} &= \frac{0.014\,[cm]}{P\,[Torr]} \\ \lambda_{Ar} &= \frac{0.0053\,[cm]}{P\,[Torr]} \end{aligned} \tag{3.5}$$

At the pipe pressure of 100 mTorr, λ_{He} is 0.15 cm and λ_{Ar} is 0.053 cm. The Knudsen's number $\mathrm{K_n}$ is calculated with the mean free path and the pipe inner diameter D. $\mathrm{K_{n\text{-}He}}$ is 0.15 cm/25.4 cm = 0.0059 and $\mathrm{K_{n\text{-}Ar}}$ is 0.053 cm/25.4 cm = 0.0021. For $\mathrm{K_n} < 0.01$, the flow is continuous and the gas-gas collision is the dominant collision. [112]

$$K_n = \frac{\lambda}{D} \tag{3.6}$$

In continuum flow regime, the conductance of long round pipes are expressed as Hagen-Poiseuille equation3.7. $\mathrm{P_1}$ is the upstream pressure, $\mathrm{P_2}$ is the downstream pressure, D is the pipe diameter, η is viscosity and Q is throughput.

$$C = \frac{Q}{P_1 - P_2} = \frac{\pi D^4}{128\eta l} \cdot \frac{P_1 + P_2}{2} \tag{3.7}$$

For Helium at 300 K, η is 19.9×10^{-6} Pascal·s. Q_{He} is 435 Torr·L/s, pipe length l is 5 meters, pipe diameter D is 25.4 cm. Assuming the P_1 and P_1 are the same, e.g. 435 mTorr for the sum term to begin, we could get P_1-P_2 = 1 Pascal = 7.5 mTorr. This verifies that the upstream and downstream pressures are very similar. The conductance of the pipe is calculated to be 5.9×10^4 L/s.

The effective pumping speed S_{eff} is then calculated using Eqn. 3.8

$$\frac{1}{S_{eff}} = \frac{1}{S} + \frac{1}{C} \tag{3.8}$$

The effective pumping speed is 983 L/s. The pipe pressure is then 443 mTorr, so reduction of pumping speed from the pipe conductance is negligible. At this pressure, the mach disk location is 5.6 mm away from the nozzle. This still sufficient for forming clusters in a supersonic expansion for some experiments explained in Chapter 7.

We experimentally measured the pipe pressure with supersonic expansion of He from the slit nozzle with this pumping setup. With a backing pressure of 660 Torr, the pipe pressure is 178 mTorr. This is measured without the mass flow controller installed in the line. The discrepancy with theory could be caused by several reasons, such as the pressure measurement is off since the pressure gauges are not calibrated, the actual nozzle opening is smaller than the design, or the pumping speed is higher than the calculation considering the estimation for EH4200 pumping speed is conservative.

3.4.3 Sample molecule detection with the residual gas analyzer

One diagnostic we have for the sample delivery in the supersonic expansion is a mass spectrometer in an residual gas analyzer (RGA). A 2 inches long stainless steel tubing with 1/8" inner diameter is used to sample the supersonic expansion exhaust line in the pipe. The pressure in the RGA is maintained to be lower than 10^{-6} torr for operating the electron multiplier in the RGA. A turbo pump (Leybold 90i) is used here to pump out the RGA. An example mass spectrum of 1-hydroxy-2-acetonaphthone molecule 3.10 is included. The signal drops to below the noise floor when the carrier gas for the supersonic expansion is closed. With this diagnostic, we are able to confirm the presence of sample molecules. This becomes a critical index particularly when we are setting up a new experiment and searching for the pump-probe signal.

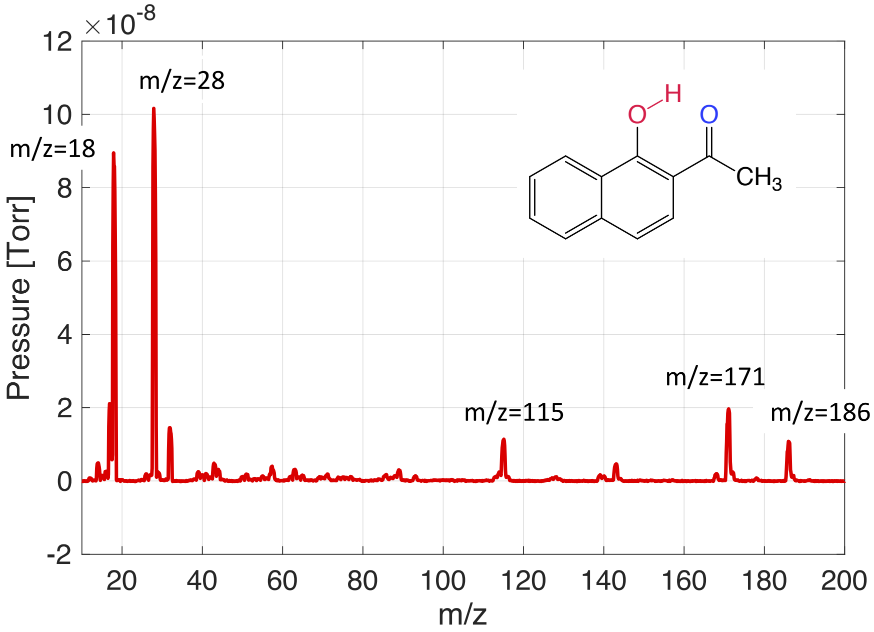

Figure 3.10: Mass spectrum of 1-hydroxy-2-acetonaphthone measured with the sampling setup. Peak m/z=18 is water, m/z=28 is N_2, m/z=115, 171 and 186 are 1-hydroxy-2-acetonaphthone.

Chapter 4

CETAS on I_2 and I_2:Ar clusters

To demonstrate cavity-enhanced ultrafast spectroscopy, we chose to study gas-phase molecular iodine (I_2) excited to the $B\ ^3\Pi_{0_u^+}$ state. The B state of I_2 has been extensively studied using both time-resolved and static spectroscopy [106, 113, 114] and thus is a good candidate for testing this new technique. A representative pump spectrum is included in Figure 4.1 with transition energies to vibrational states on B-state from X-state highlighted. Excitation to the bound B-state potential energy surface launches a vibrational wavepacket. In our experiment with pump and probe at the same wavelength, we expect to observe a bleach of the ground state absorption along with stimulated emission occurring when the wavepacket returns to the Franck-Condon region, as shown in Fig. 4.2a.

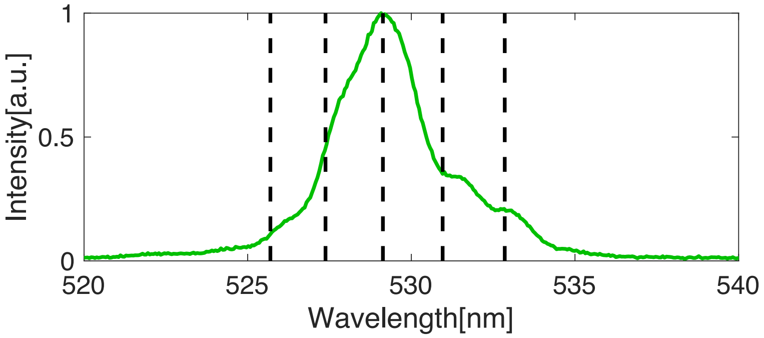

Figure 4.1: A representative optical spectrum of pump intracavity light. Each vertical line corresponds to an energy difference between a vibrationally excited state on the B-state and the zero point energy on X-state of I_2.

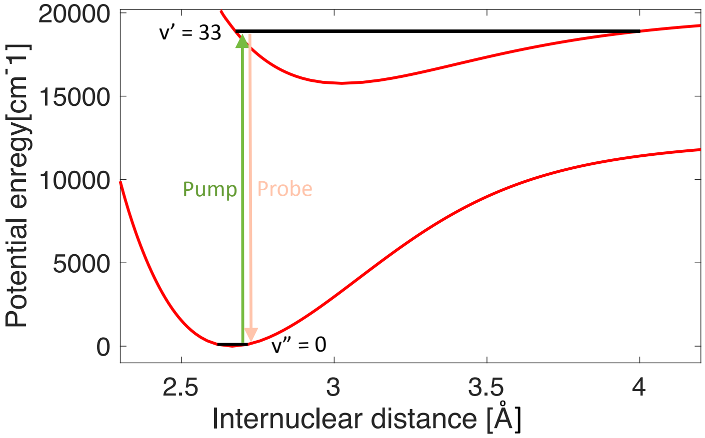

(a) The potential energy diagram of iodine. For simplicity, only the zero point energy and $\nu = 33$ vibrational states on the B-state are labeled in this figure.

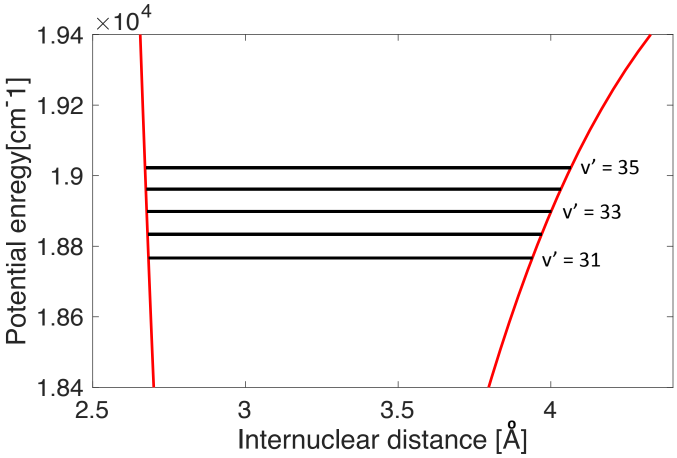

(b) The B-state potential energy curve with relevant vibrational states represented by horizontal lines. The pump spectrum is centered at 529 nm and primarily excites I_2 to three states around $\nu = 33$ state.

Figure 4.2: The potential energy diagram of I_2 [115, 116] with arrows illustrating the pump and probe measurement.

Vibrational energies between ν=31 state and ν=35 are listed in Fig. 4.3 below. [117] The beat frequencies and corresponding periods are calculated and included in Fig. 4.3b.

v’	Wavenumber [cm^{-1}]	Wavelength [nm]	Frequency [×10^{14} Hz]
31	18766.8672	532.8540	5.6262
32	18833.9309	530.9566	5.6463
33	18898.8899	529.1316	5.6675
34	18961.7422	527.3777	5.6846
35	19022.4879	525.6936	5.7028

(a) Selected vibrational energies of I$_2$.

Beating states	Beat frequency [THz]	Period [fs]
v’=34 & v’=35	1.8211	549.1
v’=33 & v’=34	1.8843	530.7
v’=32 & v’=33	1.9474	513.5
v’=31 & v’=32	2.0105	497.4
v’=33 & v’=35	3.7054	269.9
v’=32 & v’=34	3.8317	261.0
v’=31 & v’=33	3.9579	252.7
v’=32 & v’=35	5.6528	176.9
v’=31 & v’=34	5.8422	171.2
v’=31 & v’=35	7.6633	130.5

(b) Calculated beat frequencies and oscillation periods.

Figure 4.3: Tabulated vibrational energies between ν=31 and ν=35 on the B-state and the calculated beat frequencies.

4.1 Experimental setup

4.1.1 Frequency comb laser

Experiments are performed with the home-built 87 MHz Yb:fiber laser system described in Chapter 2. The oscillator’s net cavity group delay dispersion (GDD) is tuned to near zero GDD, but slightly anomalous, to give the quietist operation with a roughly 30 kHz free-running comb-tooth linewidth. The 9 W of 1060 nm frequency comb laser described in Chapter 2 is frequency doubled in a BBO crystal of 0.5 mm thickness. The crystal has a cut angle of 22.8° for type I phase matching of second harmonic generation at 1064 nm. The measured frequency doubling efficiency is 20%. The green beam goes through a beam splitter and about 80% of the power is sent to the pump cavity and the 20% goes the probe and reference.

4.1.2 Pump and probe cavities

The probe cavity is a nominally impedance matched four-mirror bow-tie ring cavity with two 50 cm radius of curvature concave mirrors. The two curved mirrors are ion beam sputtered high reflectors and the two plane mirrors are magnetron sputtered high reflectors that have a higher scattering loss than the curved mirrors. We measured the probe cavity finesse using a ring-down technique, as described in [37]. The result is shown in Figure 4.4. The measurement is taken by sweeping the cavity length over resonance faster than the cavity recovery time and recording the cavity transmission light with a fast photodiode. Using Eqn. 4.1, where l is the cavity length and P is optical power on the detector, the cavity finesse could be derived from the ring-down trace [26].

$$\frac{P(t)}{P_0} = e^{-\frac{2\pi c}{l\mathcal{F}}t} \tag{4.1}$$

Our cavity length matches the frequency comb laser repetition rate of 87.4 MHz. The ring-down times based on the fitting of these measurements spread between 0.64 μs and 0.70 μs. The cavity finesse is calculated to be between 353 and 384 with a mean value of 370. The absorption enhancement factor of approximately 120. The intracavity focus is calculated to be 70 μm FWHM. The cavity is locked with the two point Pound-Drever-Hall method described in Chapter 3.

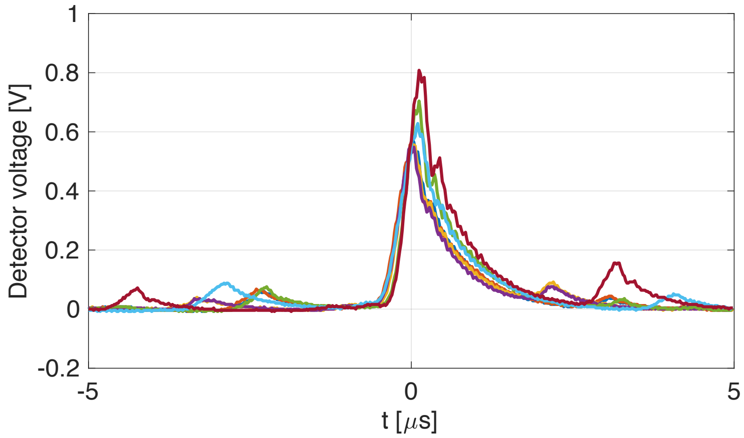

(a) Multiple ring-down measurements of the probe cavity.

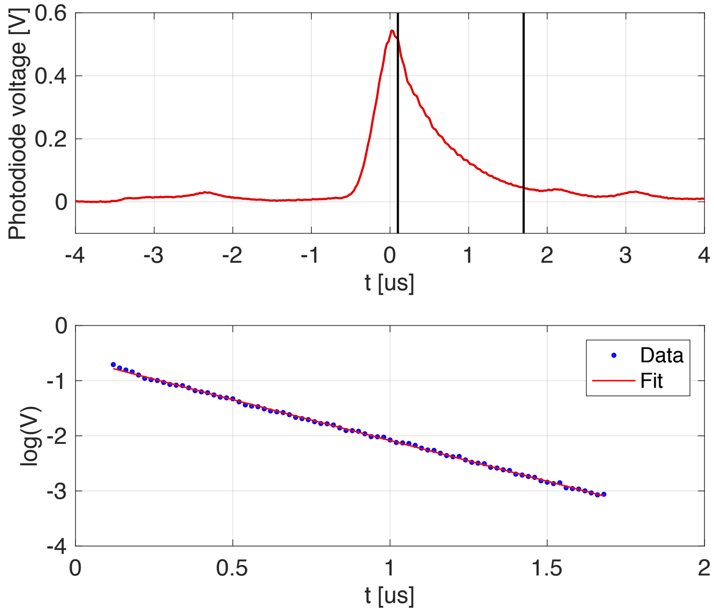

(b) One example ring-down. The bottom figure shows the natural logarithm of photodiode signal in the time interval labeled by black vertical lines in the middle figure. The linear fit is acquired using least squares fitting. The ring-down time for this measurement is 0.67 μs and a resulting cavity finesse is 367.

Figure 4.4: The figure shows the ring-down measurements of probe cavity. The cavity finesse concluded with these measurements is 370 ± 12.

The pump cavity is a four-mirror bow-tie ring cavity with a 110 μm focus formed by 75 cm radius of curvature mirrors. The pump cavity is strongly overcoupled [26], with the loss dominated by the 3% transmission of the input coupler. Calculations indicate that for the low finesse ($\sim$ 200) employed here, when the pump cavity's f_0 is the same as the laser's, changes in the intracavity pulse shape and delay are negligible as the intracavity pump power is modulated in this way. The pump cavity's f_0 is matched to the probe cavity by inserting a $\sim$ 150 μm thick cover slip at Brewster's angle in the pump cavity. The pump beam polarization is rotated by inserting a wave plate in the pump beam and re-orienting the intracavity cover slip.

4.2 Transient absorption measurement results and analysis

For introducing the I_2 sample, He or Ar carrier gas is passed through a room-temperature teflon pick-up cell containing glass wool coated in solid iodine powder and then expanded into vacuum through a 700 μm diameter nozzle. To decrease the amount of I_2 in the experiment, we merge this flow with a separate stream of pure carrier gas that bypasses the pickup cell, diluting the I_2 concentration. All components in the gas handling system downstream of the pickup cell, including the nozzle, are made of teflon to prevent undesired chemistry. The stagnation pressure was varied between 200 Torr and 760 Torr and the laser beams cross approximately 1 mm above the nozzle. The molecular beam is directed into a roots pumping system while the chamber pressure is maintained below 7 mTorr by a turbo-molecular pump and dry ice-cooled cold trap as shown in Figure 3.8.

Data is recorded by scanning the external delay stage and recording the subtracted signal (probe$-$reference) with a lock-in amplifier (SR830, SRS Inc.), generously provided by Professor Michael White. Typical pump-probe traces from a He-seeded expansion for both parallel and perpendicular polarizations are shown in Figure 4.5. Coherent oscillations of the B-state wavepacket are observed on top of a ground state bleach signal. A difference between parallel and perpendicular signals is observed near time zero and also at long delays around $\sim$110 ps. The rotational constant B in equilibrium position of I_2 at B state is 0.037 cm^{-1}. The revival time is T = 1/(2Bc) = 450 ps and 110 ps is about a quarter of the revival time. The ground state bleach and vibrational beat pattern slowly decay at long delays. The pressure broadening of I_2 has been measured to be 3.6 MHz/Torr for half-width at half maximum in He [118]. With a He carrier gas pressure of $\sim$ 500 Torr, the excited I_2 has a lifetime of about $\sim$ 44 ps. Since the pressure in the interaction region is lower than the backing pressure, the excited I_2 population decay due to the He pressure is longer than the estimated 44 ps and this is roughly consistent with the timescale at which the ground state bleach and vibrational beats decay in the measurement.

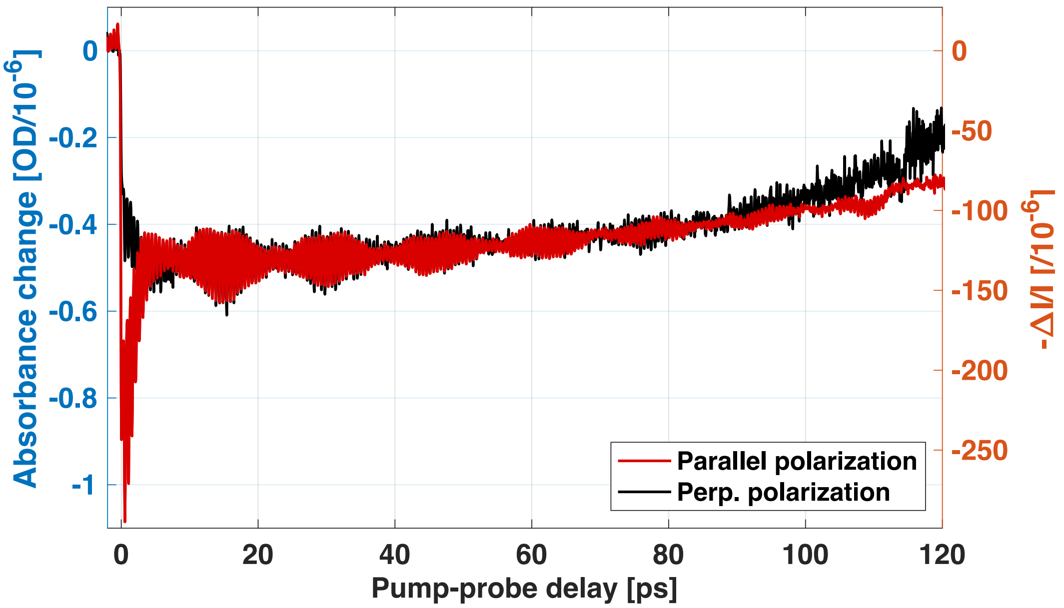

Figure 4.5: Measurements of a molecular wavepacket in the $B\ ^3\Pi_{0_u^+}$ state of I_2. Stimulated emission occurs when the molecule returns to the Franck-Condon region. Three vibrational states near $v = 33$ on the B-state surface are predominantly excited, giving rise to the observed vibrational beating pattern. Rotational motion causes a rapid decay of the polarization anisotropy. The perpendicular polarization data was taken under different conditions for the pump cavity and has been multiplied by 3.2.

The pump-probe trace with parallel polarizations in Figure 4.5 is Fourier transformed to a power spectrum shown in Figure 4.6. The vertical lines in all these spectra represent calculated quantum beat frequencies. Since the spectroscopy of I_2 has been done to very high precision, the beat frequency can be used to calibrate the step accuracy of the pump-probe delay stage actuator. A factor of 0.9965 is multiplied to the time-delay of pump-probe measurements to overlap the power spectrum peaks with the calculation. This is within the specifications of the step motor manufacturer's quoted step size uncertainty.

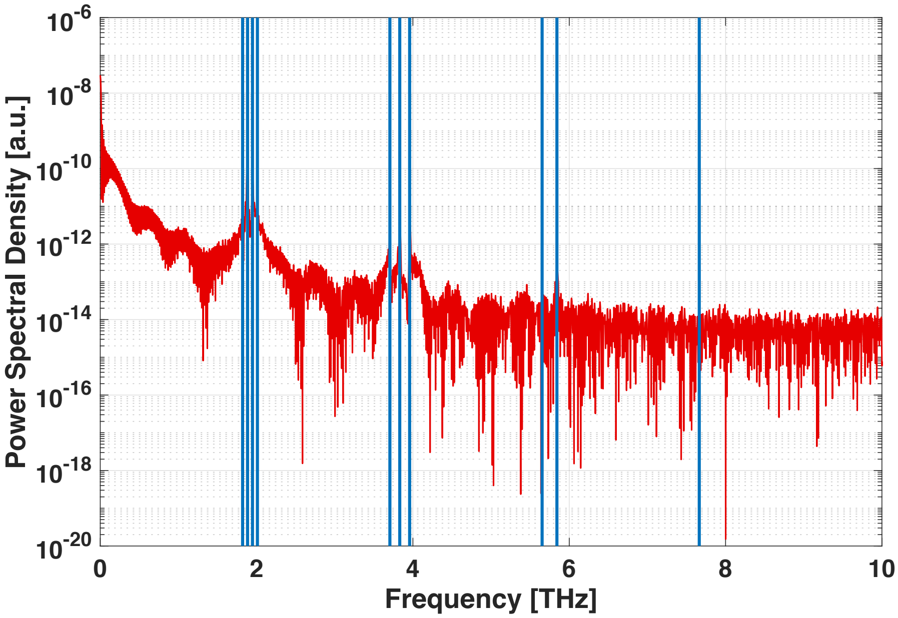

Figure 4.6: Fourier transform of the transient absorption measurement of I_2. Each vertical line corresponds to a vibrational beat frequency included in Fig. 4.3.

The enlarged views of the power spectrum density in Figure 4.7 show that the Fourier transform of measured transient absorption spectrum aligns well with the expected oscillation frequencies [114, 106].

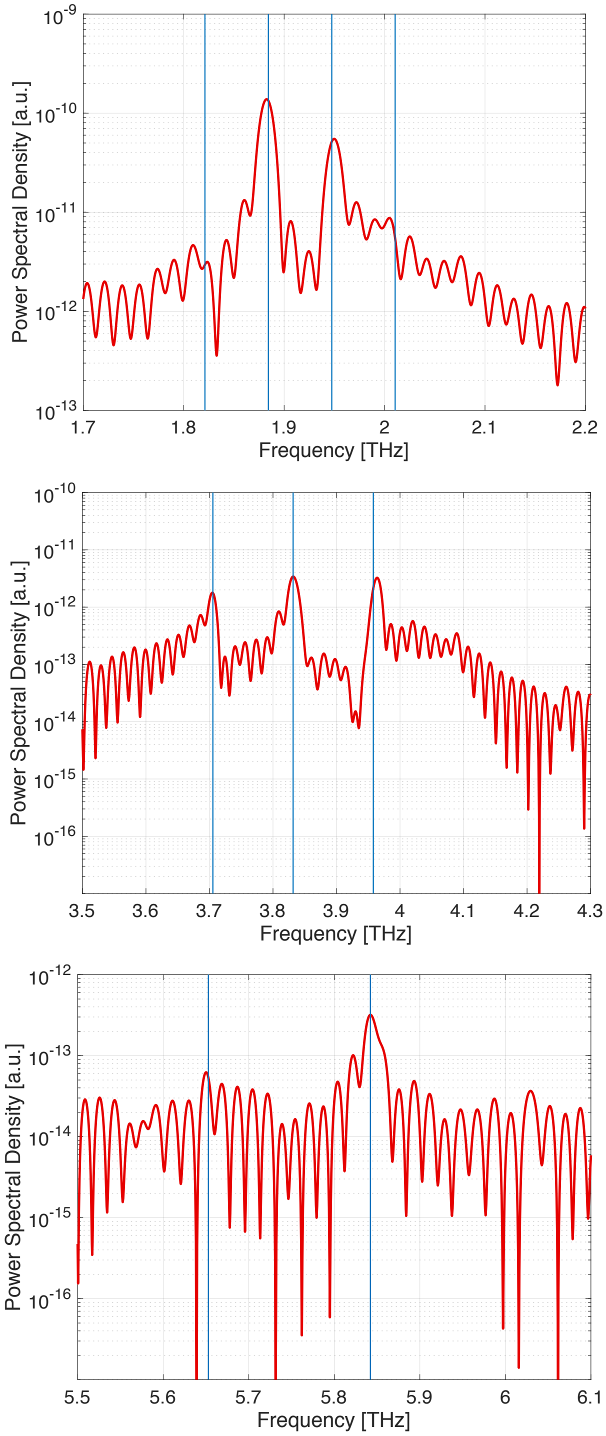

Figure 4.7: Detailed power spectra near the expected beat frequencies.

Since the pump spectrum is centered around 529 nm, excitation to ν=32, 33 and 34 are predominant. The vibrational dephasing period is calculated with Eqn. 4.2 using beat frequencies from Fig. 4.3 to be 15.8 ps, which is consistent with the measurement in Figure 4.5.

$$T = \frac{1}{f_{\nu_{32}\&\nu_{33}} - f_{\nu_{34}\&\nu_{33}}} \tag{4.2}$$

The right y-axis of the transient absorption spectrum in Figure 4.5 shows the fractional change in the transmitted light intensity ($\Delta I/I$) determined from the DC photocurrent at the autobalance detector (Nirvana 2007, Newport Inc.) and the calibrated lock-in gain. According to the manual of the lock-in amplifier (SR830, SRS Inc.) The lock-in amplifier output voltage is

$$\text{Lock-in output} = (\text{Signal/Lock-in sensitivity}-\text{Offset})\times\text{Expand}\times 10\text{V} \tag{4.3}$$

With Expand = 1 and offset = 0, the change in the probe cavity transmission intensity is calculated with

$$\Delta I = \text{Lock-in output} \times \frac{\text{Lock-in sensitivity}}{10} \times \text{Lock-in overlap integral} \tag{4.4}$$

Since the lock-in multiplies the signal with a pure sine wave at lock-in reference frequency and measures the single Fourier component (sine) of the signal, the lock-in overlap integral term is included in calculating ΔI. For example, if the signal is a peak-to-peak 2V square wave S(t), the square wave can be rewritten as a composition of many sine waves.

$$S(t) = 1.273 sin(\omega t) + 0.4244 sin(3\omega t) + 0.2546 sin(5\omega t) + \dots \tag{4.5}$$

$\omega = 2\pi f$, where f is the reference lock-in frequency. The measured signal is $1.273 sin(\omega t)$. $\Delta I/I$ is calculated with

$$\frac{\Delta I}{I} = \frac{\Delta I}{\text{DC}} \tag{4.6}$$

The left y-axis shows the change in the molecular ensemble's optical density (ΔOD), calculated from $\Delta I/I$ and the measured cavity finesse via

$$\Delta OD = -\log_{10}(e)\frac{\pi}{\mathcal{F}_{probe}}\frac{\Delta I}{I} \tag{4.7}$$

Systematic uncertainty regarding these quantities is estimated to contribute less than 20% error to the y-axis calibration. The uncertainty in the probe cavity finesse measurement as shown in Figure 4.4 is only about $\sim 3\%$. The largest uncertainty contribution is from whether the cavity is impedance matched or not. This probe cavity mirrors include two partial reflectors and two high reflectors. The cavity had a finesse of ~ 700 and operated in the impedance matched configuration before the experiments of I_2. At the time of taking the measurements on I_2 reported here, the cavity finesse decreased significantly to about 370. The decrease in cavity finesse is a result of I_2 contamination of the mirror coatings. With the ring-down measurements, it is unclear if the reflectivity decrease of partial reflectors and high reflectors are equivalent. In other words, we are not able to conclude if the cavity is still impedance matched for these measurements. However, the signal enhancement factor is rather insensitive when the cavity is close to impedance matched and we conservatively estimate a 20% uncertainty in the cavity enhancement factor.

For long delay scans, CE-TAS enjoys a practical convenience that pump/probe overlap is determined solely by the spatial modes of the pump and probe fsEC's, and is therefore insensitive to the translation stage position or alignment. If high-pressure argon is used as the carrier gas, a large coherent transient with a FWHM of 120 fs is observed before the oscillatory signal as shown in Figure 4.9 and this is used to estimate the temporal resolution. This is consistent with the observed rise time of the ground state bleach signal as shown in Figure 4.16 (a), where the pump-probe delay step size is 50 fs.

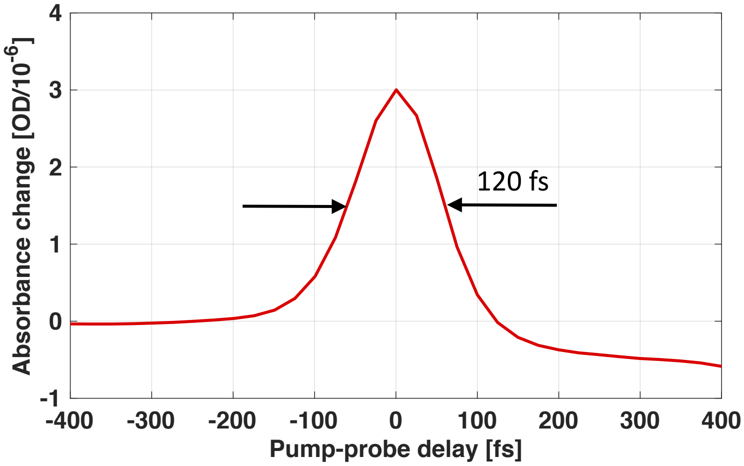

Figure 4.8: Transient signal at timezero of I_2 in Ar-seeded supersonic expansion. The two arrows indicating 120 fs apart at FWHM in the figure is for eye-guiding.

The I_2 in Ar measurement is also used to determine the zero of the delay axis by using the large transient signal from I_2 and Ar. This large transient timezero signal is only observed with Ar as the carrier gas, but not with He. Depending on the alignment, this transient signal with both positive and negative signs have been observed. The temporal spacing between the first peak and the time-zero transient is 530.7 fs, corresponding to the strongest beat between ν=33 and ν=34.

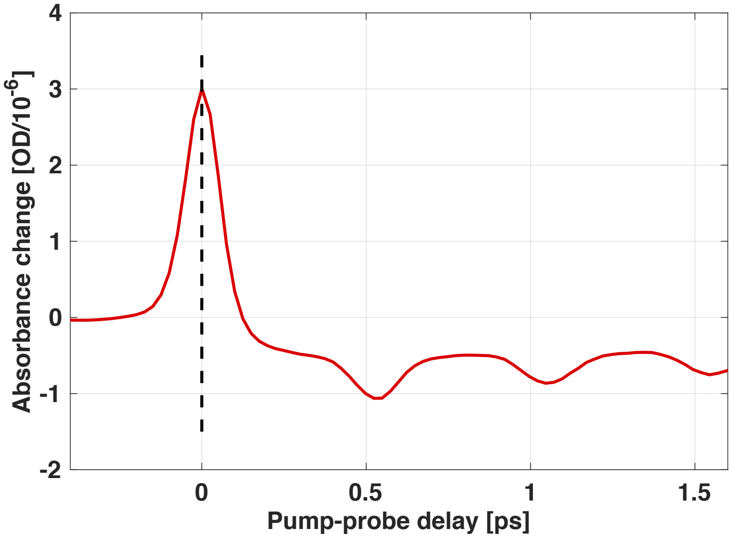

Figure 4.9: Time zero calibration with the transient absorption signal of I_2 in Ar-seeded supersonic expansion.

An additional concern with the CE-TAS scheme arises from the potential distortion of the intra-cavity pulse shape due to absorption from background gas in the vacuum chamber. This is particularly true for a molecule like I_2, with sharp spectral features that can cause the probe pulse to develop a wake. Indeed, when flowing large amounts of I_2 gas, we observe a small oscillatory signal before time zero due to this wake. The appearance of this signal coincides with the onset of I_2 absorption lines becoming barely visible in the intracavity light optical spectrum (Fig. 4.10(c)). This artifact becomes negligible when the I_2 flow is reduced, as shown in Fig. 4.10(b). As in other forms of cavity-enhanced spectroscopy, the total absorption of the analyte should be kept small with respect to the cavity mirror losses to avoid distortions of the signal.

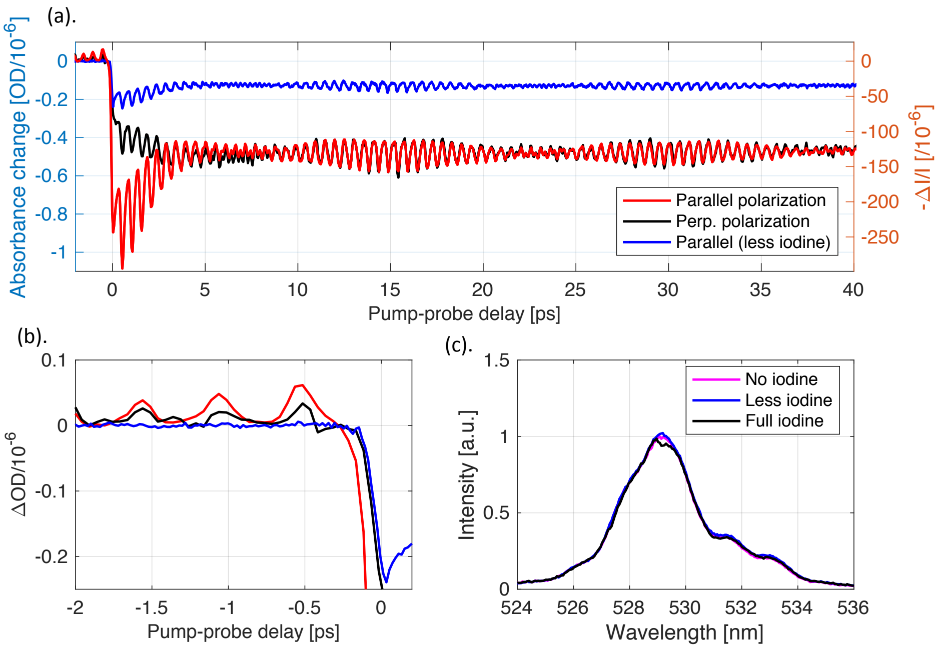

Figure 4.10: (a), Cavity-enhanced transient absorption measurements in I_2. The parallel polarization and perpendicular polarization traces are the same as in Fig. 4.5. The blue trace is measured with less iodine by diluting the I_2 concentration in the beam by merging the flow from the pickup cell with pure carrier gas. If the partial pressure of I_2 in the vacuum chamber gets too high, an artifact of the CE-TAS scheme is visible before time zero due to distortion of the intracavity pulses. This artifact is effectively eliminated by reducing the gas flow. (b), A zoom-in view of the traces in (a) before time zero. (c), The intracavity light spectrum is also visibly distorted when the artifact appears.

Another potential issue with CE-TAS instrument is that the molecular beam flow speed is not high enough to replenish the sample at 90 MHz. In the molecular beam setup with He as the carrier gas, the maximum flow speed of He can be calculated with [111]

$$V = \sqrt{\frac{2R}{W}(\frac{\gamma}{\gamma - 1})T_0} \tag{4.8}$$

R is the gas constant, W is the molecule's molecular weight, γ is 5/3 for He in a supersonic expansion from a round nozzle and T_0 is the carrier gas temperature. For He, the highest flow speed can be 1766 m/s. If we assume the I_2 flow speed is 1000 m/s, it takes 110 ns for the molecular beam to flow through the pump cavity focus (w is 95 μm). For pulses at a repetition rate of 87.4 MHz, the time interval between pulses is about 11.5 ns. In other words, the molecules are estimated to get excitations from 10 pulses on average.

Here we include an estimation of the pump excitation ratio in I_2 with 10 W pump power at 87.4 MHz repetition rate. The pump peak fluence in photons/cm^2 is

$$J = \frac{2P_{pump}}{\pi w^2 f_{rep} h\nu} \tag{4.9}$$

The pump cavity is focused to a beam radius of w = 95 μm. When excited at 530 nm, the absorption cross-section of I_2 is 3×10^{-18} cm^2. [119] The excitation ratio is calculated to be $\eta = J\sigma = 0.65\%$. At the highest pump powers ($\sim$ 50 W), we estimate that the pump pulse excites about 3.2 percent of the I_2 molecules.

As mentioned in Chapter 3, the light in pump cavity is modulated by modulating the lock point with a sine wave. The modulation depth is not 100% and the pump cavity transmission is a slightly distorted sine wave as shown in Figure 4.11. Each time the pump cavity re-locks, the pump cavity transmission has a slightly different waveform. As a result, the overlap integral between the pump power and a sine wave requires calibration each time the pump cavity locks. A second lock-in amplifier is now installed to record the pump cavity transmission to eliminate this problem for future experiments.

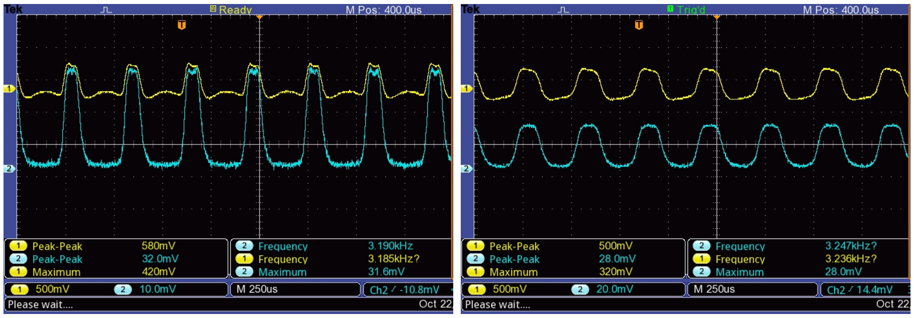

Figure 4.11: Two example pump cavity transmission waveforms. The blue traces are the pump cavity transmission signals recorded by a silicon photodiode. The yellow traces are the error signals for the pump cavity lock.

We took a series of measurements on I_2 in He-seeded supersonic expansion with an average pump intracavity power between 1.0 W and 20.3 W and all traces are shown in Figure 4.12. The average pump intracavity power was adjusted by sliding a neutral density filter in the cavity transmission beam for the lock error signal. All the other conditions, such as the pump modulation depth, are kept close to be the same with our best effort. The ground state bleach signal size shows no significant increase for pump powers higher than $\sim$ 10 W. The ground state bleach signals between 5.5 ps and 7.5 ps are averaged and included in Figure 4.13. As we calculated earlier, 10 W pump power corresponds to a single pass excitation fraction of 0.65%. The measurements are taken at 1 mm above the supersonic expansion nozzle, where the flow speed of gas is slower than V given by eqn. 4.8. The I_2 molecules can potentially excited by more than 10 pulses to a resulting excitation fraction higher than 6.5%. Still, the saturation of signal at this excitation ratio is surprising and these measurements should be repeated. Further investigation, varying the nozzle position, carrier gas, etc., should also be done.

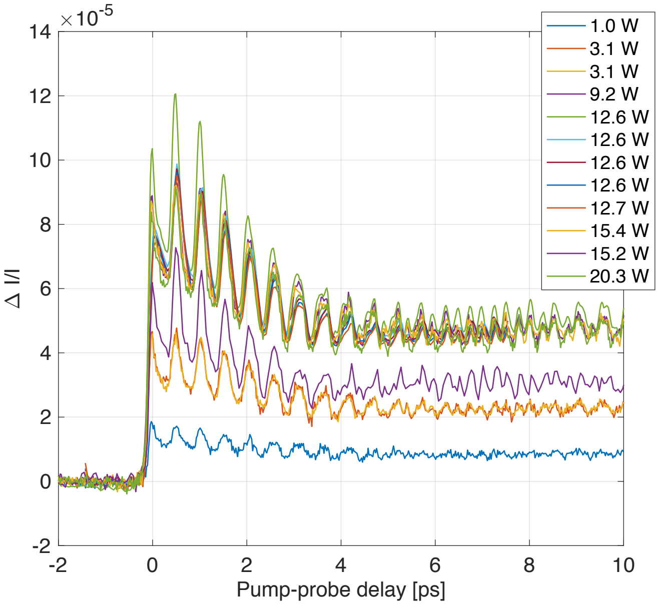

Figure 4.12: Transient absorption measurements with intracavity pump power ranging from 1.0 W to 20.3 W.

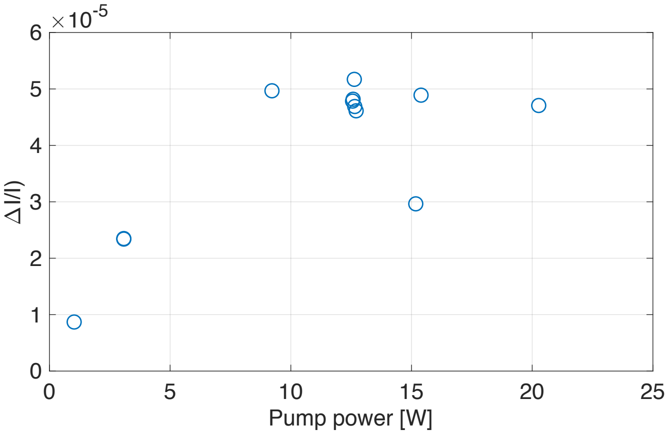

Figure 4.13: The mean of ground state bleach signal size between 5.5 ps and 7.5 ps pump-probe delay shows saturation of transient absorption at around 10 W pump power.

As shown in Figure 4.14, over this wide range of average pump intracavity power, the shape of pump-probe signal remains unchanged.

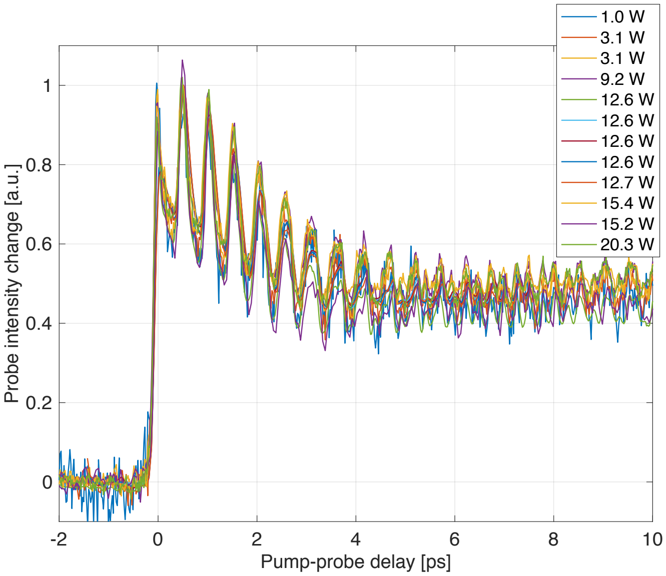

Figure 4.14: Transient absorption measurements with intracavity pump power ranging from 1.0 W to 20.3 W. All traces are scaled to overlap.

Another test of how the transient absorption signal size scales with the pump power is measured with the probe light is coupled to the probe cavity while the pump is not coupled to the pump cavity. In the pump beam path, a chopper is used instead to modulate the pump power and the resulting pump power has a square wave form.

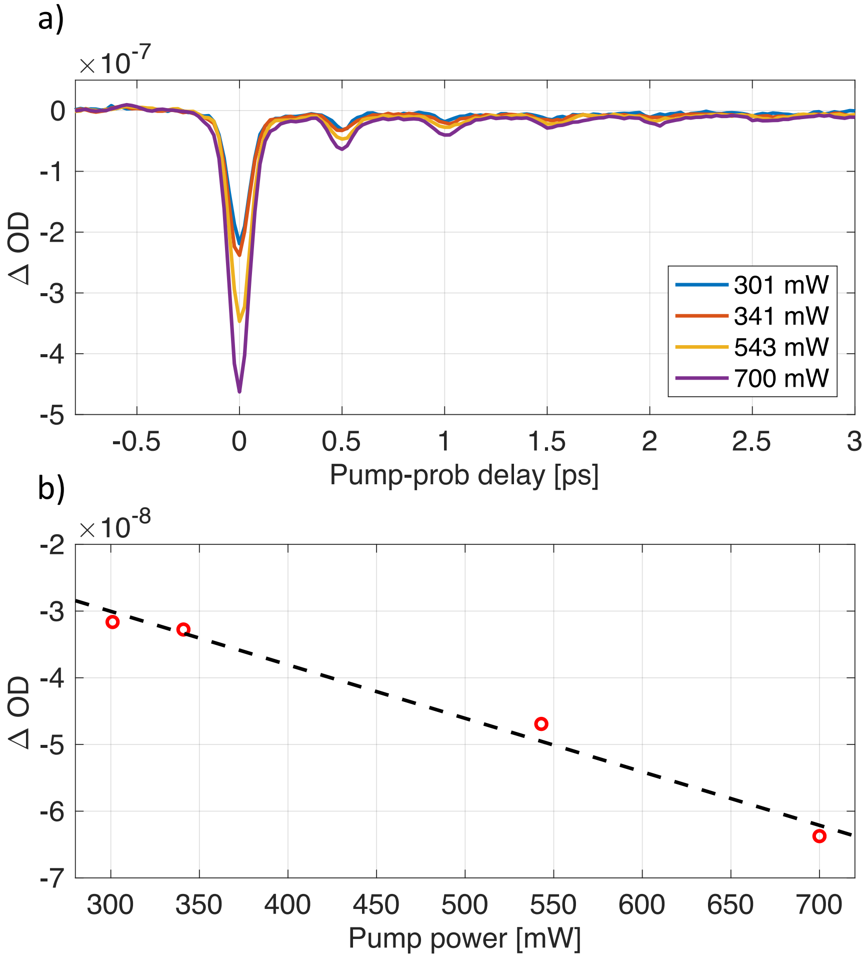

Figure 4.15: a). Transient absorption spectrum of I_2 in He-seeded supersonic expansion at pump powers from 301 mW to 700 mW. b). The height of the peak at 0.5 ps pump-probe delay and the linear fit of the peak heights. These data are taken with a chopper in the pump beam and no pump cavity.

By varying the pump power over a factor of 2, we verified that the pump-probe signal is linear to the pump power in this range. one thing to note when comparing data taken with different setups is that I_2 actually represents a pathological case for this setup, in that the vibrational beat pattern depends very sensitively on the pump and probe light spectrum and the vibrational states probed.

4.3 Noise performance of cavity enhanced ultrafast spectroscopy

The noise performance of cavity-enhanced ultrafast spectroscopy is evaluated in two independent ways. One is using the RIN measurement as presented in Chapter 3 Figure 3.2. The probe light RIN data shown in Figure 3.2 is at -125 dBc/Hz and the lock-in detection only detects the in-phase component, so the noise is 3 dB lower. This gives a noise level in ΔI/I of $10^{-128/20}/\sqrt{Hz} = 3.9 \times 10^{-7}/\sqrt{Hz}$. Using equation 4.7 with $\mathcal{F}/\pi = 120$, we get the noise in terms of ΔOD is $1.4\times10^{-9}/\sqrt{Hz}$, assuming white noise limited performance.

The other way we examined the noise performance of CE-TAS is as following. We reduced the I_2 flow as low as we stably could with the gas-handling system of that time and recorded 60 consecutive scans over a 1 hour period. Each scan, the data are taken for 0.5 s per delay point with perpendicular polarizations and 50 fs step size, for a total accumulation of 30 s per point. Figure 4.16(a) shows every 10th scan along with the average of the complete data set. The error bars in Fig. 4.16(a) are the uncertainty in the mean, calculated simply as the standard deviation of the 60 consecutive measurements divided by $\sqrt{60}$. The error bars have a mean size of $\Delta OD = 2.0 \times 10^{-10}$ averaged over all delays with a standard deviation of 2×10^{-11}. White noise performance is supported by an Allan deviation analysis, shown in Fig. 4.16(b) with the slope of -1/2 on the log-log plot [26]. This then indicates a sensitivity integration time of $2.0 \times 10^{-10} \times \sqrt{30 \text{ s}} = 1.1 \times 10^{-9}/\sqrt{Hz}$. Considering the very different ways these measurements are taken, this is excellent agreement. We report the sensitivity to one significant figure as $\Delta OD = 1 \times 10^{-9}/\sqrt{Hz}$, and our demonstrated detection limit in a practical transient absorption experiment, where averaging time must be distributed over many pump-probe delays, as $\Delta OD = 2 \times 10^{-10}$.

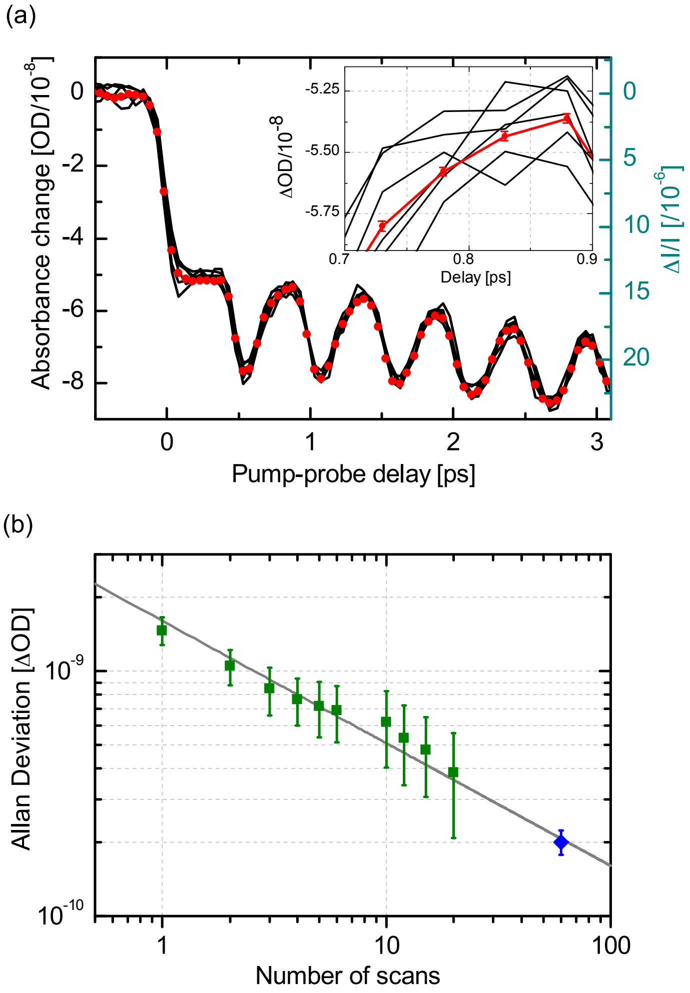

Figure 4.16: Noise performance of CE-TAS. (a), Transient absorption measurements taken with reduced gas flow and perpendicular polarizations. The red dots represent the average of 60 consecutive scans taken over a 1 hour period. Black curves are every 10th scan from the data set. Inset: Zoom-in around 0.8 ps delay. Error bars represent the uncertainty in the mean. (b), The green squares show the average of the Allan deviations obtained independently for each delay point. Error bars here are the standard deviation (not the uncertainty in the mean) of this ensemble, to represent the spread in the data. The blue diamond is the average of the error bars of (a), along with their standard deviation. The grey line has a slope of -1/2 on the log-log plot, the expected slope for white noise performance.

4.4 CE-TAS measurement of I_2:Argon clusters

The cavity-enhanced ultrafast spectroscopy is motivated with studying dynamics in neutral clusters in molecular beams. To experimentally verify that cavity-enhanced ultrafast spectroscopy can be applied to clusters, we replaced the round nozzle with a slit nozzle and seeded the expansion with Argon instead of Helium to to obtain clusters [120]. The nozzle is a 5 mm long × 200 μm wide slit nozzle 3D printed with PEEK plastic for compatibility with I_2. With many Ar atoms to collide with, the vibrations of the excited iodine molecules are rapidly quenched [120, 121], as a result, the vibrational beat pattern seen in He-seeded expansions is expected to be suppressed. Figure 4.17 shows the transient absorption measurements in I_2 formed in an Ar-seeded supersonic expansion. The pump and probe beams are 6 mm above the nozzle and the backing pressure of Argon is increased from 260 Torr to 460 Torr. As the Ar pressure increases, the coherent transient peak at timezero increases and subsequent oscillations decreases. This is showing the clustering between I_2 and Argon and demonstrating we have the sensitivity to perform ultrafast transient absorption measurements in dilute cluster beams.

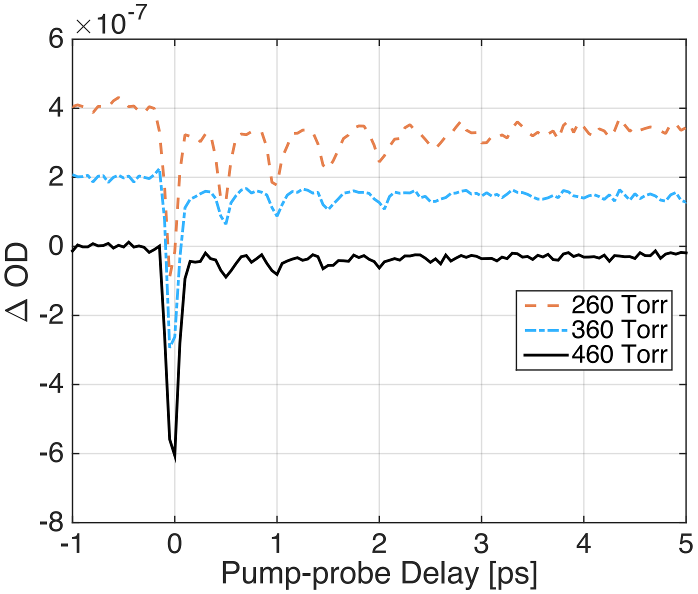

Figure 4.17: CE-TAS measurement of I_2-Ar clusters in a supersonic expansion from a slit nozzle. The Ar backing pressure is increased from 260 Torr to 460 Torr. The traces are offset for clarity.

Chapter 5

Towards widely tunable cavity-enhanced ultrafast spectroscopy

The CETAS experiments on iodine and iodine-argon clusters in supersonic expansions have shown the sensitivity of the technique is sufficient for studying ultrafast dynamics in molecular beams. To map out the energy distribution and structure changes in more complex molecules, we need to take pump-probe measurements at multiple different wavelengths. The exact spectral range depends on the energy for the transition and the molecules of interest. This thesis describes the development for a spectrometer at ultraviolet and tunable visible. More specifically, this chapter summarizes work on the instrument advances, including generation of UV light, the UV enhancement cavity, the visible enhancement cavity, the molecular beam setup, and technical details of the widely tunable spectrometer, etc. Demonstration of tunable visible frequency comb generation and stabilization are included in next chapter.

5.1 Seeding the Yb:fiber amplifier

As introduced in Chapter 2, there are two different oscillators used for work included in this thesis. One is the homebuilt Yb:fiber oscillator depicted in Chapter 2. The oscillator output is sent to the fiber stretcher then used to seed the Yb:fiber LMA fiber amplifier. This is used for the supercontinuum generation in Chapter 6. The other oscillator is the commercial mode-locked Er:fiber frequency comb laser (Menlo ULN, Menlo, GmbH). The Er:fiber comb is amplified in a home-built Er:fiber amplifier and shifted in dispersive wave to 1060 nm in a highly nonlinear fiber assembly. The light is amplified in a homebuilt Yb:fiber amplifier to seed the large mode area fiber amplifier and achieves 11.3 Watts of 1060 nm light after the compressor.

5.2 SHG and THG of Yb:fiber comb at 1060 nm

Using the 11 Watts Yb:fiber frequency comb, we generate high power ultraviolet light at 353 nm by sum frequency generation of 1060 nm light and the second harmonic at 530 nm. A schematic of the setup is included in Figure 5.1. The Er:fiber frequency comb is dispersive wave shifted to 1060 nm in a highly nonlinear fiber assembly. The light is amplified in the photonic crystal fiber amplifier described in Chapter 2 to 11 Watts. The fundamental gaussian beam diameter 2w is 4.2 mm, which is measured with a knife edge on a linear manual stage. The result is consistent with another measurement using a CCD camera.

The beam is focused into a 2 mm thick LBO cut for type I phase matching for second harmonic generation of 1064 nm. The LBO crystal has antireflection coating for 1064 nm and 532 nm on both sides. The fundamental and second harmonic are collimated by a concave silver mirror then sent through a Calcite time delay compensator (TDC12301-AR, Newlight Photonics Inc.) and a dual waveplate (WPD03-H1030-F515-SP, Newlight Photonics Inc.). The time delay between the fundamental and the second harmonic comes from the group velocity mismatch of the two pulses in the LBO. In type I phase matching, i.e. ooe phase matching, we calculate the group velocity mismatch between 1064 nm and 532 nm to be 43 fs/mm in LBO using the optical constants in [122]. The second harmonic's polarization is orthogonal to the fundamental's. The dual waveplate rotates the polarization of the fundamental pulse to match the second harmonic. Then the sum frequency generation is done within a 0.3 mm thick BBO cut for type I third harmonic generation of 1056 nm (BTC5030-THG1056(I)-AR, Newlight Photonics, Inc.).

The focal length of both concave silver mirrors M1 and M2 and the two lenses L1 and L2 are all 10 cm. Both LBO and BBO are mounted in rotational mounts on manual stages for alignment. The L2 is mounted on a 3-axis stage for collimating the output beams.

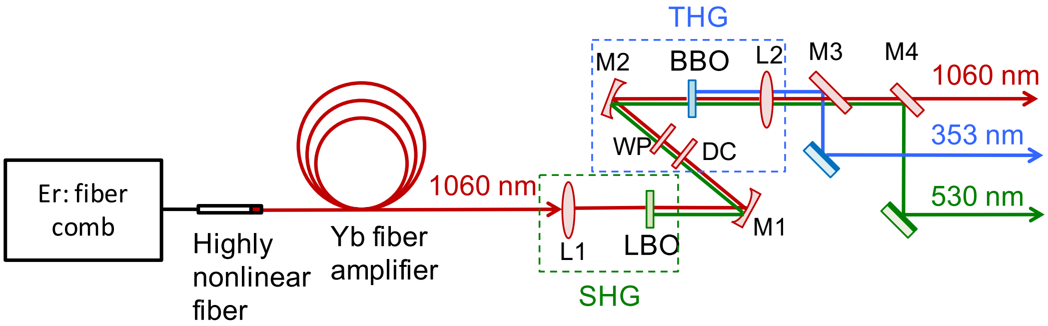

Figure 5.1: The optical layout of second harmonic generation and third harmonic generation with Yb:fiber laser. L1, L2: lenses, f = 10 cm; DC: delay compensator; WP: dual waveplate; M1, M2: concave silver mirror, f = 10 cm; M3, M4: harmonic separation dichroic mirror

Two different beamsplitters are used to separate the different harmonics. Figure 5.2 contains the harmonic generation efficiency curve at different fundamental powers. The pump power is tuned by running the pump diode for Yb:fiber amplifier with different currents. Without the sum frequency generation BBO crystal in the setup, the SHG conversion efficiency is as high as 36%, which yields 4.22 W of 530 nm light when pumped by 11.5 W of 1060 nm. When the phase matching of both second harmonic and third harmonic generation are optimized, the overall SHG and THG conversion efficiency is 25% and 6%, respectively.

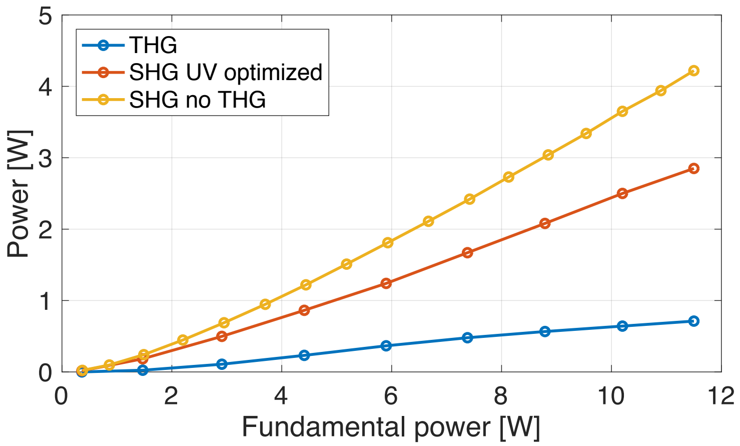

Figure 5.2: The conversion efficiency of SHG and THG of 1060 nm light. The blue curve represents the third harmonic generation efficiency. The red and yellow curves are the second harmonic generation efficiency with the UV power optimized and without the third harmonic generation setup, respectively.

5.3 UV cavity

5.3.1 UV cavity mirror coating

The UV frequency comb is coupled into a 3 meters long bow-tie cavity for power enhancement as depicted in Figure 5.3.

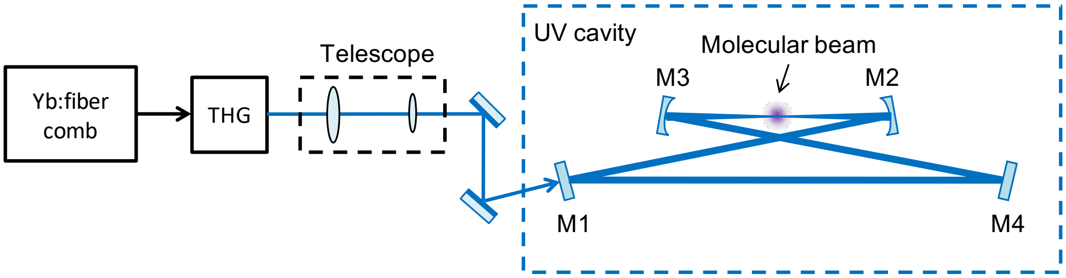

Figure 5.3: The optical layout of coupling the UV comb to the pump cavity. M1 is an input coupler with 97% reflectivity at 350 nm. M2, M3, M4 are all mirrors with reflectivity higher than 99.8%. M2 and M3 have a radius of curvature of 75 cm.

The cavity consists of an input coupler with 97% reflectivity at 350 nm and three mirrors with a minimum reflectivity of 99.8% at 350 nm. The mirror coatings are designed with an incident angle of 0°. The finesse of the UV cavity is calculated using equation 1.8 to be $\sim$172.

For this cavity, we set the distance between the curved mirrors M2 and M3 to be 79.8 cm. The total cavity length is 3 m to match the 100 MHz repetition rate. The maximum incident angle on all cavity mirrors is 4.5° and the minimum incident angle is 2.4°. Using the ABCD matrix method, we calculated the beam radius at focus is 80 μm both horizontally and vertically. The UV cavity buildup is measured to be 21, which is lower than the estimation using the pump cavity mirrors' reflectivity. This could be due to the astigmatism of the UV beam and the mode-matching of UV beam to the pump cavity. Further investigation is needed for higher buildup, but the intracavity UV power is sufficient for the experiments. The buildup measurement is taken with the method described in [26]. The locking and modulation of this cavity is done in the way as described in Chapter 3.

5.3.2 UV cavity contamination and solution

One issue with simultaneously running a molecular beam of small organic molecules and an optical cavity containing high power UV light in the same vacuum chamber is contamination of the cavity mirrors. It takes only seconds to occur. When the cavity mirror is contaminated by the sample molecules, the cavity beam mode jumps to higher order modes, the intracavity power drops and the comb cavity lock becomes too unstable to keep the UV cavity on resonance.

To solve this problem, we designed a different molecular beam jet and modified the vacuum pumping strategy. There are several concerns for designing the molecular beam jet. One, the setup should allow alignment of the slit nozzle in XYZ axis, rotation and tip/tilt to match the probe beam path. Second, the beam height is 2.5 inches above the breadboard, so the setup has to be compact so that the distance between the nozzle and the beam could be adjustable from zero to 15 mm for experiments on clusters. Third, the assembly should isolate the molecular beam from the cavity mirrors. Fourth, for some experiments, the molecule of interest is heated to up to 150° C for a higher vapor pressure, which means the assembly should be heated as well. A schematic is shown in Figure 5.5. The mechanical drawings of these parts are included in the Appendix.

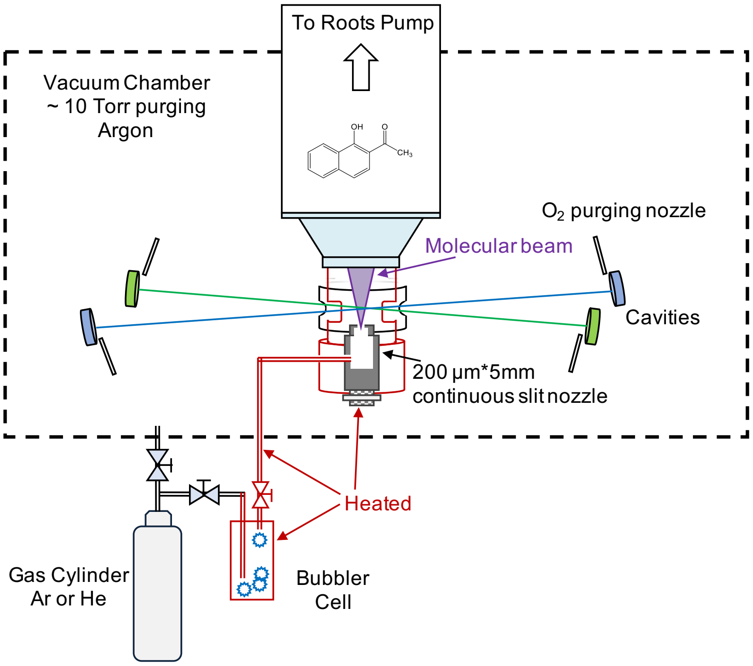

Figure 5.4: The schematic of the molecular beam jet setup. The holder of the nozzle isolates the molecular beam from the vacuum chamber. With the "sealed" operation of the supersonic expansion, the inert purge gas, and the mirror purging O_2, we are able to run the supersonic expansion of organic molecules and the high power UV cavity in the same vacuum chamber.

Photos of the molecular beam jet parts and the assembly are included here.

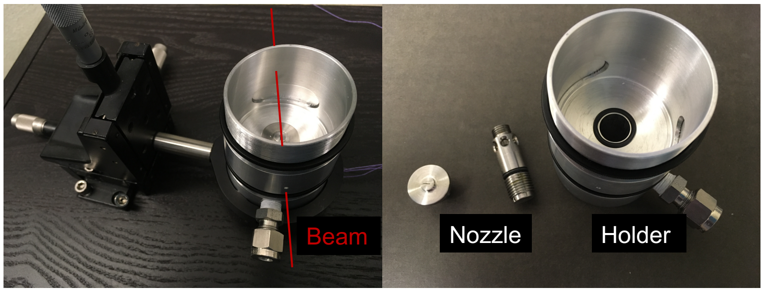

Figure 5.5: Photos of the molecular beam jet. See the main text for details.

The 200 μm wide and 5 mm long continuous slit nozzle is held in an aluminum holder. The 2 inches diameter holder is used to position the slit nozzle relative to the pump and probe beams, heat the nozzle, and isolate the molecular beam from the vacuum chamber. A wide ring-shaped piece mounted on the holder, which is indicated in black in the figure, have two of 2 mm diameter holes for the beams' passage. The assembly seals well enough such that with 20 Torr of Argon purging the chamber, the pressure in the holder is below 50 mTorr. In addition, we purge all cavity mirrors with oxygen to maintain the stable operation of the UV cavity in the presence of organic molecules. Eight pieces of stainless steel tubings with an inner diameter of 1/8 inches are set up as the O_2 purging nozzles pointing at the highly reflective surfaces of all cavity mirrors. The chamber pressure measured with a manometer pressure gauge increases by 1-2 Torrs with O_2 compared to without O_2. The O_2 dosing puts additional constrains on the cavity mirrors. For this setup, all mirrors have a SiO_2 top layer to resist further oxidation. To guide the supersonic expansion to the vacuum pumps, a 3D printed acrylonitrile butadiene styrene (ABS) cone is pushed on to the jet holder. A short piece of polyethlene hose is clamped to the cone on one end and attached to the lid of the chamber on the other end. The molecules escape from the nozzle are isolated from the chamber and guided to the exhaust line.

The sample pick-up cell, the molecules delivery lines, the supersonic jet holder and the nozzle are all heated. The pick-up cell and the stainless steel tubings are heated by wrapping heat tapes around them. For the tubing in the chamber, we use heater wires covered by heat conducting ceramic beads. 2-4 pieces of 15 Watts 1/8 diameter cartridge heaters are glued in the jet holder for heating. All temperatures are measured with thermo-couples and controlled with PID temperature controllers. The nozzle temperature is set 20°C higher than the cell. From cell to nozzle, the sample delivery line is heated with increasing temperatures to avoid sample condensation.

5.3.3 f_o tuning with gas pressure

This new molecular beam setup not only eliminates the contamination problem, but also provides a way to tune the f_o difference between the pump and probe cavities. The f_o tuning curve is in Figure 5.6. The measurement is taken in the following way. In the vacuum chamber, the pump and probe cavity lengths are set to match the frequency comb's repetition rate of 91 MHz. The UV light from the third harmonic generation is coupled to the pump cavity and the green light from the second harmonic generation is coupled to the probe cavity, which was used in the I_2 experiment as described in earlier chapters. Both pump and probe cavities are locked to the frequency comb laser. At each Argon pressure, the oscillator's f_o is tuned to optimize the pump cavity intracavity power. The ratio of probe intracavity power compared to highest probe intracavity power is recorded.

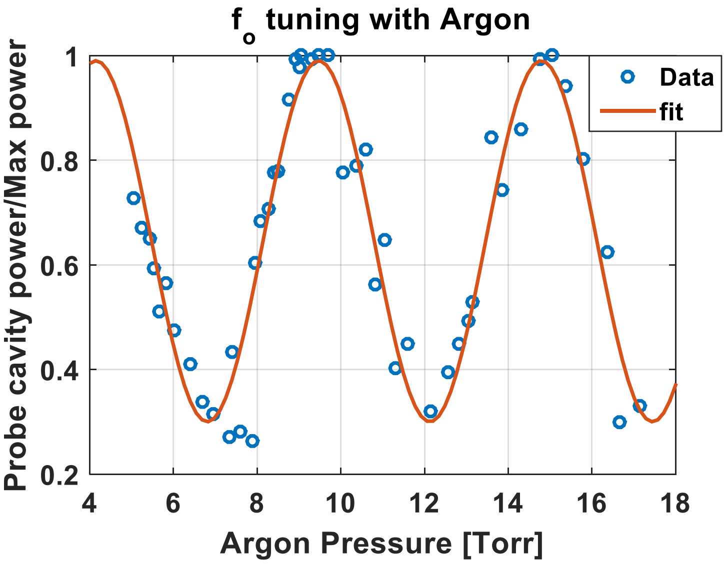

Figure 5.6: Tuning of f_o with Argon pressure. The data is fitted with a sine wave using least square fitting.

Using the Sellmeier equation coefficients of Argon reported in [123], the index of refraction of 1 atmosphere of Argon at 15°C can be described as eqn. 5.1. Here n is the index of refractive and λ is wavelength in unit of μm.

$$(n-1)\cdot 10^7 = 643.2135 + \frac{286060.21}{144 - \frac{1}{\lambda^2}} \tag{5.1}$$

The carrier-envelope phase shift induced by Argon is expressed in eqn. 5.2. $\Delta\phi_{CE}$ is the carrier envelop phase shift, ω is the angular frequency, and L is the length of the beam path in the gas.

$$\Delta\phi_{CE} = \omega_0^2 \frac{dn}{d\omega}\frac{L}{c} \tag{5.2}$$

In our case, L is the cavity length minus the 2 inches molecular beam holder diameter, where the Argon pressure is less than 100 mTorr. 1 Torr of Argon is calculated to give a 0.62π phase shift at 350 nm and 0.17π phase shift at 530 nm. Therefore, 4.4 Torr of Argon gives 2π phase shift between these two wavelengths. The fitting of measurement gives 5.3 Torr of Argon for a phase shift of 2π. With 10 Torr of Argon, we calculate the group delay dispersion to be 6.7×10^{-4} fs^2/cm at 350 nm. The total GDD with 10 Torr of Argon in the cavity is 2.2 fs^2. The pulse broadening is negligible for 100 fs pulses in the cavity.

5.4 Enhancement cavity for the tunable visible frequency comb

5.4.1 Visible cavity mirror coating

In the widely tunable spectroscopy, we use a tunable visible frequency comb as the probe. Since the pump-probe signal enhancement scales with product of the pump and probe cavity finesse, we designed the probe cavity to achieve a finesse of $\sim$ 1000 at 450 - 700 nm. At one particular wavelength, off-shelf quarter-wave stacks mirrors could satisfy both high reflectivity and low group delay dispersion. However, broadband high reflectors tend to have high dispersion that's not appropriate for cavities to coherently enhance femtosecond pulses. Mirrors with high reflectivity, low dispersion in such a broad spectral range are not standard. Therefore, we designed custom cavity mirror coatings so that the enhancement of tunable visible femtosecond pulses is achievable with one set of mirrors. Figure 5.7 shows the optical layout of the visible cavity and the coating curves of the partial reflector and high reflector. The high reflector and partial reflector have opposite chirps.

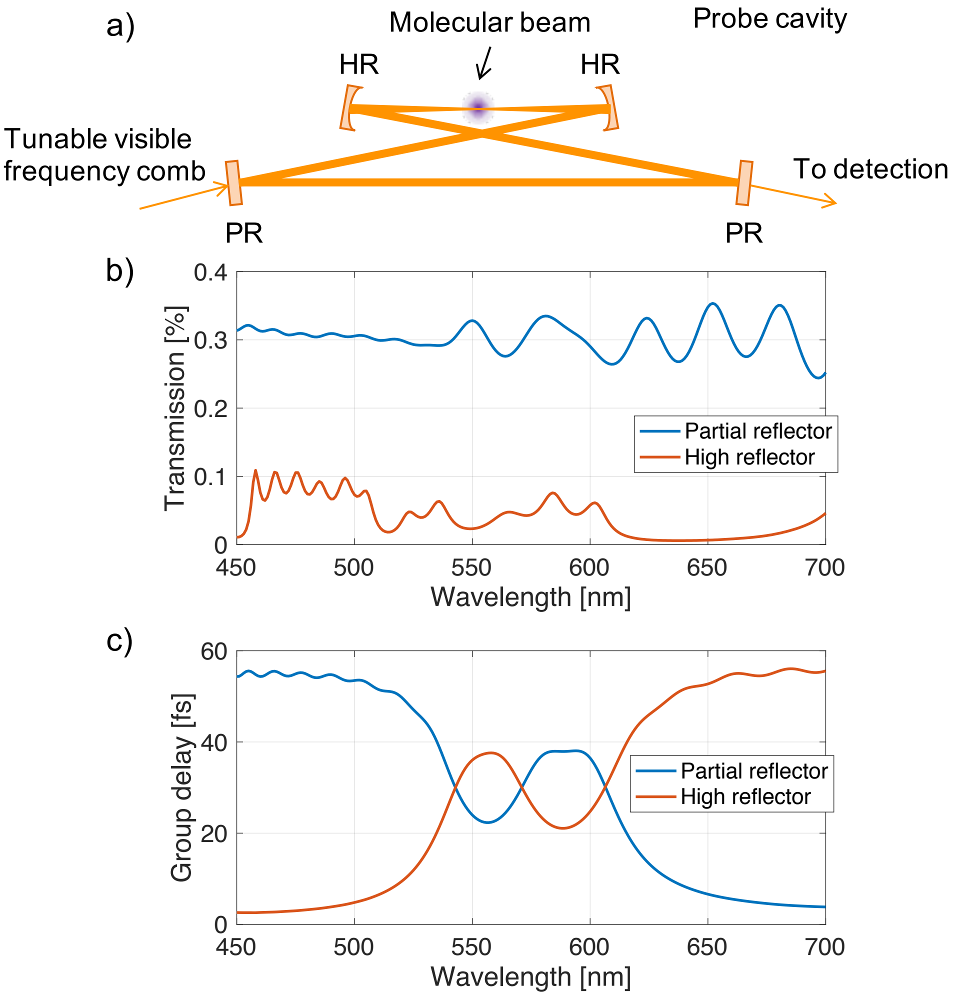

Figure 5.7: a). The optical layout of the tunable visible frequency comb enhancement cavity. The input coupler M1 and the output coupler M4 have 99.7% reflectivity at 450 - 700 nm. M2 and M3 are high reflectors with reflectivity higher than 99.9%. M2 and M3 have a radius of curvature of 50 cm. b). The mirror coating transmission curves calculated by the coating company. c). The calculated group delay in both high reflectors and partial reflectors provided by the coating company.

The lower plot in Figure 5.8 shows the group delay dispersion of the partial reflector and the high reflector are low and they have opposite signs so the absolute total round-trip GDD is less than 100 fs^2. The intracavity pulse durations are calculated with the GDD data and assuming 100 fs pulse duration input pulses. This set of mirrors supports pulses less than 200 fs over the whole range at 450 - 700 nm. In the upper figure, the cavity finesse is calculated with the mirror transmission data in Figure 5.7(b).

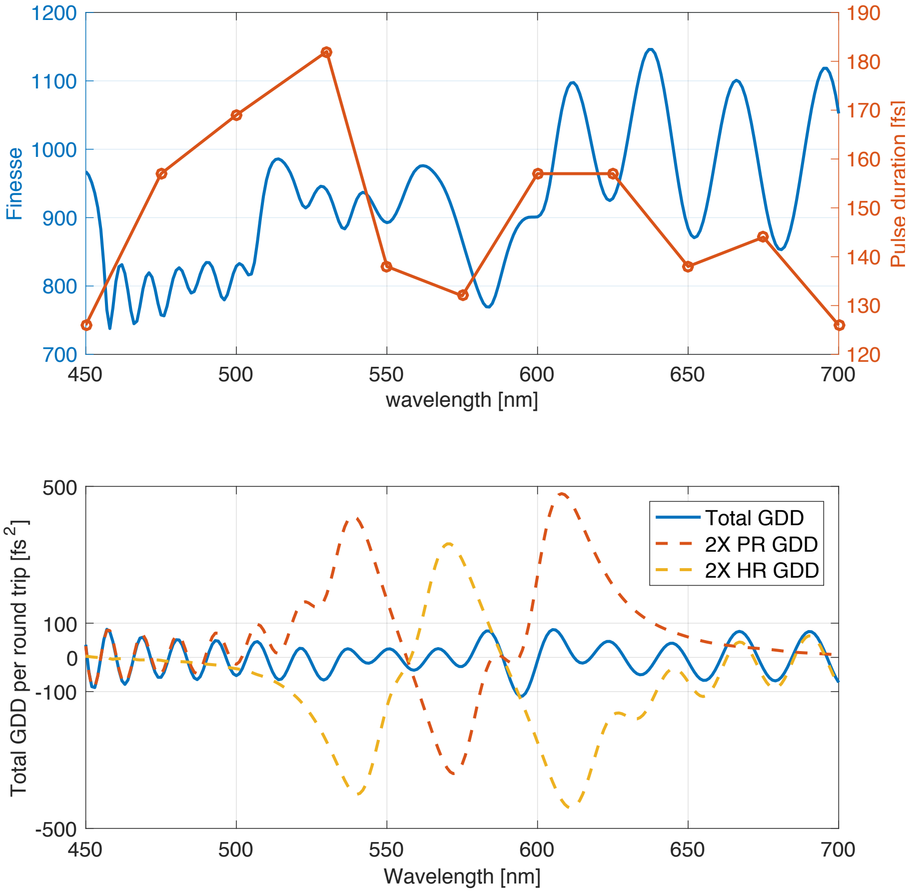

Figure 5.8: The visible cavity mirrors are pairs of chirped mirrors. The upper plot shows the cavity finesse is between 750 and 1150 at all different wavelength. The lower plot shows the GDD of the mirror coatings and the total round trip GDD is smaller than 100 fs^2 at 450 - 700 nm. With such well controlled GDD, the intracavity pulse duration is below 200 fs across the whole visible spectral range when seeded with 100 fs pulses.

5.4.2 Tunable visible frequency comb coupled to enhancement cavity

The visible enhancement cavity is aligned with the second harmonic of the Yb:fiber laser. The distance between the two concave mirror M2 and M3 is set to 51.8 cm and the total cavity length is 3 meters. The maximum incident angle on the cavity mirrors is 3°. The beam radius at the cavity focus is calculated to be 56 μm for 450 nm and 70 μm for 700 nm. Using the tunable visible frequency comb generated from a femtosecond optical parametric oscillator, which is discussed in detail in the next chapter, we locked the laser to the cavity. A schematic of locking the tunable visible frequency comb to the cavity is shown in Figure 6.12. A few intracavity spectra are recorded and exhibited in Figure 5.9. The full-width-half-maximum of the two spectra at 567.5 nm and 587.5 nm are 4.9 nm and 3.5 nm, respectively. Fourier transform limited pulse durations are calculated to be 97 fs and 146 fs.

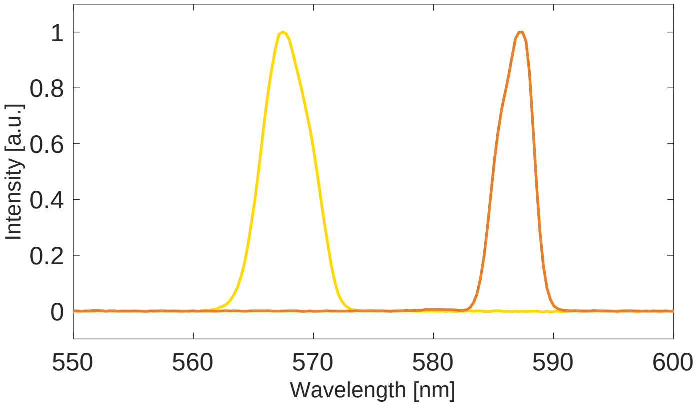

Figure 5.9: The figure shows the two intracavity spectra at different visible wavelength. The tunable visible frequency comb is generated in a optical parametric oscillator. The bandwidth of both spectra are able to support pulses less than 150 fs.

Chapter 6

Tunable visible frequency comb generation and stabilization

6.1 Introduction

By coupling frequency combs into optical resonators, we have demonstrated a new ultrafast spectroscopy method to study ultrafast chemical dynamics in molecular beams. This method is taking advantage of the fact that frequency combs consist of evenly spaced comb "teeth" in the frequency domain while simultaneously frequency combs are femtosecond pulses in the time domain. To unravel more complex photo-induced molecular dynamics with cavity-enhanced ultrafast spectroscopy, we are extending the operating range of this method to be widely tunable since the samples of interest tend to have broad absorption features.

Widely tunable femtosecond pulses, especially at a high repetition rate, are also needed for various biophotonics applications, particularly imaging experiments, such as Coherent anti-Stokes Raman Scattering imaging [124] and multiphoton microscopy [125]. In two-photon microscopy, widely tunable pulses allow the excitation of different specimen and stronger fluorescence signals benefit from the femtosecond pulse durations due to the high peak intensity.

Using Ti:Sapphire lasers as the pump lasers, tunable femtosecond lasers in near-infrared and visible spectral range are commercially available. However, with pump lasers at 1 μm, such as Yb:fiber lasers, which are more compact, cost-saving and low-maintenance, frequency conversion to tunable visible is less developed. One earlier work [126] showed dispersive wave generation with 170 fs pulses at 1020 nm in a series of photonic crystal fibers with the dispersion profile well engineered. This method produced less than 10 mW of 347 - 680 nm pulses. But to cover the whole tuning range, the authors needed to replace the photonic crystal fibers with different core sizes for each wavelength. Another demonstrated setup for tunable visible pulses is reported in [127]. The authors pumped a highly nonlinear fiber with 60 fs pulses at 1.55 μm at 108 MHz. By varying the amount of chirp in the pump pulses in the nonlinear fiber, the dispersion wave generation is tuned between 1.05 and 1.40 μm. The dispersive wave is frequency doubled in three fan-out MgO:LiNbO$_3$ crystals with different polling periods. This setup generated less than 10 mW of 520 - 700 nm pulses with 600 fs to 1 ps pulse durations.

For tunable near-infrared, optical parametric oscillators pumped by the second harmonic of Yb lasers exhibit excellent tunability [128, 129]. The OPO reported in ref. [130] outputs hundreds of mW in 688 - 1050 nm and 1150 - 1900 nm using a 1 mm thick BiBO as the nonlinear crystal. Vengeli et al.[131] compared two OPOs based on BBO and LBO crystals pumped by second harmonic of Yb:KGW laser. The two OPOs have rather similar performance in terms of tuning range and parametric conversion efficiency. In both articles, the output pulses were compressed in a pair of grating compressor to reach about 100 fs pulse durations. None of these previous light sources is phase-stabilized for frequency comb applications, but stabilization of OPOs for comb applications has been achieved in other contexts [132, 133].

6.2 Tunable visible comb generation via spectral broadening in all-normal dispersion photonic crystal fiber

The pulse energy of our Yb:fiber frequency comb laser is 110 nJ per pulse with the average power of 11 Watts and the repetition rate of 100 MHz. We have explored several ways to generate widely tunable frequency combs with this low pulse energy. Mainly we employ fibers or cavities to increase the interaction length of pulses in the medium to realize nonlinear optics. The all-normal photonic crystal fiber based setup is described in this section. The work of using a cavity, which is an optical parametric oscillator in this case, is included in later sections.

6.2.1 Layout of supercontinuum generation of Yb:fiber laser

The optical layout is shown in Figure 6.1. The Yb:fiber oscillator and amplifier are described in Chapter 2. Less than 1 W of light is sent to a 18 cm long photonic crystal fiber (NL-1050-NEG-PM-1, NKT Photonics). A half waveplate and a polarizer are used to rotate the polarization of 1060 nm light in a half waveplate to align with the slow axis of the fiber. Both ends of the fiber are mounted on a precision manual stage. The PCF has a mode field diameter of 2.2 μm and a numerical aperture of 0.37 at 1064 nm, so an aspherical lens is used to focus the beam into the fiber. The highest coupling efficiency observed with this setup is 29%. This could be due to the poor surface flatness caused by the hand cleaving process of this fiber.

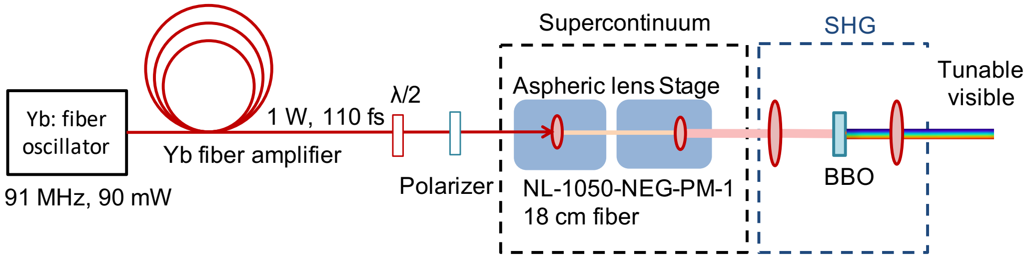

Figure 6.1: The optical layout of supercontinuum generation of Yb:fiber laser in a photonic crystal fiber. $\lambda/2$: half waveplate.

Spectrally broadening of near-IR pulses has been demonstrated in various types of fibers [126, 134, 135, 136]. The advantage of this supercontinuum generation fiber is that the dispersion is normal for all the wavelength between 600 nm to 1400 nm. The spectrum of the input pulses is broadened via self-phase modulation. In more common hybrid anomalous-normal dispersion fibers, the soliton dynamics arise from the anomalous dispersion corrupt the temporal profile by producing many pulses. In this all-normal dispersion fiber, the output pulses can still consist of a single pulse, which is crucial for applying pulses to ultrafast spectroscopy.

6.2.2 Frequency doubling of supercontinuum spectrum in near-IR

The input and output spectrum from the supercontinuum generation PCF are included in Figure 6.2. The whole spectrum contains 495 mW power with 1.97 W input. Higher input power does not broaden the spectrum further or increase the output power. This spectrum is very similar to the observation reported in [137].

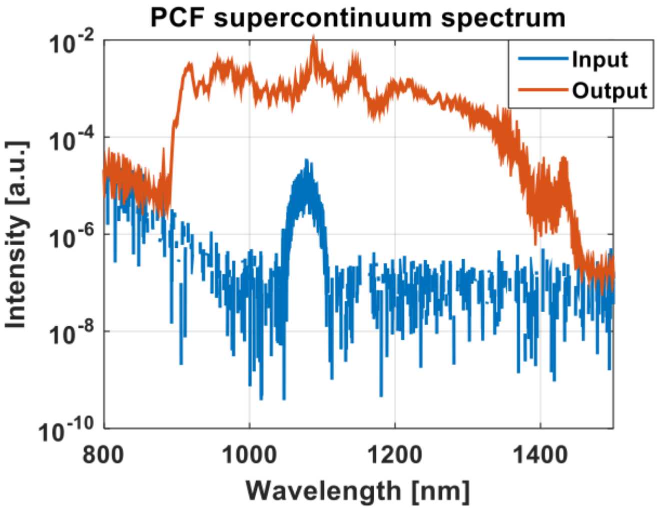

Figure 6.2: Supercontinuum generation spectrum of Yb:fiber laser in a photonic crystal fiber.

The supercontinuum spectrum is frequency doubled in a 0.5 mm thick BBO cut for type I phase-matching for second harmonic generation of 1064 nm. Both sides of the BBO are coated with antireflection coating for 1064 nm and 532 nm. The tunable visible spectra are included in Figure 6.3. The spectrum is tunable between 460 and 640 nm. All these tunable visible spectra contain about 0.5 mW power. The average power of the second harmonic of the supercontinuum could be improved by using a different nonlinear crystal. One or two pieces of periodically-polled MgO:$\mathrm{LiN_3O_5}$ could cover the phase-matching conditions for the near-IR spectrum. However, the group delay dispersion in MgO:PPLN is much higher than BBO, so the frequency doubled light spectrum bandwidth and pulse duration could be a concern for the ultrafast experiments.

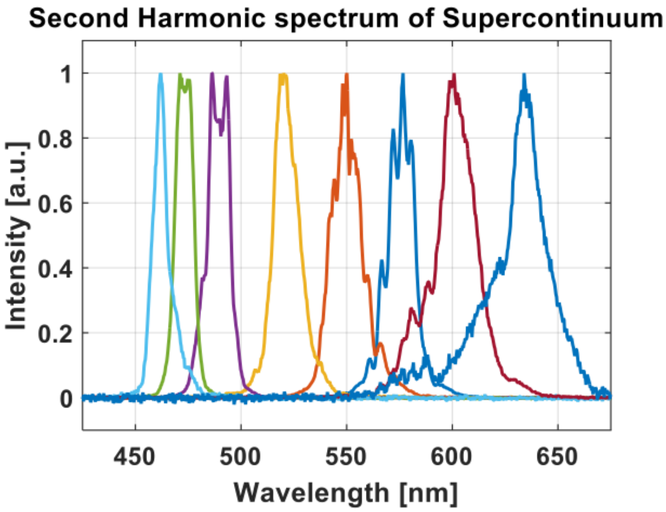

Figure 6.3: Tunable visible pulses generation by frequency doubling the supercontinuum spectrum.

To examine the suitability of the tunable visible light for cavity-enhanced ultrafast spectroscopy, we measured the relative intensity noise of the tunable pulses under several different BBO phase matching angles. A typical noise spectrum up to 6 kHz is presented in Figure 6.4. The relative intensity noise in the visible light is very similar to RIN of the 1060 nm frequency comb laser as shown in Figure 2.16. The supercontinuum generation based on self phase modulation does not add noise significantly.

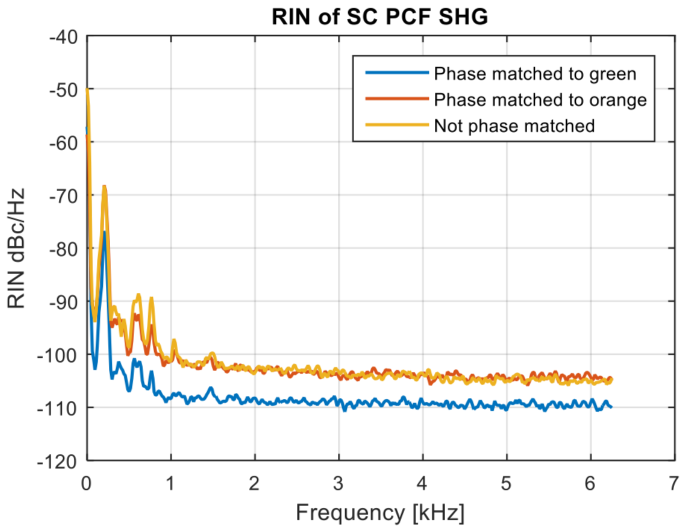

Figure 6.4: Relative intensity noise of tunable visible pulses generated with the supercontinuum spectrum.

The performance of this supercontinuum fiber setup in terms of spectrum tunability and intensity noise meets the requirement for cavity-enhanced ultrafast spectroscopy experiments. However, the tunable visible powers are low for the experiment. The optical power required by the autobalance detector for efficient common mode noise subtraction performance is about 1 mW. Considering the 1:2 power splitting ratio of probe/reference recommended for optimal performance of the autobalance detector, the loss from the grating in the PDH error signal generation setup, tunable visible pulses with higher powers are desired. The more critical reason that we did not perform the UV/vis cavity-enhanced ultrafast spectroscopy experiments with the fiber setup is that we observed decays of this fiber over a time period of a few hours and the decay were not reversible.

6.3 Green pumped femtosecond optical parametric oscillator

We present a femtosecond optical parametric oscillator that generates tunable near-infrared and visible frequency comb at 420 - 1470 nm with 10 to 265 mW in the visible. The OPO is synchronously pumped by the second harmonic of a 11 Watts Yb:fiber frequency comb laser operating at 1060 nm with 100 MHz repetition rate. A noncritical phase matching LBO crystal is used as the nonlinear crystal for parametric oscillation. The resonant signal is tunable between 835 - 970 nm by changing the LBO crystal temperature and the idler covers 1175 - 1470 nm. Using one piece of thin BBO crystal for intracavity doubling both signal and idler, we achieve tunable visible pulses by simply adjusting the phase-matching angle of the BBO and the OPO cavity length.

6.3.1 Nonlinear crystals selection

A few nonlinear crystals are considered for the optical parametric process including Lithium triborate (LBO), Beta barium borate (BBO), BiB_3O_6 (BiBO), MgO doped periodically-poled Lithium niobate(MgO:PPLN) and Periodically Poled Stoichiometric Lithium tantalite (PPSLT). The selection of nonlinear crystal is based on the single-pass parametric gain, the phase-matching tuning method and range, the material dispersion and the damage threshold. Figure 6.5 included a comparison of these above mentioned crystals.

Crystal	BBO	LBO	BIBO	MgO:PPLN	PPSLT
Category	Negative Uniaxial	Biaxial	Biaxial	Negative Uniaxial	
Phase-matching	Type I e→oo	Type I e→oo	Type I o→ee	Type 0 o→oo	Type 0 o→oo
Cut angle	22.7	theta,phi = 90, 0	theta,phi = 40.5 0	Poling period 6.8-7 μm	Poling period 7.5-8.0 μm
Group velocity mismatch [fs/mm] 530 nm pump signal 900	70	37	190	846-866 (25-200°C) 700 (HC)	627 (200°C) 600(HC)
Interaction length [mm]	1.57	3.0	0.58	0.13	0.18
Nonlinearity coefficients [pm/V]	d_{22} = 2.3, d_{31} = -0.16	d_{31} = -0.95, d_{32} = 1.02, d_{33} = 0.057	d_{12} = 3.2, d_{13} = -1.76, d_{14} = 1.66		
d_{eff} [pm/V]	$d_{31}\sin(\Theta)-d_{22}\cos(\Theta)\sin(2\phi)$ 2.02 (SNLO)	0.85(SNLO)	$-d_{12}\cos(\Theta)2-d_{13}\sin(\Theta)2+d_{14}\sin(2\Theta)$ -2.28(SNLO)	14 (typical) G&H, Covesion	7(HC)
Γ [1/mm] 2w = 50 um	1.50	0.66	1.47	6.61	3.54
Parametric gain	27.8	13.1	1.37	1.37	0.86
Damage threshold [GW/cm^2]	9.9 at 1053 nm	2.2 (10 ns); 45 (100 ps) at 532 nm		4	Higher than PPLN
Tuning for phase-matching	Angle tuning	Temperature tuning	Angle tuning YZ plane	Temperature and polling period	Temperature and polling period

Figure 6.5: A comparison of LBO, BBO, BiBO, MgO:PPLN and PPSLT as the OPO crystals. The group velocity mismatch is calculated with the group velocities at 530 nm (pump) and 900 nm. The interaction length is calculated using ratio of pump pulse duration (110fs) and the group velocity mismatch. Γ and parametric gain are calculated using eqn. 6.1 and eqn. 6.2.

Since the pump pulse duration is about 100 fs, the group velocity walk-off limits how long the pump pulse and the generated pulse can overlap in the crystal. The parametric gain G is calculated using the following equations [138].

$$\Gamma^2 = \frac{8\pi^2 d_{eff}^2 I_p}{n_p n_s n_i \lambda_s \lambda_i \epsilon_0 c}(\Gamma L \gg 1) \tag{6.1}$$

Here d_{eff} is the nonlinear coefficient, I_p is the pump intensity, L is the crystal length.

$$G = \frac{1}{4} e^{2L\sqrt{\Gamma^2-(\Delta k/2)^2}} \tag{6.2}$$

The calculated single pass parametric gain of different crystals are included in Figure 6.6.

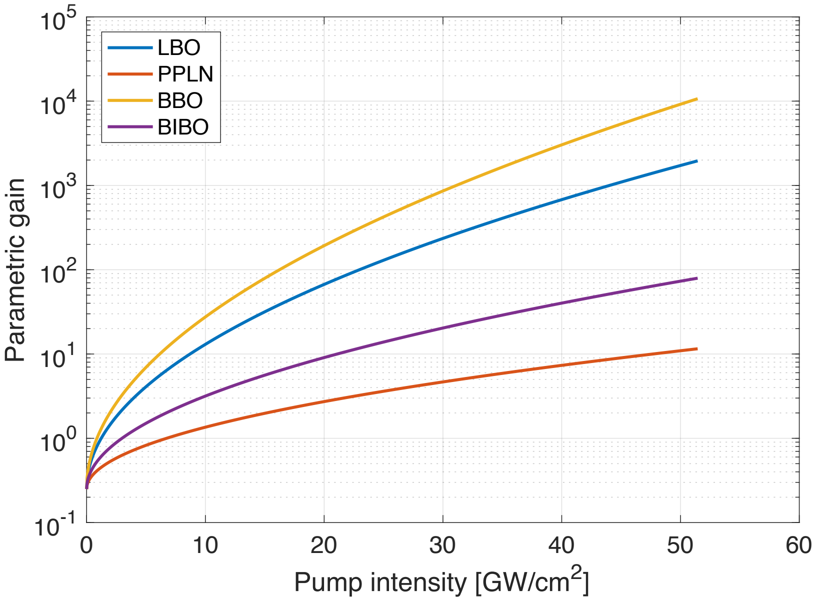

Figure 6.6: The comparison of calculated parametric gain of four different crystals including a 3 mm long LBO, a 2 mm long BBO, a 1 mm long BiBO and a 0.5 mm long MgO:PPLN. The pump intensity is calculated using 0-4 W average power, 110 fs pulse duration and a focused beam size of 2w = 50 μm.

The 3 mm long LBO is selected as the OPO crystal with several reasons. One is that the single-pass parametric gain is higher than BBO and BiBO. Second is that the tuning of phase-matching is by tuning the crystal temperature, where the crystal misalignment is minimal compared to the phase-matching angle tuning way. In addition, LBO's group velocity dispersion is low, so the generated pulse can still have enough bandwidth to support short pulses for the ultrafast spectroscopy experiments.

6.3.2 Optical layout of OPO

The optical layout of OPO is shown in Figure 6.7. The second harmonic of the frequency comb shown in Figure 5.1 is taken to pump the OPO.

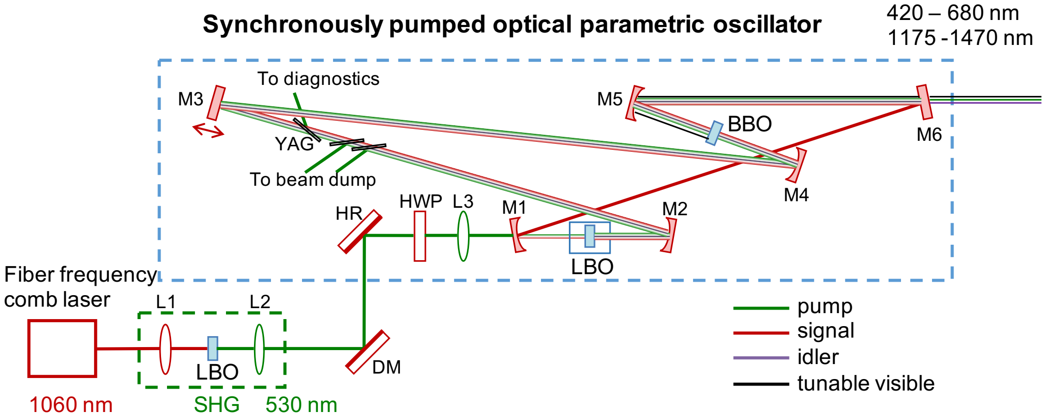

Figure 6.7: The schematic of the synchronously pumped optical parametric oscillator. A frequency comb laser centered at 1060 nm is frequency doubled in a LBO crystal to 530 nm. This pumps a synchronously pumped optical parametric oscillator. The tunable visible light is generated by frequency doubling both the signal and idler. L1, L2: focal length = 10 cm; DM: dichroic mirror; HR: high reflector; HWP: half waveplate; L3: convex lens, focal length = 15 cm; M: mirror.

The OPO crystal is a 3 mm long LBO cut for type I noncritical phase-matching OPO pumped by 532 nm. A phase-matching tuning curve of LBO pumped with 534 nm light is included in Figure 6.8.

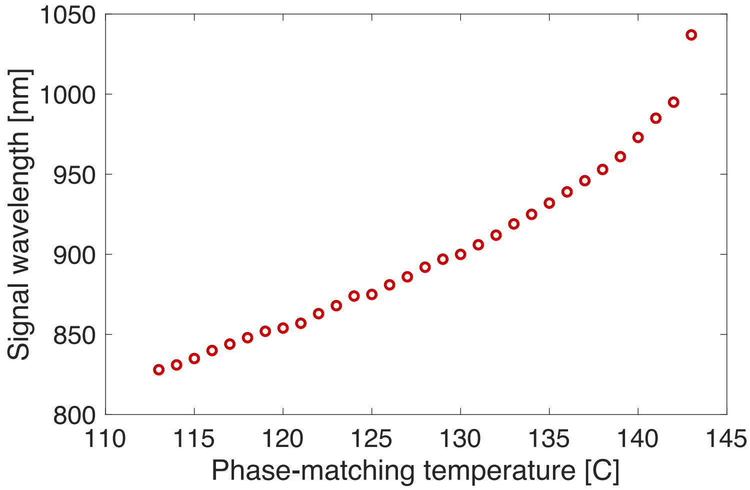

Figure 6.8: The calculated phase-matching signal wavelength vs. the LBO crystal temperature when pumped by 534 nm light using SNLO.

The crystal has an angle of θ=90° and ϕ=0°.[122] Both sides have antireflection coatings at 532 nm and 850 - 1064 nm for the pump and signal respectively. The crystal is housed in a home-built oven for controlling the crystal temperature between 25°C and 200°C. The compact oven design minimizes the incident angle on the cavity mirrors for minimum astigmatism. The oven is mounted on a tip, tilt and rotation stage for alignment of the LBO. With the pump wavelength at 530 nm, the phase-matching temperature is measured to be 127°C to 144°C to phase match to 834 nm to 969 nm in the signal and 1452 nm to 1169 nm in the idler.

The intracavity second harmonic generation of signal and idler are achieved by tuning the phase-matching angle of the BBO crystal. We select BBO for the broad phase-matching tunability and moderately high nonlinear coefficient. Using SNLO [139], we calculate the phase-matching angle for type I SHG of 850 nm is θ of 27.6° and SHG of 1400 nm is 20.0°. The 2 mm long BBO crystal has a cut angle of θ=23.2° and ϕ=90° for type I SHG of 1040 nm and is AR coated for 1040 and 520 nm. The tuning of phase-matching can be achieved via rotating the BBO phase-matching angle θ and OPO cavity length. A tuning curve of type I SHG phase-matching angle in BBO is included in Figure 6.9.

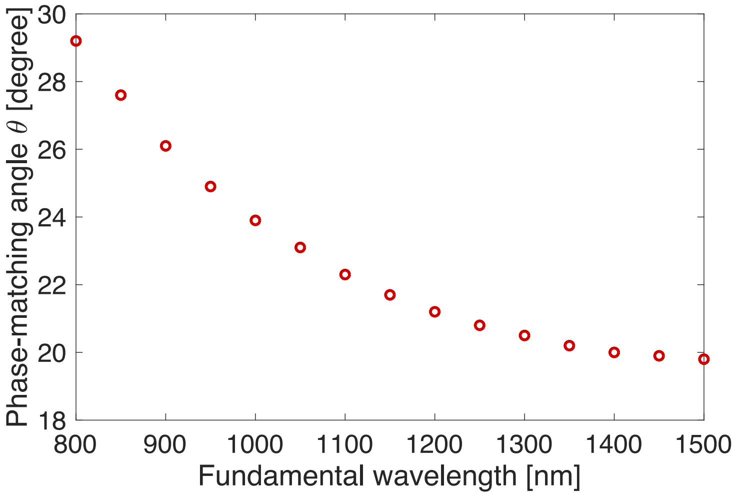

Figure 6.9: The calculated type I SHG phase-matching angle of BBO using SNLO.

6.3.3 OPO cavity mirror coatings

To obtain stable operation, the OPO is only resonant with the signal. However, we need both the signal and idler for intracavity doubling to cover the whole visible spectral range. At the same time, we need the net round-trip group delay dispersion to be small so the OPO supports ultrashort pulses. So even though the OPO cavity finesse is low, to meet all constrains over such a broad range we need to customize the cavity mirror coatings. We design the mirror coatings as following. M1, M6 has $> 99.9\%$ reflectivity at 850 - 1064 nm and $< 5\%$ reflectivity for 450 - 700 nm and the group delay dispersion (GDD) is smaller than 100 fs^2 for 850 - 1064 nm. This allows efficient transmission of the visible pulses at the output coupler M6 and passage of green pump laser at input coupler mirror M1. All of M2, M3, M4 and M5 are protected silver mirrors with a reflectivity higher than 98% at 850 - 1400 nm and GDD less than 2 fs^2. A representative coating is coating 113833 from Layertec, GmbH. The round trip loss of the signal power caused by the optics is calculated to be 16% at 850 nm giving a cavity photon lifetime of 57 ns. The coating of input coupler M1 and output coupler M6 allows transmission of idler so the cavity is only resonant with the signal.

6.3.4 OPO cavity mirror layout

The total OPO cavity optical length is 3 meters, which matches the pump laser's repetition rate of 100 MHz for synchronous pumping. M1, M2, M4 and M5 are curved mirrors with a radius of curvature of 20 cm. The separation between M1 and M2 is 21.0 cm and between M4 and M5 is 20.6 cm. Using the cavity's ABCD matrix, we calculate the beam radius at the two focal planes are 30 μm and 70 μm respectively. Since the stability of the cavity strongly depends on the curved mirror separations, M2 and M5 are mounted on translation stages for ease of fine adjustment. The 1/2 inch diameter planar mirror M3 is mounted on a copper bullet style PZT as described by Briles *et al.* [140] This stage is used to get the cavity length close to cavity resonant length and the PZT is for active stabilization of cavity length adjustment. Another piezo actuator (AE0203D08F, Thorlabs, Inc.), which has a lower resonance frequency but longer travel, is mounted in the same stage for fine tuning of cavity length. The incident angle on this mirror is set to be 1.5°, so that the cavity misalignment is negligible when changing the cavity length. This geometry not only collimates the residual pump, the frequency doubled signal, and doubled idler output beam, but also allows all these beams to propagate collinearly with roughly the same optical path length to the experiment, which minimizes any extra alignment effort when changing the output wavelength for the following experiment.

6.3.5 Intracavity Brewster's plates

Three pieces of 500 μm thick undoped YAG wafers are inserted in the OPO cavity and solved multiple issues for practical operation and diagnostics of the OPO. Firstly, the pump of the OPO is 4 Watts of 530 nm light, and this high power green light propagates collinearly with the signal, idler, and the tunable visible light. Without careful attenuation, the Watts of green causes trouble in the alignment process, complicates the spectrum separation setup and could induce thermal and optics damaging issues. So the first two pieces are aligned at Brewster's angle to reflect 29% of s-polarized pump at each surface using YAG's Sellmeier equation coefficients reported in [141] while introducing minimal loss for the signal and idler since they are generated in the p polarization. The residual light left after the Brewster's plates is 225 mW, which is comparable to the doubled signal. Secondly, As mentioned previously, the SPOPO is singly resonant with the signal and all cavity mirror are either high reflectors for signal or silver mirrors. Therefore, to access the intracavity signal without interrupting the cavity, the diagnostics are set up with the reflection from the third YAG wafer that's used in an angle 0.5° off from the Brewster's angle for a reflection of less than 0.01%. This reflection is sent to two switchable diagnostics that either records the intracavity signal and idler spectrum on an optical spectrum analyzer MS9740A, Anritsu, Inc. or measures the signal and idler power with two calibrated Ge detectors. Thirdly, adding Brewster's plates in the OPO cavity allows us to add dispersion for a more stable near degeneracy and to tune the cavity loss in a well-controlled manner by tuning the alignment of YAG wafers.

6.4 SPOPO results

6.4.1 Alignment procedure of the OPO

The LBO crystal is aligned by overlapping the reflection with the incident pump beam and minimizing the distortion on the polarization of pump beam. The OPO cavity is initially aligned with the green pump laser without the SHG BBO crystal in the cavity and the cavity length is set close to 3 meters to match the repetition rate of the pump. Once the first two roundtrips are overlapped, the parametric oscillation could be found by carefully tuning the position of M3 so the cavity is on resonance. The alignment is then optimized by maximizing the intracavity signal power and minimizing the oscillation threshold. The second harmonic generation BBO crystal is then inserted to the middle of M4 and M5. The resonance is found again by moving M3 to meet the synchronously pumping condition.

6.4.2 Near-infrared and visible light characterization

The spectrum and power of the signal and idler are shown in Figure 6.10. By varying the LBO temperature from 127°C to 144°C and adjusting the OPO cavity length, the signal is tuned between 835 nm to 970 nm and the corresponding idler is from 1469 nm to 1175 nm. Tuning towards shorter signal wavelengths is limited by the OPO cavity mirror coating range. Tuning towards longer signal wavelengths is limited by stability as the OPO approaches degeneracy. With the SHG BBO crystal tuned away from the phase-matching angles, the intracavity signal power is over 2.5 Watts and the non-resonant idler is over 300 mW in all the tuning range. For the intracavity doubling, we tried several BBO crystals of different thicknesses. With a 2 mm thick BBO, the second harmonic of the signal is over 125 mW in all stable oscillation configurations and achieves 265 mW at 451 nm. The doubled idler is over 9 mW across 580 nm to 680 nm and reaches 25 mW at 581 nm. All visible spectra have bandwidth to support pulses shorter than 150 fs. The spectrum and power of the OPO output is in Figure 6.10. A zoom-in for the spectra and powers of the visible pulses is shown in Figure 6.11.

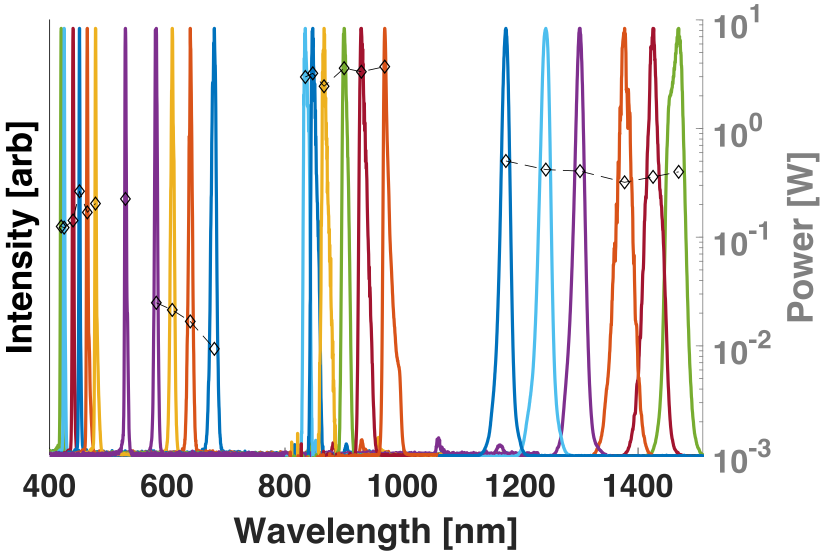

Figure 6.10: The intracavity signal and idler spectra and power at different phase-matching temperatures of LBO in the synchronously pumped optical parametric oscillator. The spectra and power of tunable visible pulses output of the OPO at different phase-matching conditions. The spectrum centered around 530 nm is the residual pump. Optical powers are represented with diamond symbols.

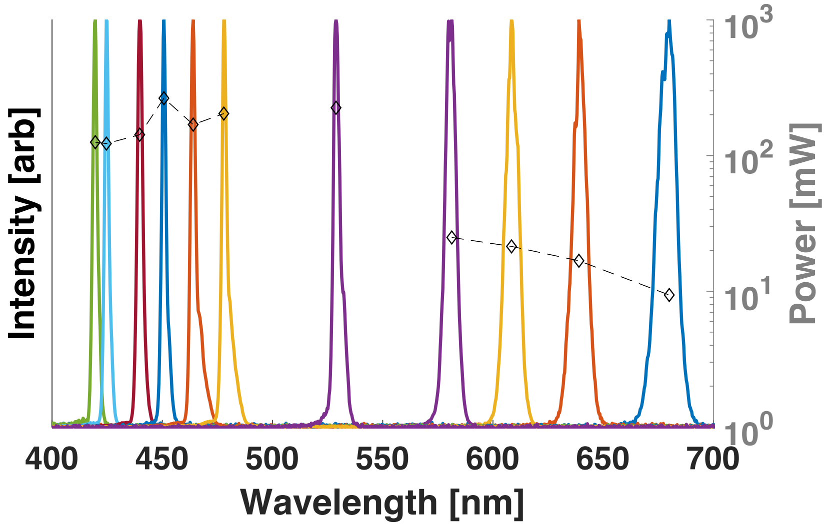

Figure 6.11: The spectra and power of tunable visible generated in the OPO under different phase-matching conditions. The spectrum centered around 530 nm is the residual pump. All powers are represented with diamond symbols.

To verify the tunable visible pulses are still short enough for an ultrafast spectroscopy experiment, we measured the visible pulse durations with a home-built two-photon photodiode autocorrelator. The all-reflective autocorrelator design is similar to the one reported in [142]. The incident beam is split by two D-shaped mirrors with a very narrow gap then arrive a home-built two-photon detector with a SiC photodiode.

Since intracavity frequency doubling significantly lowers the signal and idler powers, the conversion efficiency of parametric oscillation should be measured under two different conditions, e.g., with the 2 mm thick SHG BBO detuned from the phase-matching angle and with the BBO phase-matching angle optimized.

6.5 Locking the OPO to the cavity

The tunable visible pulses are coupled to the visible cavity described in Chapter 5. Locking the OPO to the cavity is achieved using the two-point Pound-Drever-Hall (PDH) lock method [143]. A brief schematic with key components is included in figure 6.12. The reflection from the spectroscopy cavity is used to generate the error signal for the PDH lock in the same fashion as described in section 3.3. The correction signal is generated in a servo loop filter (D2-125, Vescent Photonics, Inc.) and feeds back to an electro-optical-modulator (EOM) in the Er:fiber oscillator laser. The servo also outputs an integrated correction signal, which feeds back to the longer travel piezo in the OPO cavity to correct the slow drift of the OPO cavity length. This is the lock configuration used in measuring the intracavity spectrum shown in Figure 5.9. However, this locking configuration does not work for locking the frequency doubled signal since the phase modulation sidebands transfer to the frequency doubled idler only. The "f_{rep} feedback" signal is sent to the copper bullet style PZT instead of the EOM in the oscillator. Work for fully stabilizing the OPO to the cavity over all tunable visible spectral range is ongoing.

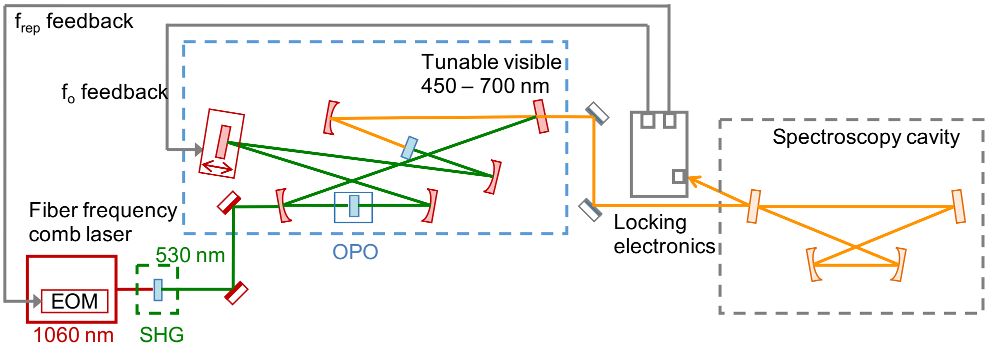

Figure 6.12: A brief schematic of the tunable visible frequency comb stabilization. The error signal for the PDH phase lock is generated with the spectroscopy reflection. The f_{rep} feedback signal is sent to the EOM in the Er:fiber oscillator laser to match the oscillator cavity length to the spectroscopy experiment cavity. The f_o feedbacks to a piezo in the OPO cavity.

6.6 Summary

We present a high power femtosecond tunable visible frequency comb generated in a synchronously pumped optical parametric oscillator pumped by second harmonic of a 11 Watts Yb:fiber frequency comb at 100 MHz repetition rate. The signal and idler cover 830 - 980 nm and 1154 - 1466 nm.

A simple frequency doubling crystal in the OPO converts both the signal and idler to collinear tunable visible across 450 to 700 nm. The application of this light source to widely tunable cavity-enhanced ultrafast spectroscopy to study ultrafast dynamics is currently underway. With over 100 mW of power in some spectral regions, the light source can also be used as a tunable visible pump source for 100 MHz angle-resolved photoemission spectroscopy (ARPES) measurements also going on in the Allison lab.

Chapter 7

Towards ultrafast dynamics of excited state intramolecular proton transfer

Cavity-enhanced ultrafast spectroscopy has been demonstrated to study the electronically excited molecule I_2. The widely tunable spectrometer in UV and visible described in earlier chapter will also focus on the dynamics of electronically excited molecules. In principle, this method could be extended to much broader spectral ranges as long as the low-noise and narrow-linewidth ultrafast frequency comb laser and the low-loss and high-finesse cavity mirrors are achievable in the target frequency. Development towards a mid-infrared version of this spectrometer for studying vibrationally excited molecules and clusters is ongoing in the Allison lab using the infrastructure described in section 2.2. However, this thesis only includes the widely tunable spectrometer operating in the UV and tunable visible. In this broad spectral range, transient absorption measurement with 100 fs temporal resolution in jet-cooled molecules and clusters could benefit understanding of ultrafast dynamics of numerous molecules. Here, we present an example application of widely-tunable cavity-enhanced ultrafast spectroscopy to study the ultrafast dynamics of excited state intramolecular proton transfer.

7.1 Excited-State Intramolecular Proton Transfer dynamics

The dynamics of ESIPT, or excited state hydrogen transfer, has been studied extensively since proton transfer represents an elementary photo-induced reaction in chemistry and biology. ESIPT has been revealed in a wide variety of molecules [144, 145, 146, 147, 148]. A representative molecule of ESIPT is 2-(2'-hydroxyphenyl)benzothiazole, or HBT. A consensus has been reached for the structural changes in the proton transfer process in this molecule, as is shown in the schematic in Figure 7.1.

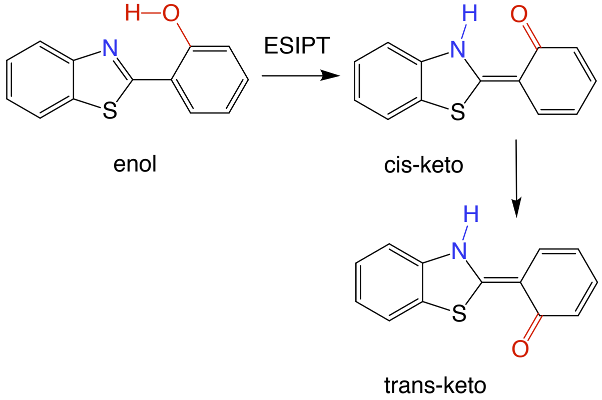

Figure 7.1: The schematic of excited state intramolecular proton transfer in HBT. The atoms directly involved in structural changes are highlighted.

The ground state HBT molecule is stable in the enol form. Upon absorption of a UV photon, the O-H bond breaks and the hydrogen transfers to the nearby nitrogen in the adjacent five-member ring in the same molecule. Following the ultrafast proton transfer, the cis-keto form molecule goes through isomerization, and the trans-keto molecule transfers the hydrogen from the nitrogen back to the oxygen atom [147]. The electronically excited keto formed molecule could dissipate excessive energy via fluorescence and radiationless ways. Both cis and trans keto could emit fluorescence. The trans-keto form molecules produce fluorescence in the visible with a strong Stoke shift from the UV pump wavelength. Figure 7.2 taken from [149] shows the absorption and emission spectrum of HBT in cyclohexane solution. The absorption peak is around 340 nm and the fluorescence of the enol form and keto form peaked at 380 nm and 525 nm, respectively. The strong Stoke's shift is commonly observed in ESIPT molecules and used as an indication for the occurrence of ESIPT.

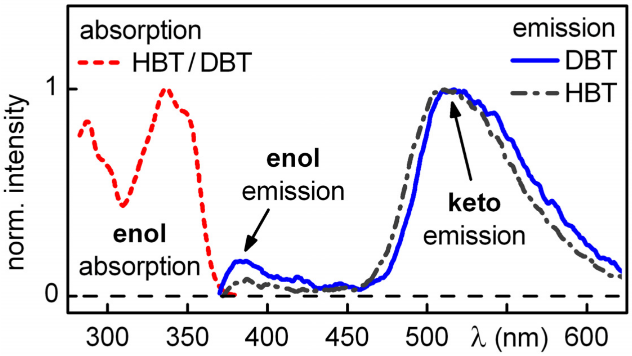

Figure 7.2: Steady state absorption and fluorescence spectra of HBT and DBT. DBT is the deuterated HBT. The figure is taken from the supplemental materials of [149]. Red dashed curve: HBT and DBT absorption spectrum; solid blue curve: fluorescence spectrum of DBT in D_2O saturated cyclohexane; dashed black curve: fluorescence spectrum of HBT in cyclohexane.

There are a few aspects that make ESIPT molecules interesting models for studying dynamics. The proton transfer reactions are mostly ultrafast and the chemical environment does not dramatically affect the reaction rate if the proton transfer is not fully shut off. For instance, the proton transfer of HBT in cyclohexane solution has been measured with transient absorption spectroscopy to be shorter than 50 fs [150]. A time resolved fluorescence measurement reported a time constant of 60 fs in cyclohexane solution [151]. Both time constants are very similar to a transient absorption measurement taken in hot HBT vapor [152]. Though most ESIPT molecules share some common characteristics in the ultrafast proton transfer, the dynamics following the proton transfer strongly depend on the detail of the molecules and the surrounding chemical environment including solvent type, temperature, etc. [153, 154, 155, 156]. A previous transient absorption measurement in hot HBT vapor showed that the internal conversion in hot vapor is 40 times faster than that in the cyclohexane solution [147]. This is explained by the authors that the skeleton torsion is slowed down by the friction from solvent molecules, which is absent in the hot vapor.

7.2 Studying ESIPT with widely tunable cavity enhanced ultrafast spectroscopy

With our tunable UV/visible cavity-enhanced ultrafast spectroscopy, we could measure the internal conversion rate of ESIPT molecules in a supersonic expansion. A comparison between our jet-cooled molecule measurement and the hot vapor transient absorption measurement could provide information about the influence of initial thermally populated vibrational states. Our results could also be compared with theoretical simulations done for gas phase molecules [157].

Another proposed experiment is applying UV pump and mid-IR probe to ESIPT molecules. In this way, we could initiate the proton transfer process with the femtosecond UV light then probe some of the vibrational modes. We could probe the OH stretch modes to directly probe the potential along the proton transfer coordinate, or probe the C=O stretch to measure the internal conversion time constant.

Since all these above measurements could be taken in a supersonic expansion, we are able to do the experiments in cold and isolated molecules free from perturbation from the environment as well as in clusters of ESIPT molecules with solvent molecules. Hydrogen bonding has been shown to alter the ESIPT in a significant way. A picosecond time resolved fluorescence measurement in jet-cooled 3-hydroxyflavone(3-HF) shows that the fluorescence lifetime in 3-HF methanol clusters is 16 ns instead of 150 ps in isolated 3-HF [158]. While another measurement using different supersonic expansion conditions and excitation wavelength concluded the prohibition of ESIPT in 3-hydroxyflavone methanol clusters. [156] The effect of hydrogen bonding on the ESIPT dynamics has been theoretically investigated for HBT [157], 1-hydroxy-2-acetonaphthone [159] using calculations in clusters. The UV pump and mid-IR probe measurement with fs temporal resolution in clusters of ESIPT molecules and protonic solvents allows probing of hydrogen bonding effect on ESIPT.

Besides the benefits for fundamental understanding in this very basic and common photoinduced reaction, more comprehensive knowledge in the ESIPT dynamics could also provide insights for the development of ESIPT based functional materials, such as luminescence emitters [160, 161, 162], white light generation materials [163, 164], and molecular probe [165] .etc.

7.3 UV-vis cavity enhanced ultrafast spectroscopy signal estimation

The UV and tunable visible frequency comb generation and experimental setup are described in earlier chapters. A signal estimation for the UV pump and tunable visible probe experiment on 1-hydroxy-2-acetonaphthone (HAN) in a molecular beam is shown here. A schematic of ESIPT in HAN is shown in Figure 7.3. Here, we calculate the fraction of molecules excited by the pump, the molecule number density in our molecular beam jet, the probe absorbance enhancement factor and then estimate the pump-probe absorption signal based on these numbers.

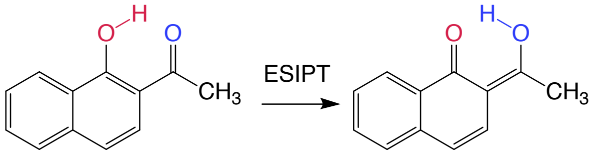

Figure 7.3: The schematic of ESIPT in 1-hydroxy-2-acetonaphthone. The atoms directly involved in structural changes are highlighted.

7.3.1 UV photon density

For the pump beam photon density, the power in the pump cavity has been demonstrated to be up to 11 Watts. However, we keep the excitation ratio to 1% or less to avoid multiphoton excitation of the molecules. The pump beam waist radius at the focus of the cavity is calculated to be 80 μm using ABCD matrix, so the beam area A is $\sim 2.0 \times 10^{-4}$ cm^2. With average power of 11 W, the repetition rate $\mathrm{f_{rep}}$ of 100 MHz and the center wavelength λ at 350 nm, the photon density is calculated with Equation 7.1 to be 9.6×10^{14} photons/cm^2.

$$\text{photon density} \approx \frac{P}{f_{rep} h\nu \mathrm{A}} \tag{7.1}$$

7.3.2 UV absorption cross-section

To calculate the excitation fraction of molecules with this photon density, we also need the cross-section of molecules at the pump wavelength. Ma *et al.* [166] reported a static absorption spectrum of HBT in toluene at

20°C, the absorbance is ~ 0.15 at 350 nm when measured with a commercial spectrometer, the standard cuvette of which is 1 cm long. According to Beer's law in Eqn. 7.2 and absorbance in Eqn. 7.3, here path length l is 1 cm and number density is 6.0×10^{15} molecules/cm^3, the cross-section σ is 5.7×10^{-17} cm^2/molecule. In another paper reported by Dharia *et al.*, the cross-section of 3-HF in tetrahydrofuran solvent at 350 nm calculated in similar fashion is surprisingly also 5.7×10^{-17} cm^2/molecule. This is the cross-section we use for this signal estimation calculation.

$$I = I_0 e^{-nl\sigma} \tag{7.2}$$

$$\text{Absorbance} = log_{10} \frac{I_0}{I} \tag{7.3}$$

The product of photon density and the cross-section gives the excitation fraction of molecules, as in 7.4. In this calculation, the excitation ratio is 4.8%. To have 1% excitation ratio, we only need 2.3 W of UV light in the cavity at focus.

$$\epsilon = \sigma \times \text{photon density} \tag{7.4}$$

7.3.3 ESIPT molecule vapor pressure

The ESIPT molecules that we use for are all powders at room temperature. To increase the vapor pressures, we heat up the aluminum sample pick-up cell and the sample delivery lines downstream. The cell temperature is stabilized to a temperature between 50°C and 130°C depending on the molecule. The vapor pressure database [167] reported a vapor pressure of 0.75 Torr at 107°C. This is roughly consistent with estimation by Arthen-Engeland *et al.* [168] that the vapor pressure of 3-HF is less than 1 Torr at 126°C. Based on these vapor pressures, we assume a 0.5 Torr as the molecule vapor pressure in the following calculation.

7.3.4 ESIPT molecule number density

Since the molecule is introduced to the overlap of the pump and probe cavity focus in a supersonic expansion, the nozzle opening shape, size and position could influence the molecule's number density. For the ESIPT experiment, we use a slit nozzle that's 200 μm wide and 5 mm long. The nozzle is placed 1 mm below the pump and probe beams. The backing pressure P_0 is mostly

300 Torr to 1000 Torr. The molecules expand from this backing pressure to a pressure P_0 of tens of mTorr. The pressure ratio P_0/P_b exceeds a critical value of G = 2.1 [111], where γ in Equation 7.5 is the specific heat of the gas under expansion.

$$G = ((\gamma + 1)/2)^{\gamma/(\gamma-1)} \tag{7.5}$$

Being 1 mm away from the 0.2 mm wide slit nozzle, the Mach number is 3.56. Using the expansion condition and a 0.5 Torr of vapor pressure and 400 K as the gas temperature, we calculate the number density of the molecule is $2\times10^{15}/\mathrm{cm}^3$. To ensure the pump probe experiment is in the quiet expansion zone, the Mach disk location, where the shock wave appears, is calculated with Eqn. 7.6. With a P_0 of 100 mTorr and P_b of 760 Torr, the Mach disk is 11.7 mm away from the nozzle.

$$\frac{x_m}{d} = 0.67 \cdot (\frac{P_0}{P_b})^{1/2} \tag{7.6}$$

7.3.5 The pump-probe signal

With the numbers we calculated above, the pump-probe signal could be derived as in Eqn. 7.7. The nϵ is the number density of molecules excited by the pump pulses, $\mathcal{F}/\pi$ is the enhancement factor introduced by the probe cavity, l is the interaction length, and σ_{probe} is the cross-section of excited molecules in the visible.

$$\Delta OD = -\log_{10}(e)(n\epsilon l\sigma_{probe}) \tag{7.7}$$

The angle between the pump and probe beam is set to be smaller than 3°, so the lower limit of interaction length is 1.5 mm, as the nozzle opening length. Assuming the absorption cross-section at visible probe wavelength is an order of magnitude smaller than the pump absorption cross-section, we get the single pass ΔOD is 7×10^{-6}. The signal is higher than the noise level of the instrument by orders of magnitude.

7.4 Discussion of cavity-enhanced ultrafast spectroscopy

The ability to average for long times, due to high frequency modulation/demodulation and the noise canceling scheme unique to cavity-enhanced ultrafast spectroscopy, is remarkable when compared to the performance of other cavity-enhanced spectroscopies, which often reach a flicker noise floor within a few minutes. Still, the current measurement remains technical noise limited. Based on previous work in suppressing noise in CE-DFCS [108, 169], achieving shot-noise limited detection should be possible, which would reduce the detection limit of the current system by one order of magnitude. Furthermore, the probe cavity finesse of 370 used in the demonstration experiment is quite modest for cavity-enhanced spectroscopy, and this can also be improved along with the time-resolution and probe pulse bandwidths that can be achieved [170, 171]. There will likely be trade-offs between the cavity finesse and the bandwidth and tunability of the probe light due to cavity-mirror dispersion [172]. We are also extending this technique to UV, tunable visible and infrared. The probe light can be spectrally resolved as in conventional transient absorption spectroscopy, and multidimensional spectroscopy can be performed via phase cycling methods [173].

Even with the current performance, cavity-enhanced ultrafast spectroscopy easily extends all-optical ultrafast spectroscopy to a vast array of interesting systems that can only be produced in supersonic expansions. Assuming that pump-induced changes in the absorption are on the same order of magnitude of the ground state absorption, exciting 2% of the molecules, one can study samples with optical density as small as 10^{-8}. For I_2, with an absorption cross section of 3×10^{-18} cm^2 [119], this translates to a column density less than 10^{10} molecules/cm^2. As an example system of interest, consider the small gas-phase water clusters $(H_2O)_n$, which can be produced via molecular beam methods with column densities and optical densities larger than our detection limit [16]. Linear spectroscopy has been performed on these systems using cavity ring-down methods and action spectroscopy [16, 174], but the small clusters are expected to dissociate in 10's of ps upon vibrational excitation [175], necessitating ultrafast techniques to record fleeting vibrational coherences. The application of ultrafast infrared spectroscopy to small water clusters, where one can assemble the liquid ”one molecule at a time” [176], could allow systematic studies of the dynamics of hydrogen bond networks with unprecedented detail. Reducing the detection limit further, as discussed above, and increasing the interaction length by using a slit nozzle, could potentially allow for measurements on trapped mass-selected ion clusters [177, 178], where an even higher degree of control over cluster composition and temperature is attainable.

Cavity-enhanced ultrafast spectroscopy with only a probe cavity could also benefit other optical measurements. For example, correlated electron systems in condensed matter at low temperature [11, 12] must be excited very weakly to avoid undesired thermal effects, and this has limited efforts to study the dynamics of complex materials [179]. It is in principle possible to incorporate a solid sample into the probe cavity either as a component of a mirror coating or as a wafer at Brewster's angle to perform ultrasensitive time-resolved measurements on solids as well.

Other researchers have also applied frequency combs to nonlinear spectroscopy, mostly with the goal of high resolution. For instance, Ideguchi *et al.* have demonstrated high-resolution Coherent anti-Stokes Raman spectroscopy (CARS) using frequency comb methods [180] and recently Lomsadze and Cundiff have demonstrated high-resolution multidimensional spectroscopy [181]. Implementing the cavity-enhancement developed here could also benefit these other comb-based nonlinear spectroscopies, particularly since as the resolution is improved, the power per spectral element, and thus nonlinear signal size, is inherently reduced.

Appendix 8

Appendix

8.A Mechanical drawings

8.A.1 Slit nozzle jet

The molecular beam drawing is included here.

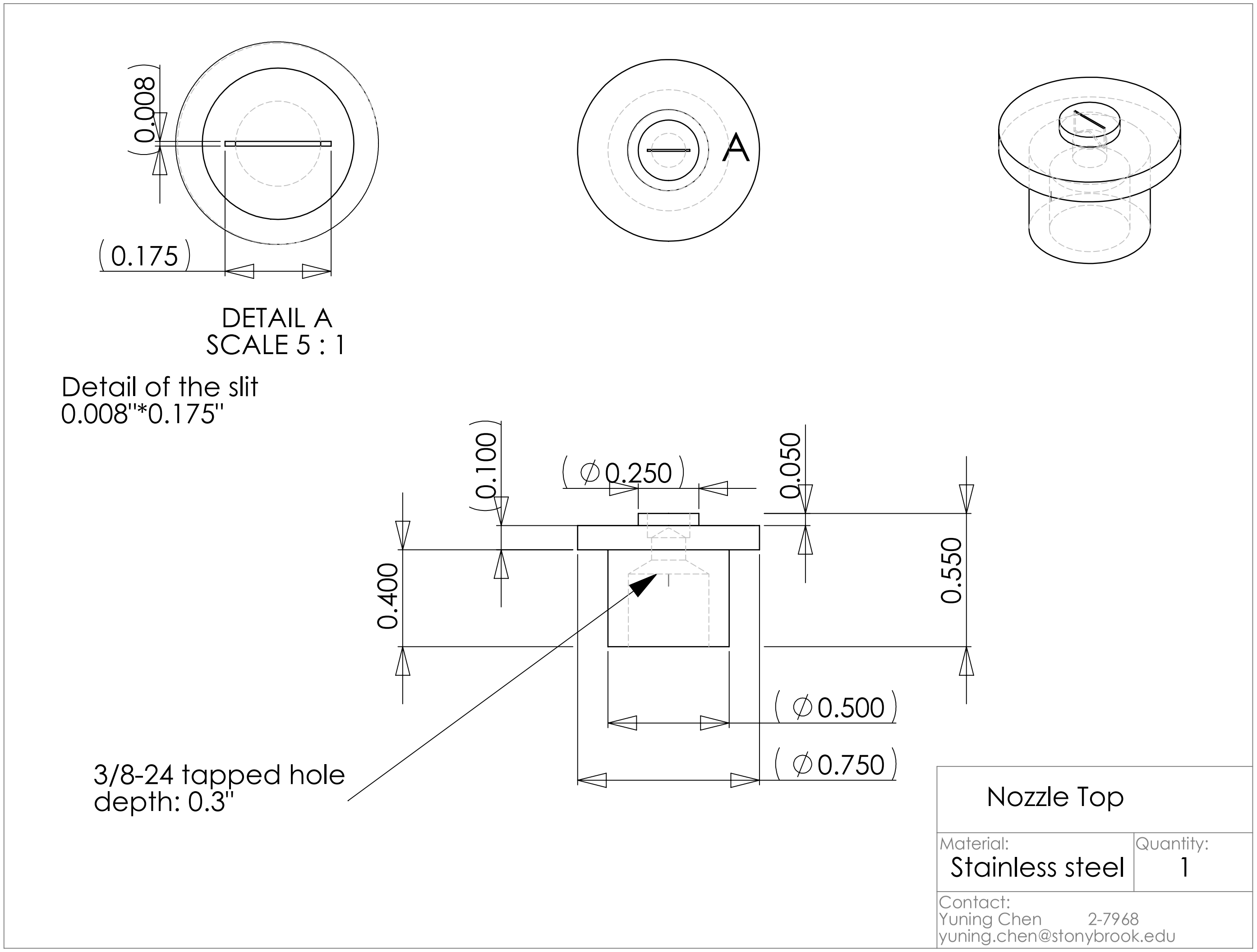

Detail of the slit
0.008"*0.175"

3/8-24 tapped hole
depth: 0.3"

Nozzle Top

Material:
Stainless steel

Quantity:
1

Contact:
Yuning Chen 2-7968
yuning.chen@stonybrook.edu

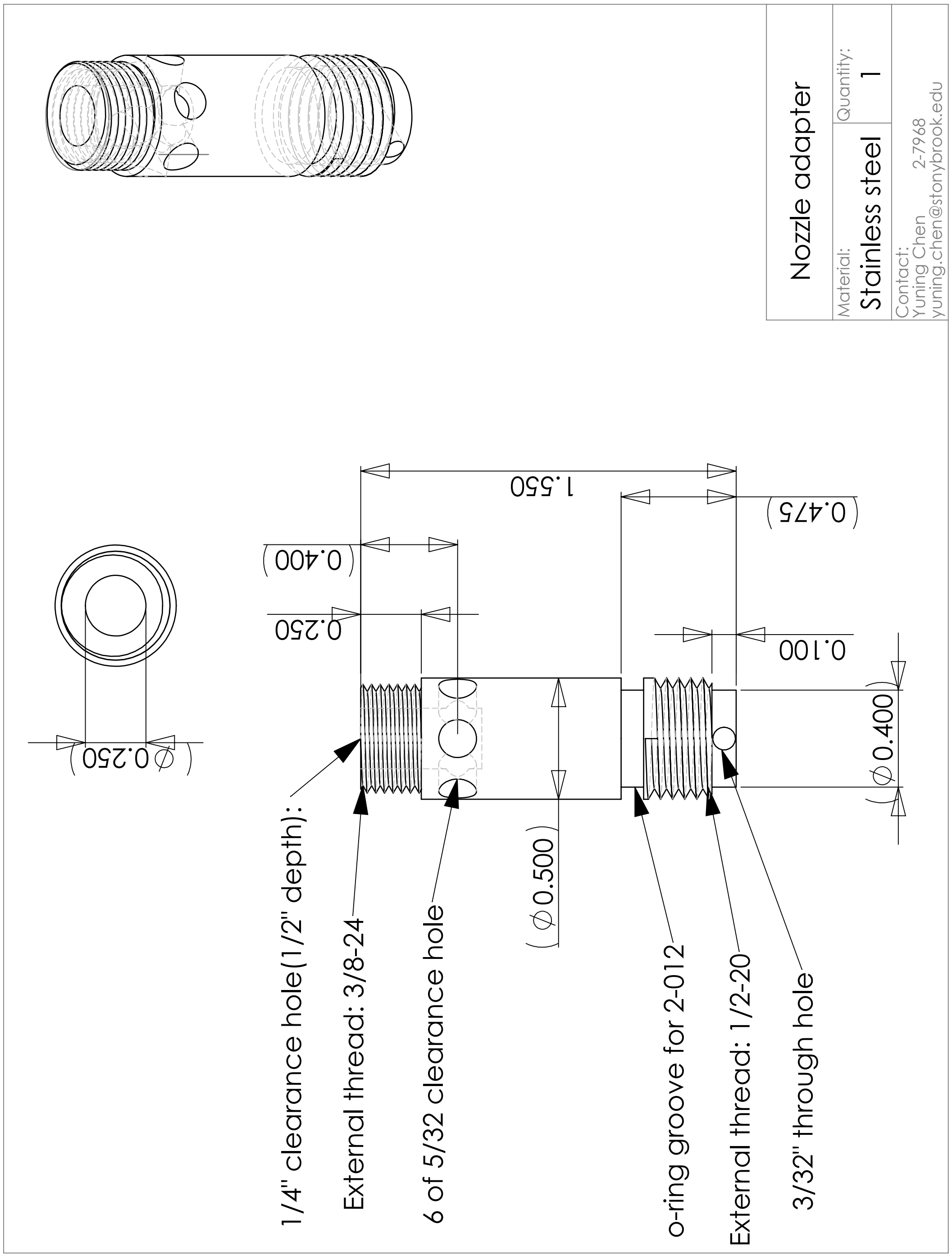
Nozzle adapter
Material:
Stainless steel
Quantity:
1
Contact:
Yuning Chen 2-7968
yuning.chen@stonybrook.edu
(⌀0.250)
1.550
(0.475)
(0.400)
0.250
0.100
(⌀0.400)
(⌀0.500)
1/4" clearance hole(1/2" depth):
External thread: 3/8-24
6 of 5/32 clearance hole
o-ring groove for 2-012
External thread: 1/2-20
3/32" through hole

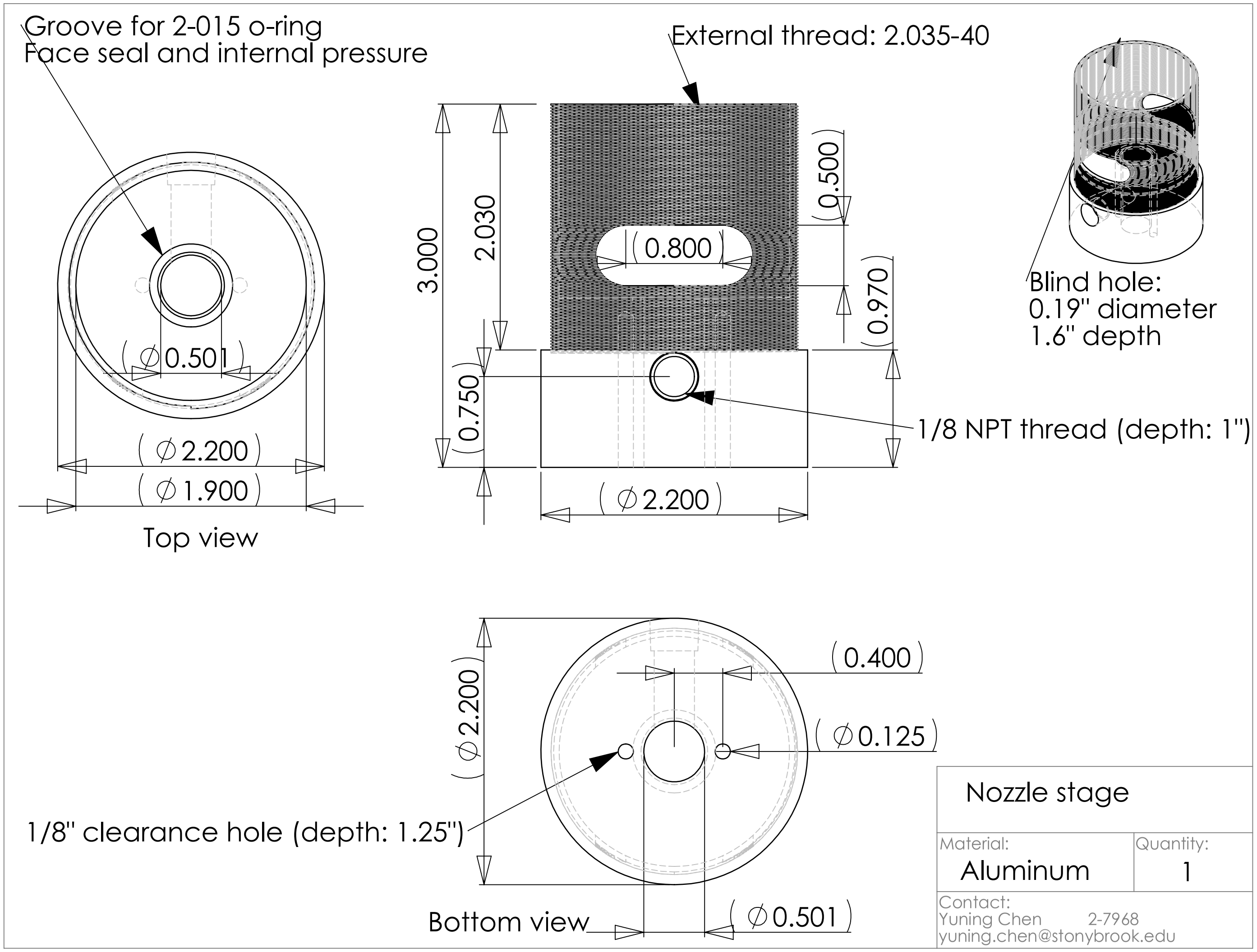
Groove for 2-015 o-ring
Face seal and internal pressure
External thread: 2.035-40
Blind hole:
0.19" diameter
1.6" depth
(⌀0.501)
(⌀2.200)
(⌀1.900)
Top view
3.000
2.030
(0.750)
(0.800)
(0.500)
(0.970)
(⌀2.200)
1/8 NPT thread (depth: 1")
(⌀2.200)
(0.400)
(⌀0.125)
1/8" clearance hole (depth: 1.25")
Bottom view
(⌀0.501)
Nozzle stage
Material:
Aluminum
Quantity:
1
Contact:
Yuning Chen 2-7968
yuning.chen@stonybrook.edu

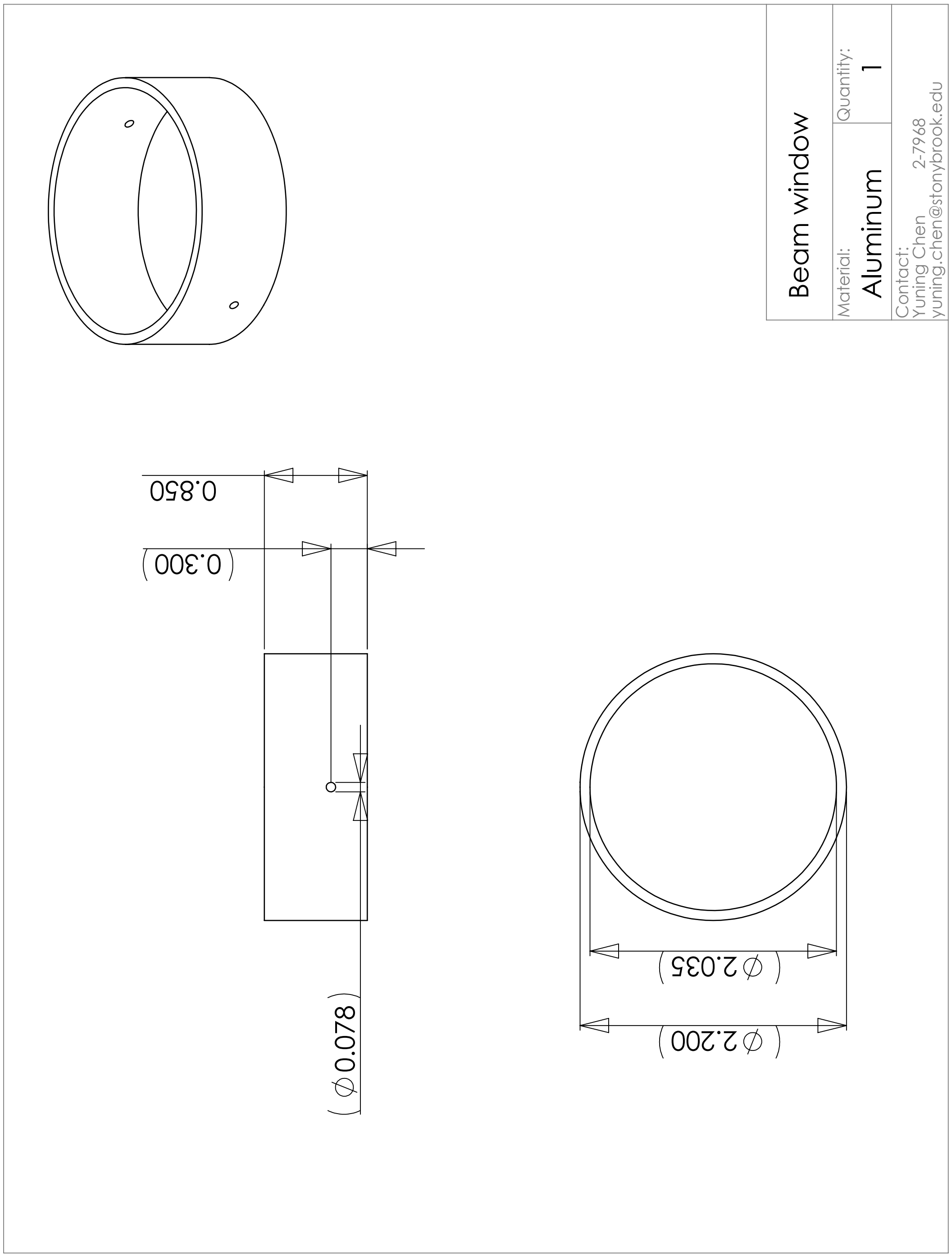
Beam window
Material:
Aluminum
Quantity:
1
Contact:
Yuning Chen 2-7968
yuning.chen@stonybrook.edu
0.850
(0.300)
(⌀0.078)
(⌀2.035)
(⌀2.200)

8.B Electronics circuit diagram

8.B.1 Ultralow noise Si detector

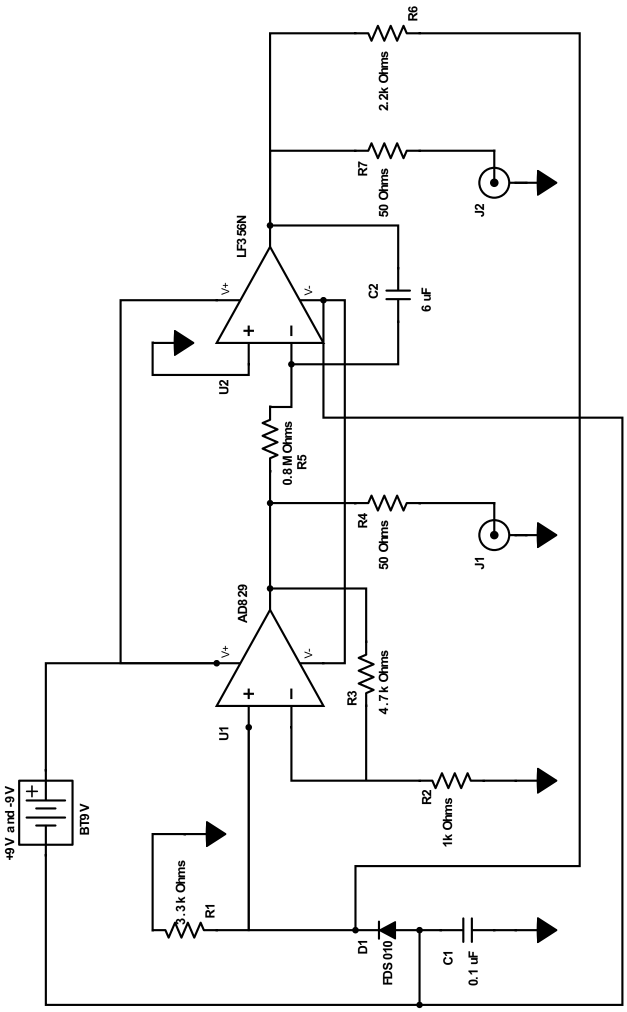

8.B.2 Integrator

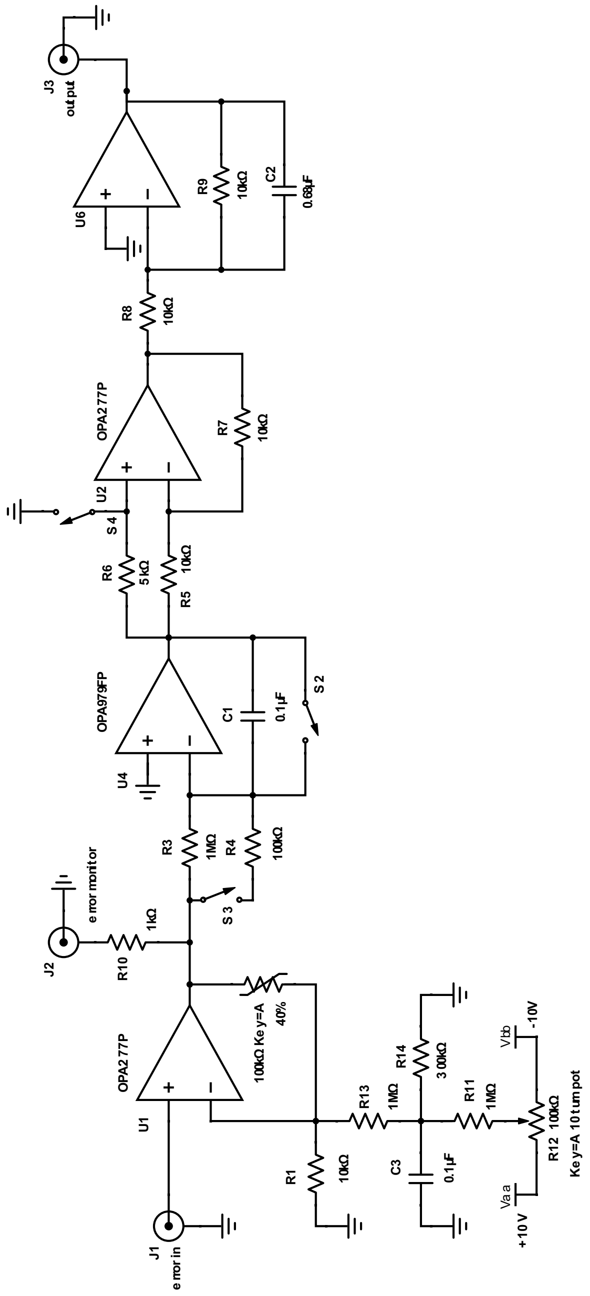

8.B.3 Bias Tee

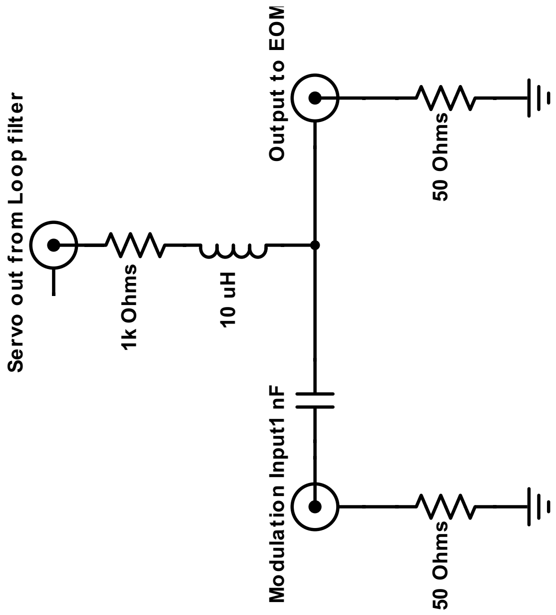
Servo out from Loop filter
1k Ohms
10 uH
Output to EOM
50 Ohms
Modulation Input
1 nF
50 Ohms

Bibliography

[1] Rudi Berera, Rienk van Grondelle, and John T M Kennis. Ultrafast transient absorption spectroscopy: principles and application to photosynthetic systems. *Photosynthesis Research*, 101(2-3):105–118, July 2009.

[2] Haik Chosrowjan, Seiji Taniguchi, and Fumio Tanaka. Ultrafast fluorescence upconversion technique and its applications to proteins. *The FEBS Journal*, 282(16):3003–3015, January 2015.

[3] Christian Bressler and Majed Chergui. Ultrafast X-ray Absorption Spectroscopy. *Chemical Reviews*, 104(4):1781–1812, April 2004.

[4] Albert Stolow, Arthur E Bragg, and Daniel M Neumark. Femtosecond Time-Resolved Photoelectron Spectroscopy. *Chemical Reviews*, 104(4):1719–1758, April 2004.

[5] Mauro Nisoli, Piero Decleva, Francesca Calegari, Alicia Palacios, and Fernando Martín. Attosecond Electron Dynamics in Molecules. *Chemical Reviews*, 117(16):10760–10825, May 2017.

[6] Jan Philip Kraack and Peter Hamm. Surface-Sensitive and Surface-Specific Ultrafast Two-Dimensional Vibrational Spectroscopy. *Chemical Reviews*, 117(16):10623–10664, May 2017.

[7] P Hamm and M T Zanni. *Concepts and Methods of 2D Infrared Spectroscopy.* Cambridge University Press, 2011.

[8] C Schriever, Stefan Lochbrunner, Eberhard Riedle, and D J Nesbitt. Ultrasensitive ultraviolet-visible 20 fs absorption spectroscopy of low vapor pressure molecules in the gas phase. *Rev. Sci. Instrum.*, 79(1):013107, 2008.

[9] Davide Boschetto, Leandro Malard, Chun Hung Lui, Kin Fai Mak, Zhiqiang Li, Hugen Yan, and Tony F Heinz. Real-Time Observation of Interlayer Vibrations in Bilayer and Few-Layer Graphene. *Nano Letters*, 13(10):4620–4623, 2013.

[10] K Röttger, S Wang, F Renth, J Bahrenburg, and F Temps. A femtosecond pump-probe spectrometer for dynamics in transmissive polymer films. *Applied Physics B*, 118(2):185–193, 2015.

[11] D N Basov, Richard D Averitt, Dirk van der Marel, Martin Dressel, and Kristjan Haule. Electrodynamics of correlated electron materials. *Reviews of Modern Physics*, 83:471–541, June 2011.

[12] Joseph Orenstein. Ultrafast spectroscopy of quantum materials. *Physics Today*, 65(9):44–50, 2012.

[13] Nadja Heine and Knut R Asmis. Cryogenic ion trap vibrational spectroscopy of hydrogen-bonded clusters relevant to atmospheric chemistry. *International Reviews in Physical Chemistry*, 34(1):1–34, 2015.

[14] David J Nesbitt. High-resolution infrared spectroscopy of weakly bound molecular complexes. *Chemical Reviews*, 88(6):843–870, 1988.

[15] Gordon G Brown, Brian C Dian, Kevin O Douglass, Scott M Geyer, Steven T Shipman, and Brooks H Pate. A broadband Fourier transform microwave spectrometer based on chirped pulse excitation. *Review of Scientific Instruments*, 79(5), 2008.

[16] J B Paul, C P Collier, R J Saykally, J J Scherer, and A O'Keefe. Direct Measurement of Water Cluster Concentrations by Infrared Cavity Ringdown Laser Absorption Spectroscopy. *The Journal of Physical Chemistry A*, 101(29):5211–5214, 1997.

[17] G Tejeda, B Mate, J M Fernandez-Sanchez, and S Montero. Temperature and Density Mapping of Supersonic Jet Expansions Using Linear Raman Spectroscopy . *Physical Review Letters*, 76:1–4, December 1996.

[18] K Kosma, S A Trushin, W Fuss, and W E Schmid. Ultrafast Dynamics and Coherent Oscillations in Ethylene and Ethylene-d4 Excited at 162 nm. *The Journal of Physical Chemistry A*, 112(33):7514–7529, 2008.

[19] Chris T Middleton, Kimberly de La Harpe, Charlene Su, Yu Kay Law, Carlos E Crespo-Hernández, and Bern Kohler. DNA Excited-State Dynamics: From Single Bases to the Double Helix. *Annual Review of Physical Chemistry*, 60(1):217–239, 2009.

[20] Hiroyuki Saigusa. Excited-state dynamics of isolated nucleic acid bases and their clusters. *J. Photochem. Photobio. C*, 7(4):197–210, 2006.

[21] Richard E Smalley, Lennard Wharton, and Donald H Levy. Molecular optical spectroscopy with supersonic beams and jets. *Accounts of Chemical Research*, 10(4):139–145, May 1977.

[22] O F Hagena and W Obert. Cluster Formation in Expanding Supersonic Jets: Effect of Pressure, Temperature, Nozzle Size, and Test Gas. *The Journal of Chemical Physics*, 56(5):1793–1802, March 1972.

[23] Gianluca Gagliardi and Hans-Peter Loock, editors. *Cavity Enhanced Spectroscopy and Sensing*. Springer, 2013.

[24] Akira Matsugi, Hiroumi Shiina, Tatsuo Oguchi, and Kazuo Takahashi. Time-Resolved Broadband Cavity-Enhanced Absorption Spectroscopy behind Shock Waves. *The Journal of Physical Chemistry A*, 120(13):2070–2077, March 2016.

[25] G Giusfredi, S Bartalini, S Borri, P Cancio, I Galli, D Mazzotti, and P De Natale. Saturated-Absorption Cavity Ring-Down Spectroscopy. *Physical Review Letters*, 104(11):110801–110804, March 2010.

[26] Warren Nagourney. *Quantum Electronics for Atomic Physics*. Oxford University Press, 2010.

[27] Th Udem, R Holzwarth, and T W Hansch. Optical frequency metrology. *Nature*, 416:233–237, March 2002.

[28] Andrew D Ludlow, Martin M Boyd, Jun Ye, E Peik, and P O Schmidt. Optical atomic clocks. *Reviews of Modern Physics*, 87(2):637–701, June 2015.

[29] M J Thorpe and J Ye. Cavity-enhanced direct frequency comb spectroscopy. *Applied Physics B*, 91(3-4):397–414, May 2008.

[30] J L Hall, J Ye, S A Diddams, Long-Sheng Ma, S T Cundiff, and D J Jones. Ultrasensitive spectroscopy, the ultrastable lasers, the ultrafast lasers, and the seriously nonlinear fiber: a new alliance for physics and metrology. *IEEE J. Quantum Elec.*, 37(12):1482–1492, 2001.

[31] Ian Coddington, Nathan Newbury, and William Swann. Dual-comb spectroscopy. *Optica*, 3(4):414–413, 2016.

[32] Florian Adler, Michael J Thorpe, Kevin C Cossel, and Jun Ye. Cavity-Enhanced Direct Frequency Comb Spectroscopy: Technology and Applications. *Annual Review of Analytical Chemistry*, 3(1):175–205, 2010.

[33] Christoph Gohle, Bj orn Stein, Albert Schliesser, Thomas Udem, and Theodor W H ansch. Frequency Comb Vernier Spectroscopy for Broadband, High-Resolution, High-Sensitivity Absorption and Dispersion Spectra. *Physical Review Letters*, 99:263902, December 2007.

[34] Titus Gherman and Daniele Romanini. Modelocked Cavity–Enhanced Absorption Spectroscopy. *Optics Express*, 10(19):1033–1042, September 2002.

[35] A Foltynowicz, P Masłowski, A J Fleisher, B J Bjork, and J Ye. Cavity-enhanced optical frequency comb spectroscopy in the mid-infrared application to trace detection of hydrogen peroxide. 110(2):163–175, 2013.

[36] Birgitta Bernhardt, Akira Ozawa, Patrick Jacquet, Marion Jacquey, Yohei Kobayashi, Thomas Udem, Ronald Holzwarth, Guy Guelachvili, Theodor W Hänsch, and Nathalie Picqué. Cavity-enhanced dual-comb spectroscopy. *Nat. Photon.*, 4(1):55–57, January 2010.

[37] Michael J Thorpe, David Balslev-Clausen, Matthew S Kirchner, and Jun Ye. Cavity-enhanced optical frequency combspectroscopy: application to human breathanalysis. *Optics Express*, 16(4):2387–2397, February 2008.

[38] Adam J Fleisher, Bryce J Bjork, Thinh Q Bui, Kevin C Cossel, Mitchio Okumura, and Jun Ye. Mid-Infrared Time-Resolved Frequency Comb Spectroscopy of Transient Free Radicals. *The Journal of Physical Chemistry Letters*, 5(13):2241–2246, 2014.

[39] Craig Benko, Linqiang Hua, Thomas K Allison, Fran ç c ois Labaye, and Jun Ye. Cavity-Enhanced Field-Free Molecular Alignment at a High Repetition Rate. *Physical Review Letters*, 114:153001, April 2015.

[40] D R Carlson, Tsung-Han Wu, and R J Jones. Dual-comb femtosecond enhancement cavity for precision measurements of plasma dynamics and spectroscopy in the XUV. In *Conference on Lasers and Electro-Optics (CLEO).*, 2015.

[41] Rudi Berera, Rienk Grondelle, and JohnT M Kennis. Ultrafast transient absorption spectroscopy: principles and application to photosynthetic systems. *Photosynthesis Research*, 101(2-3):105–118, 2009.

[42] Udem Th. The Frequency Comb (R)evolution. In *Winter College on Optics: Optical Frequency Combs - from multispecies gas sensing to high precision interrogation of atomic and molecular targets*, International Centre for Theoretical Physics, February 2016.

[43] Th Udem, J Reichert, R Holzwarth, and T W H a nsch. Accurate measurement of large optical frequency differences with a mode-locked laser. *Optics Letters*, 24(13):881–883, July 1999.

[44] M E Fermann and I Hartl. Ultrafast Fiber Laser Technology. *IEEE Journal of Selected Topics in Quantum Electronics*, 15(1):191–206, January 2009.

[45] Andy Chong, Joel Buckley, Will Renninger, and Frank Wise. All-normal-dispersion femtosecond fiber laser. *Optics Express*, 14(21):10095–10100, October 2006.

[46] S M J Kelly. Characteristic sideband instability of periodically amplified average soliton. *Electronics Letters*, 28(8):806–807, April 1992.

[47] Martin Baumgartl, Caroline Lecaplain, Ammar Hideur, Jens Limpert, and Andreas T u nnermann. 66 W average power from a microjoule-class sub-100 fs fiber oscillator. *Optics Letters*, 37(10):1640–1642, May 2012.

[48] Lora Nugent-Glandorf, Todd A Johnson, Yohei Kobayashi, and Scott A Diddams. Impact of dispersion on amplitude and frequency noise in a Yb-fiber laser comb. *Optics Letters*, 36(9):1578–1580, May 2011.

[49] R Paschotta. Noise of mode-locked lasers (Part I): numerical model. *Applied Physics B*, 79(2):153–162, 2004.

[50] R Paschotta. Noise of mode-locked lasers (Part II): timing jitter and other fluctuations. *Applied Physics B*, 79(2):163–173, 2004.

[51] Ingmar Hartl, Genady Imeshev, Liang Dong, Gyu C Cho, and Martin E Fermann. Ultra-Compact Dispersion Compensated Femtosecond Fiber Oscillators and Amplifiers. In *Conference on Lasers and Electro-Optics/Quantum Electronics and Laser Science and Photonic Applications Systems Technologies*, page CThG1. Optical Society of America, 2005.

[52] Thomas R Schibli, I Hartl, Dylan C Yost, M J Martin, A Marcinkevicius, M E Fermann, and J Ye. Optical frequency comb with submillihertz linewidth and more than 10 W average power. *Nat. Photon*, 2(6):355–359, June 2008.

[53] Xiangyu Zhou, Dai Yoshitomi, Yohei Kobayashi, and Kenji Torizuka. Generation of 28-fs pulses from a mode-locked ytterbium fiber oscillator. *Optics Express*, 16(10):7055–7059, May 2008.

[54] J R Buckley, S W Clark, and F W Wise. Generation of ten-cycle pulses from an ytterbium fiber laser with cubic phase compensation. *Optics Letters*, 31(9):1340–1342, May 2006.

[55] G P Agrawal. *Nonlinear Fiber Optics*. Academic Press, 2012.

[56] G P Agrawal. *Applications of Nonlinear Fiber Optics*. Academic Press, 2008.

[57] M Hofer, M H Ober, F Haberl, and M E Fermann. Characterization of ultrashort pulse formation in passively mode-locked fiber lasers. *IEEE J. Quantum Elec.*, 28(3):720–728, 1992.

[58] Andrew Weiner. *Ultrafast Optics*. Wiley, 2009.

[59] N Newbury. Understanding noise sources and stabilization strategies in frequency combs - part 2. 2016.

[60] L C Sinclair, J D Desch $^{\text{TM}}$ nes, L Sonderhouse, W C Swann, I H Khader, E Baumann, N R Newbury, and I Coddington. Invited Article: A compact optically coherent fiber frequency comb. *Review of Scientific Instruments*, 86(8), 2015.

[61] Axel Ruehl, Andrius Marcinkevicius, Martin E Fermann, and Ingmar Hartl. 80 W, 120 fs Yb-fiber frequency comb. *Optics Letters*, 35(18):3015–3017, September 2010.

[62] Fatih Ömer Ilday, J Chen, and F X K a rtner. Generation of sub-100-fs pulses at up to 200 MHz repetition rate from a passively mode-locked Yb-doped fiber laser. *Optics Express*, 13(7):2716–2721, 2005.

[63] Nathan R Newbury and William C Swann. Low-noise fiber-laser frequency combs (Invited). *Journal of the Optical Society of America B*, 24(8):1756–1770, 2007.

[64] Katherine J Bock. *Femtosecond Fiber Lasers*. PhD thesis, School of Electrical Engineering and Computer Science, University of Ottawa, Ottawa, Canada, 2012.

[65] Jinendra K Ranka, Alexander L Gaeta, Andrius Baltuska, Maxim S Pshenichnikov, and Douwe A Wiersma. Autocorrelation measurement of 6-fs pulses based on the two-photon-induced photocurrent in a GaAsP photodiode. *Optics Letters*, 22(17):1344–1346, September 1997.

[66] W H Knox. In situ measurement of complete intracavitydispersion in an operating Ti:sapphire femtosecond laser. *Optics Letters*, 17(7):514–516, 1992.

[67] A Cing o z, Dylan C Yost, T K Allison, A Ruehl, M E Fermann, I Hartl, and J Ye. Broadband phase noise suppression in a Yb-fiber frequency comb. *Optics Letters*, 36(5):743–745, March 2011.

[68] Kasturi Saha, Yoshitomo Okawachi, Bonggu Shim, Jacob S Levy, Reza Salem, Adrea R Johnson, Mark A Foster, Michael R E Lamont, Michal Lipson, and Alexander L Gaeta. Modelocking and femtosecond pulse generation in chip-based frequency combs. *Optics Express*, 21(1):1335–1343, January 2013.

[69] M Kourogi, K Nakagawa, and M Ohtsu. Wide-span optical frequency comb generator for accurate optical frequency difference measurement. *IEEE J. Quantum Elec.*, 29(10):2693–2701, October 1993.

[70] N Kuse, C C Lee, J Jiang, C mohr, Thomas R Schibli, and M E Fermann. Ultra-low noise all polarization-maintaining Er fiber-based optical frequency combs facilitated with a graphene modulator. *Optics Express*, 23(19):24342–24350, September 2015.

[71] Darren D Hudson, Kevin W Holman, R Jason Jones, Steven T Cundiff, Jun Ye, and David J Jones. Mode-locked fiber laser frequency-controlled with an intracavity electro-optic modulator. *Optics Letters*, 30(21):2948–2950, 2005.

[72] W Zhang, M Lours, M Fischer, R Holzwarth, G Santarelli, and Y L Coq. Characterizing a fiber-based frequency comb with electro-optic modulator. *IEEE Transactions on Ultrasonics, Ferroelectrics and Frequency Control*, 59(3):432–438, 2012.

[73] Kana Iwakuni, Hajime Inaba, Yoshiaki Nakajima, Takumi Kobayashi, Kazumoto Hosaka, Atsushi Onae, and Feng-Lei Hong. Narrow linewidth comb realized with a mode-locked fiber laser using an intra-cavity waveguide electro-optic modulator for high-speed control. *Optics Express*, 20(13):13769–13776, 2012.

[74] William C Swann, Esther Baumann, Fabrizio R Giorgetta, and Nathan R Newbury. Microwave generation with low residual phase noise from a femtosecond fiber laser with an intracavity electro-optic modulator. *Optics Express*, 19(24):24387–24395, November 2011.

[75] Yoshiaki Nakajima, Hajime Inaba, Kazumoto Hosaka, Kaoru Minoshima, Atsushi Onae, Masami Yasuda, Takuya Kohno, Sakae Kawato, Takao Kobayashi, Toshio Katsuyama, and Feng-Lei Hong. A multi-branch, fiber-based frequency comb with millihertz-level relative linewidths using an intra-cavity electro-optic modulator. *Optics Express*, 18(2):1667–1676, January 2010.

[76] C Benko, A Ruehl, M J Martin, K S E Eikema, M E Fermann, I Hartl, and J Ye. Full phase stabilization of a Yb:fiber femtosecond frequency

comb via high-bandwidth transducers. *Optics Letters*, 37(12):2196–2198, June 2012.

[77] C C Lee, C mohr, J Bethge, S Suzuki, M E Fermann, I Hartl, and Thomas R Schibli. Frequency comb stabilization with bandwidth beyond the limit of gain lifetime by an intracavity graphene electro-optic modulator. *Optics Letters*, 37(15):3084–3086, 2012.

[78] Tim Hellwig, Steffen Rieger, and Carsten Fallnich. Toward an all-optically stabilized frequency comb based on a mode-locked fiber laser. *Optics Letters*, 39(3):525–527, 2014.

[79] Chengying Bao, Andrew C Funk, Changxi Yang, and Steven T Cundiff. Pulse dynamics in a mode-locked fiber laser and its quantum limited comb frequency uncertainty. *Optics Letters*, 39(11):3266–3269, 2014.

[80] Naoya Kuse, Yutaka Nomura, Akira Ozawa, Makoto Kuwata-Gonokami, Shuntaro Watanabe, and Yohei Kobayashi. Self-compensation of third-order dispersion for ultrashort pulse generation demonstrated in an Yb fiber oscillator. *Optics Letters*, 35(23):3868–3870, 2010.

[81] R Jason Jones and Jun Ye. High-repetition-rate coherent femtosecond pulse amplification withan external passive optical cavity. *Optics Letters*, 29(23):2812–2814, December 2004.

[82] E D Black. An Introduction to Pound-Drever-Hall Laser Stabilization. *Am. J. Phys.*, page 79, 2001.

[83] R W P Drever, J L Hall, F V Kowalski, J Hough, G M Ford, A J Munley, and H Ward. Laser phase and frequency stabilization using an optical resonator. 31(2):97–105, 1983.

[84] Chengquan Li, Eric Moon, and Zenghu Chang. Carrier-envelope phase shift caused by variation of grating separation. *Optics Letters*, 31(21):3113–3115, November 2006.

[85] E Treacy. Optical pulse compression with diffraction gratings. *IEEE Journal of Quantum Electronics*, 5(9):454–458, 1969.

[86] Stacy Wise, V Quetschke, A J Deshpande, G Mueller, D H Reitze, D B Tanner, B F Whiting, Y Chen, A T unnermann, E Kley, and T Clausnitzer. Phase Effects in the Diffraction of Light: Beyond the Grating Equation. *Physical Review Letters*, 95:013901, 2005.

[87] Daniele Brida, Günther Krauss, Alexander Sell, and Alfred Leitenstorfer. Ultrabroadband Er:fiber lasers. *Laser & Photonics Reviews*, 8(3):409–428, January 2014.

[88] C Erny, K Moutzouris, J Biegert, D Kühlke, F Adler, Alfred Leitenstorfer, and Ursula Keller. Mid-infrared difference-frequency generation of ultrashort pulses tunable between 3.2 and 4.8. *Optics Letters*, 32:1138–1140, March 2007.

[89] Henry Timmers, Abijith Kowligy, Alex Lind, Flavio C Cruz, Nima Nader, Myles Silfies, Gabriel Ycas, Thomas K Allison, Peter G Schunemann, Scott B Papp, and Scott A Diddams. Molecular fingerprinting with bright, broadband infrared frequency combs. *Optica*, 5:1–6, June 2018.

[90] M E Fermann, V I Kruglov, B C Thomsen, J M Dudley, and J D Harvey. Self-Similar Propagation and Amplification of Parabolic Pulses in Optical Fibers. *Physical Review Letters*, 84:6010–6013, June 2000.

[91] John M Dudley, Christophe Finot, David J Richardson, and Guy Millot. Self-similarity in ultrafast nonlinear optics. *Nat Phys*, 3(9):597–603, September 2007.

[92] Jian Zhao, Wenxue Li, Chao Wang, Yang Liu, and Heping Zeng. Pre-chirping management of a self-similar Yb-fiber amplifier towards 80 W average power with sub-40 fs pulse generation. *Optics Express*, 22(26):32214–32219, December 2014.

[93] Shian Zhou, Lyuba Kuznetsova, Andy Chong, and Frank W Wise. Compensation of nonlinear phase shifts with third-order dispersion in short-pulse fiber amplifiers. *Optics Express*, 13(13):4869–4877, June 2005.

[94] Wei Liu, Damian N Schimpf, Tino Eidam, Jens Limpert, Andreas T u nnermann, Franz X K a rtner, and Guoqing Chang. Pre-chirp managed

nonlinear amplification in fibers delivering 100 W, 60 fs pulses. *Optics Letters*, 40(2):151–154, January 2015.

[95] F Roser, J Rothhard, B Ortac, A Liem, O Schmidt, T Schreiber, J Limpert, and A Tunnermann. 131 W 220 fs fiber laser system. *Optics Letters*, 30(20):2754–2756, October 2005.

[96] Zhigang Zhao and Yohei Kobayashi. Ytterbium fiber-based, 270 fs, 100 W chirped pulse amplification laser system with 1 MHz repetition rate. *Applied Physics Express*, 9(1):012701, 2016.

[97] Tino Eidam, Stefan Hanf, Enrico Seise, Thomas V Andersen, Thomas Gabler, Christian Wirth, Thomas Schreiber, Jens Limpert, and Andreas Tunnermann. Femtosecond fiber CPA system emitting 830 W average output power. *Optics Letters*, 35(2):94–96, January 2010.

[98] Marcel Wunram, Patrick Storz, Daniele Brida, and Alfred Leitenstorfer. Ultrastable fiber amplifier delivering 145-fs pulses with 6-μJ energy at 10-MHz repetition rate. *Optics Letters*, 40(5):823–826, March 2015.

[99] Axel Ruehl. Advances in Yb:Fiber Frequency Comb Technology. *Optics and Photonics News*, May 2012:31, 2012.

[100] Zhadnovich S Sheyerman A Levy G Damascelli A Mills A K and Jones D J. An XUV Source using a Femtosecond Enhancement Cavity for Photoemission Spectroscopy. *SPIE*, 2015.

[101] Tsung-Han Wu, David Carlson, and R Jason Jones. A high-power fiber laser system for dual-comb spectroscopy in the vacuum-ultraviolet. In *Frontiers in Optics 2013*, page FTu2A.4. Optical Society of America, 2013.

[102] R Paschotta, J Nilsson, A C Tropper, and D C Hanna. Ytterbium-doped fiber amplifiers. *IEEE J. Quantum Elec.*, 33(7):1049–1056, 1997.

[103] G Cheriaux, Barry Walker, L F DiMauro, P Rousseau, F Salin, and J P Chambaret. Aberration-free stretcher design for ultrashort-pulse amplification. *Optics Letters*, 21(6):414–416, March 1996.

[104] S Kane and J Squier. Fourth-order-dispersion limitations of aberration-free chirped-pulse amplification systems. *Journal of the Optical Society of America B*, 14(5):1237–1244, 1997.

[105] Jérôme Morville, Daniele Romanini, Marc Chenevier, and Alexander Kachanov. Effects of laser phase noise on the injection of a high-finesse cavity. *Applied Optics*, 41(33):6980–6990, November 2002.

[106] Ahmed H Zewail, M Dantus, R M Bowman, and A Mokhtari. Femtochemistry: recent advances and extension to high pressures. *"Journal of Photochemistry & Photobiology, A: Chemistry"*, 62(3):301–319, 1992.

[107] R W P Drever, John L Hall, F V Kowalski, J Hough, G M Ford, A J Munley, and H Ward. Laser phase and frequency stabilization using an optical resonator . *Applied Physics B: Lasers and Optics*, 31(2):97–105, June 1983.

[108] Aleksandra Foltynowicz, Ticijana Ban, Piotr Mas owski, Florian Adler, and Jun Ye. Quantum-Noise-Limited Optical Frequency Comb Spectroscopy. *Physical Review Letters*, 107:233002, November 2011.

[109] Travis C Briles, Dylan C Yost, Arman Cing o z, Jun Ye, and Thomas R Schibli. Simple piezoelectric-actuated mirror with 180 kHz servo bandwidth. *Optics Express*, 18(10):9739–9746, May 2010.

[110] R Campargue. Progress in overexpanded supersonic jets and skimmed molecular beams in free-jet zones of silence. *The Journal of Physical Chemistry*, 88(20):4466–4474, September 1984.

[111] D R Miller. Free Jet Sources. In G Scoles, editor, *Atomic and Molecular Beam Methods*. Oxford University Press, 1988.

[112] John F O'Hanlon. *A User's Guide to Vacuum Technology*. John Wiley & Sons, Inc., 3 edition, September 2003.

[113] Robert S Mulliken. Iodine Revisited. *The Journal of Chemical Physics*, 55(1):288–309, 1971.

[114] J I Steinfeld, R N Zare, L Jones, M Lesk, and W Klemperer. Spectroscopic Constants and Vibrational Assignment for the B $^3\Pi_{0_u^+}$ State of Iodine. *J. Chem. Phys.*, 42(1):25–33, 1965.

[115] J A Coxon. The calculation of potential energy curves of diatomic molecules: application to halogen molecules. *J. Quant. Spectrosc. Ra.*, 11:443–462, 1971.

[116] R F Barrow and Kim K Lee. $B^3\Pi_{O+u}$-$X^1\Sigma_g^+$ system of $^{127}I_2$: rotational analysis and long range potential in the $B^3\Pi_{O+u}$ state. *J. Chem. Soc. Faraday. T. 2*, 69:684–700, 1973.

[117] P Luc. Molecuiar Constants and Dun ham Expansion Parameters Describing the B-X System of the Iodine Molecule . *Journal of Molecular Spectroscopy*, 80:41–55, June 1980.

[118] A G Astill, A J McCaffery, M J Proctor, E A Seddon, and B J Whitaker. Pressure broadening of the nuclear hyperfine spectrum of 127I 2by He and Xe. *Journal of Physics B: Atomic and Molecular Physics*, 18(18):3745–3757, January 1999.

[119] A Saiz-Lopez, R W Saunders, D M Joseph, S H Ashworth, and J M C Plane. Absolute absorption cross-section and photolysis rate of I_2. *Atmos. Chem. Phys.*, 4(5):1443–1450, 2004.

[120] Juen-Kai Wang, Qianli Liu, and Ahmed H Zewail. Solvation Ultrafast Dynamics of Reactions. 9. Femtosecond Studies of Dissociation and Recombination of Iodine in Argon Clusters. *The Journal of Physical Chemistry*, 99(29):11309–11320, July 1995.

[121] H Eshet, M A Ratner, and R B Gerber. Selective energy and phase transfer in the photodissociation of I2 in argon clusters: Quantum dynamics simulations. *Chemical Physics Letters*, 431(1-3):199–203, November 2006.

[122] Chuangtian Chen, Yicheng Wu, Aidong Jiang, Bochang Wu, Guiming You, Rukang Li, and Shujie Lin. New nonlinear-optical crystal: LiB_3O_5. *Journal of the Optical Society of America B*, 6:616–621, April 1989.

[123] Edson R Peck and Donald J Fisher. Dispersion of Argon. *Journal of the Optical Society of America A*, 54:1362–1364, November 1964.

[124] Conor L Evans and X Sunney Xie. Coherent Anti-Stokes Raman Scattering Microscopy: Chemical Imaging for Biology and Medicine. *Annual Review of Analytical Chemistry*, 1(1):883–909, July 2008.

[125] Warren R Zipfel, Rebecca M Williams, and Watt W Webb. Nonlinear magic: multiphoton microscopy in the biosciences. *Nature Biotechnology*, 21(11):1369–1377, November 2003.

[126] Haohua Tu and Stephen A Boppart. Ultraviolet-visible non-supercontinuum ultrafast source enabled by switching single silicon strand-like photonic crystal fibers. *Optics Express*, 17:17983–17988, September 2009.

[127] K Moutzouris, F Adler, D Trautlein, and Alfred Leitenstorfer. Multi-milliwatt ultrashort pulses continuously tunable in the visible from a compact fiber source. *Optics Letters*, 31:1148–1150, March 2006.

[128] C Cleff, J Epping, P Gross, and Carsten Fallnich. Femtosecond OPO based on LBO pumped by˜a˜frequency-doubled Yb-fiber laser-amplifier system for˜CARS˜spectroscopy. *Applied Physics B*, 103(4):795–800, February 2011.

[129] Chenglin Gu, Minglie Hu, Jintao Fan, Youjian Song, Bowen Liu, Lu Chai, Chingyue Wang, and Derryck T Reid. High power tunable femtosecond ultraviolet laser source based on an Yb-fiber-laser pumped optical parametric oscillator. *Optics Express*, 23(5):6181–6186, 2015.

[130] Wenlong Tian, Zhaohua Wang, Xianghao Meng, Ninghua Zhang, Jiangfeng Zhu, and Zhiyi Wei. High-power, widely tunable, green-pumped femtosecond BiB_3O_6 optical parametric oscillator. *Optics Letters*, 41(21):4851–4854, 2016.

[131] Julius Vengelis, Ignas Stasevičius, Karolina Stankevičiūtė, Vygandas Jarutis, Rimantas Grigonis, Mikas Vengris, and Valdas Sirutkaitis. Characteristics of optical parametric oscillators synchronously pumped by second harmonic of femtosecond Yb:KGW laser. *Optics Communications*, 338(C):277–287, March 2015.

[132] Florian Adler, Kevin C Cossel, Michael J Thorpe, Ingmar Hartl, Martin E Fermann, and Jun Ye. Phase-stabilized, 1.5 W frequency comb at 2.8–4.8 um. *Optics Letters*, 34:1330–1332, April 2009.

[133] J H Sun, B J S Gale, and D T Reid. Composite frequency comb spanning 0.4–2.4 um from a phase-controlled femtosecond Ti:sapphire

laser and synchronously pumped optical parametric oscillator . *Optics Letters*, 32:1414–1416, April 2007.

[134] Bernd Metzger, Andy Steinmann, and Harald Giessen. High-power widely tunable sub-20fs Gaussian laser pulses for ultrafast nonlinear spectroscopy. *Optics Express*, 19:24354–24360, November 2011.

[135] Zhanwei Liu, Logan G Wright, Demetrios N Christodoulides, and Frank W Wise. Kerr self-cleaning of femtosecond-pulsed beams in graded-index multimode fiber. *Optics Letters*, 41(16):3675–3674, 2016.

[136] Alexander M Heidt, Alexander Hartung, Gurthwin W Bosman, Patrizia Krok, Erich G Rohwer, Heinrich Schwoerer, and Hartmut Bartelt. Coherent octave spanning near-infrared and visible supercontinuum generation in all-normal dispersion photonic crystal fibers. *Optics Express*, 19:3775–3787, January 2011.

[137] Yuan Liu, Youbo Zhao, Jens Lyngso, Sixian You, William L Wilson, Haohua Tu, and Stephen A Boppart. Suppressing Short-Term Polarization Noise and Related Spectral Decoherence in All-Normal Dispersion Fiber Supercontinuum Generation. *Journal of Lightwave Technology*, 33(9):1814–1820, July 2015.

[138] R Akbari and A Major. Optical, spectral and phase-matching properties of BIBO, BBO and LBO crystals for optical parametric oscillation in the visible and near-infrared wavelength ranges. *Laser Physics*, 23(3):035401–035409, January 2013.

[139] Arlee V Smith. SNLO nonlinear optics code available from A. V. Smith, AS-Photonics, ALbuquerque, NM.

[140] Travis C Briles, Dylan C Yost, Arman Cingoz, Jun Ye, and Thomas R Schibli. Simple piezoelectric-actuated mirror with 180 kHz servo bandwidth. *Optics Express*, 18:9739–9746, April 2010.

[141] David E Zelmon, David L Small, and Ralph Page. Refractive-index measurements of undoped yttrium aluminum garnet from 0.4 to 5.0 um. *Applied Optics*, 37:4933–4935, July 1998.

[142] H Mashiko, A Suda, and K Midorikawa. All-reflective interferometric autocorrelator for the measurement of ultra-short optical pulses. *Applied Physics B*, 76(5):525–530, May 2003.

[143] Eric D Black. An introduction to Pound–Drever–Hall laser frequency stabilization. *American Journal of Physics*, 69(1):79–87, January 2001.

[144] K Bartl, A Funk, K Schwing, H Fricke, G Kock, H D Martin, and M Gerhards. IR spectroscopy applied subsequent to a proton transfer reaction in the excited state of isolated 3-hydroxyflavone and 2-(2-naphthyl)-3-hydroxychromone. *Physical Chemistry Chemical Physics*, 11(8):1173–7, 2009.

[145] Simon Ameer-Beg, Stuart M Ormson, Robert G Brown, Pavel Matousek, Mike Towrie, Erik T J Nibbering, Paolo Foggi, and Frederik V R Neuwahl. Ultrafast Measurements of Excited State Intramolecular Proton Transfer (ESIPT) in Room Temperature Solutions of 3-Hydroxyflavone and Derivatives. *The Journal of Physical Chemistry A*, 105(15):3709–3718, April 2001.

[146] Jinyong Kim, Wooseok Heo, and Taiha Joo. Excited State Intramolecular Proton Transfer Dynamics of 1-Hydroxy-2-acetonaphthone. *The Journal of Physical Chemistry B*, 119(6):2620–2627, February 2015.

[147] Mario Barbatti, Adélia J A Aquino, Hans Lischka, Christian Schriever, Stefan Lochbrunner, and Eberhard Riedle. Ultrafast internal conversion pathway and mechanism in 2-(2‘-hydroxyphenyl)benzothiazole: a case study for excited-state intramolecular proton transfer systems. *Physical Chemistry Chemical Physics*, 11(9):1406–1410, 2009.

[148] Stefan Lochbrunner, K Stock, and Eberhard Riedle. Direct observation of the nuclear motion during ultrafast intramolecular proton transfer. *Journal of Molecular Structure*, 700(1-3):13–18, August 2004.

[149] Christian Schriever, Stefan Lochbrunner, Armin R Ofial, and Eberhard Riedle. The origin of ultrafast proton transfer: Multidimensional wave packet motion vs. tunneling. *Chemical Physics Letters*, 503(1-3):61–65, February 2011.

[150] Stefan Lochbrunner, Alexander J Wurzer, and Eberhard Riedle. Microscopic Mechanism of Ultrafast Excited-State Intramolecular Proton Transfer: A 30-fs Study of 2-(2‘-Hydroxyphenyl)benzothiazole. *The Journal of Physical Chemistry A*, 107(49):10580–10590, December 2003.

[151] Chul Hoon Kim and Taiha Joo. Coherent excited state intramolecular proton transfer probed by time-resolved fluorescence. *Physical Chemistry Chemical Physics*, 11(44):10266–5, 2009.

[152] C Schriever, Stefan Lochbrunner, Eberhard Riedle, and D J Nesbitt. Ultrasensitive ultraviolet-visible 20fs absorption spectroscopy of low vapor pressure molecules in the gas phase. *Review of Scientific Instruments*, 79(1):013107–013110, January 2008.

[153] Osama K Abou-Zied, Ralph Jimenez, Elizabeth H Z Thompson, David P Millar, and Floyd E Romesberg. Solvent-Dependent Photoinduced Tautomerization of 2-(2‘-Hydroxyphenyl)benzoxazole. *The Journal of Physical Chemistry A*, 106(15):3665–3672, April 2002.

[154] Shin-ichi Nagaoka, Noboru Hirota, Minoru Sumitani, and Keitaro Yoshihara. Investigation of the dynamic processes of the excited states of o-Hydroxybenzaldehyde and o-Hydroxyacetophenone by emission and picosecond spectroscopy. *Journal of Ameican Chemistry Society*, 105:4220–4226, January 1983.

[155] Stefan Lochbrunner, Kai Stock, and T Bizjak. Proton transfer and internal conversion of o-hydroxybenzaldehyde: coherent versus statistical excited-state dynamics. *Chemical Physics Letters*, 354:409–416, January 2002.

[156] Ryozo Takau, Yoshihisa Fujiwara, and Michiya Itoh. Comment No excited state proton transfer takes place in jet-cooled methanol clusters of 3-hydroxyflavone. *Chemical Physics Letters*, 217:478–480, January 1993.

[157] Nawee Kungwan, Felix Plasser, Adélia J A Aquino, Mario Barbatti, Peter Wolschann, and Hans Lischka. The effect of hydrogen bonding on the excited-state proton transfer in 2-(2-hydroxyphenyl)benzothiazole:

a TDDFT molecular dynamics study. *Physical Chemistry Chemical Physics*, 14(25):9016–9010, 2012.

[158] J M Dawes and S C Wallace. Excited state proton transfer in jet-cooled 3-hydroxyflavone and its methanol complexes. *Chemical Physics Letters*, 208:335–340, January 1993.

[159] Juan Angel Organero, Irene Garca-Ochoa, Miquel Moreno, José Maria Lluch, Luca Santos, and Abderrazzak Douhal. A theoretical insight into the internal H-bond and related rotational motion and proton transfer processes of 1-hydroxy-2-acetonaphthone in the S0 state. *Chemical Physics Letters*, 328(1-2):83–89, September 2000.

[160] Ji Eon Kwon and Soo Young Park. Advanced Organic Optoelectronic Materials: Harnessing Excited-State Intramolecular Proton Transfer (ESIPT) Process. *Advanced Materials*, 23(32):3615–3642, July 2011.

[161] Vikas S Padalkar and Shu Seki. Excited-state intramolecular proton-transfer (ESIPT)-inspired solid state emitters. *Chem. Soc. Rev.*, 45(1):169–202, 2016.

[162] Toshiki Mutai, Hirotaka Sawatani, Toshihide Shida, Hideaki Shono, and Koji Araki. Tuning of Excited-State Intramolecular Proton Transfer (ESIPT) Fluorescence of Imidazo[1,2- a]pyridine in Rigid Matrices by Substitution Effect. *The Journal of Organic Chemistry*, 78(6):2482–2489, February 2013.

[163] Kuo-Chun Tang, Ming-Jen Chang, Tsung-Yi Lin, Hsiao-An Pan, Tzu-Chien Fang, Kew-Yu Chen, Wen-Yi Hung, Yu-Hsiang Hsu, and Pi-Tai Chou. Fine Tuning the Energetics of Excited-State Intramolecular Proton Transfer (ESIPT): White Light Generation in A Single ESIPT System. *Journal of the American Chemical Society*, 133(44):17738–17745, November 2011.

[164] Wenhao Sun, Shayu Li, Rui Hu, Yan Qian, Shuangqing Wang, and Guoqiang Yang. Understanding Solvent Effects on Luminescent Properties of a Triple Fluorescent ESIPT Compound and Application for White Light Emission. *The Journal of Physical Chemistry A*, 113(20):5888–5895, May 2009.

[165] Dhiraj P Murale, Hwajin Kim, Wan Sung Choi, and David G Churchill. Highly Selective Excited State Intramolecular Proton Transfer (ESIPT)-Based Superoxide Probing. *Organic Letters*, 15(15):3946–3949, July 2013.

[166] Jie Ma, Jianzhang Zhao, Pei Yang, Dandan Huang, Caishun Zhang, and Qiuting Li. New excited state intramolecular proton transfer (ESIPT) dyes based on naphthalimide and observation of long-lived triplet excited states. *Chemical Communications*, 48(78):9720–3, 2012.

[167] Thermodynamic Research Center. TRCVP, Vapor Pressure Database, Version 2.2P.

[168] Th Arthen-Engeland, T Bultmann, Niko P Ernsting, M A Rodriguez, and W Thiel. Singlet excited-state intramolecular proton transferin 2-(2'-hydroxyphenyl)benzoxazole:spectroscopy at low temperatures, femtosecond transient absorption, and MNDO calculations. *Chemical Physics*, 163:43–53, April 1992.

[169] Amir Khodabakhsh, Chadi Abd Alrahman, and Aleksandra Foltynowicz. Noise-immune cavity-enhanced optical frequency comb spectroscopy. *Optics Letters*, 39(17):5034–5037, September 2014.

[170] S Holzberger, N Lilienfein, M Trubetskov, H Carstens, F L u cking, V Pervak, Ferenc Krausz, and I Pupeza. Enhancement cavities for zero-offset-frequency pulse trains. *Optics Letters*, 40(10):2165–2168, May 2015.

[171] C Gohle, T Udem, M Herrmann, J Rauschenberger, R Holzwarth, H A Schuessler, Ferenc Krausz, and T W Hansch. A frequency comb in the extreme ultraviolet. *Nature*, 436(7048):234–237, 2005.

[172] R Jason Jones and Jun Ye. Femtosecond pulse amplification by coherent addition in a passive optical cavity. *Optics Letters*, 27(20):1848–1850, 2002.

[173] Sang-Hee Shim and Martin T Zanni. How to turn your pump-probe instrument into a multidimensional spectrometer: 2D IR and Vis spectroscopies via pulse shaping. *Physical Chemistry Chemical Physics*, 11:748–761, 2009.

[174] Udo Buck and Friedrich Huisken. Infrared Spectroscopy of Size-Selected Water and Methanol Clusters. *Chemical Reviews*, 100(11):3863–3890, 2000.

[175] Lee C Ch'ng, Amit K Samanta, Yimin Wang, Joel M Bowman, and Hanna Reisler. Experimental and Theoretical Investigations of the Dissociation Energy (D0) and Dynamics of the Water Trimer, (H2O)3. *The Journal of Physical Chemistry A*, 117:7207, 2013.

[176] Frank N Keutsch and Richard J Saykally. Water clusters: Untangling the mysteries of the liquid, one molecule at a time. *Proceedings of the National Academy of Sciences*, 98(19):10533–10540, 2001.

[177] Takuya Majima, Gabriele Santambrogio, Christof Bartels, Akira Terasaki, Tamotsu Kondow, Jan Meinen, and Thomas Leisner. Spatial distribution of ions in a linear octopole radio-frequency ion trap in the space-charge limit. *Physical Review A*, 85:053414, May 2012.

[178] Guo-Zhong Li, Shenheng Guan, and Alan G Marshall. Comparison of Equilibrium Ion Density Distribution and Trapping Force in Penning, Paul, and Combined Ion Traps. *J. Am. Soc. Mass. Spectr.*, 9(5):473–481, 1998.

[179] M K Liu, R D Averitt, T Durakiewicz, P H Tobash, E D Bauer, S A Trugman, A J Taylor, and D A Yarotski. Evidence of a hidden-order pseudogap state in URu_2Si_2 using ultrafast optical spectroscopy. *Phys. Rev. B*, 84:161101, October 2011.

[180] Takuro Ideguchi, Simon Holzner, Birgitta Bernhardt, Guy Guelachvili, Nathalie Picqué, and Theodor W Hänsch. Coherent Raman spectro-imaging with laser frequency combs. *Nature*, 502(7471):355–358, October 2013.

[181] Bachana Lomsadze and Steven T Cundiff. Frequency combs enable rapid and high-resolution multidimensional coherent spectroscopy. *Science*, 357(6358):1389–1391, September 2017.